1982

Application of quasi-lagrangian diagnostics to the study of numerically-simulated oceanic cyclones.

Tallman, William C.

Monterey, California. Naval Postgraduate School

NAVAL POSTGRADUATE SCHOOL
Monterey, California

THESIS

APPLICATION OF QUASI-LAGRANGIAN DIAGNOSTICS
TO THE STUDY OF
NUMERICALLY-SIMULATED OCEANIC CYCLONES

by

William C. Tallman

June 1982

Thesis Advisor: Carlyle H. Wash

SECURITY CLASSIFICATION OF THIS PAGE (When Data Entered)

REPORT DOCUMENTATION PAGE

READ INSTRUCTIONS BEFORE COMPLETING FORM

1. REPORT NUMBER

2. GOVT ACCESSION NO.

3. RECIPIENT'S CATALOG NUMBER

4. TITLE (and Subtitle)
Application of Quasi-Lagrangian Diagnostics to the study of Numerically-Simulated Oceanic Cyclones

5. TYPE OF REPORT & PERIOD COVERED
Master's Thesis; June 1982

6. PERFORMING ORG. REPORT NUMBER

7. AUTHOR(s)
William C. Tallman

8. CONTRACT OR GRANT NUMBER(s)

9. PERFORMING ORGANIZATION NAME AND ADDRESS
Naval Postgraduate School
Monterey, California 93940

10. PROGRAM ELEMENT, PROJECT, TASK AREA & WORK UNIT NUMBERS

11. CONTROLLING OFFICE NAME AND ADDRESS
Naval Postgraduate School
Monterey, California 93940

12. REPORT DATE
June 1982

13. NUMBER OF PAGES
121

14. MONITORING AGENCY NAME & ADDRESS(if different from Controlling Office)

15. SECURITY CLASS. (of this report)
Unclassified

15a. DECLASSIFICATION/DOWNGRADING SCHEDULE

16. DISTRIBUTION STATEMENT (of this Report)

Approved for public release; distribution unlimited.

17. DISTRIBUTION STATEMENT (of the abstract entered in Block 20, if different from Report)

18. SUPPLEMENTARY NOTES

19. KEY WORDS (Continue on reverse side if necessary and identify by block number)
Mass, storm-following budget,
model-generated cyclones,
NOGAPS, budget-derived vertical velocities,
oceanic cyclones,

20. ABSTRACT (Continue on reverse side if necessary and identify by block number)

A study of two oceanic extratropical cyclones, generated by the Navy Operational Atmospheric Prediction System (NOGAPS) model (see Sandgathe, 1981), reveals a simultaneous development of the upper- and lower-tropospheric features while these features maintain their positions relative to each other. These cyclones also develop extreme shear in most synoptic fields after 120 hours of numerical simulation.

DD FORM 1 JAN 73 1473 EDITION OF 1 NOV 65 IS OBSOLETE
S/N 0102-014-6601

SECURITY CLASSIFICATION OF THIS PAGE (When Data Entered)

The mass budgers of these cyclones show a concentration of inward lateral transport (convergence) in the lowest model layer and outward lateral transport (divergence) in a layer centered near 300 mb. Time sections of lateral transprot, vertical velocity and mass tendency reveal that these cyclones develop in two phases--an explosive cyclogenesis phase, and a quasi-steady state phase. These time sections also reveal a 12-hour cyclic pattern embedded within the two phases of cyclone evolution. This 12-hour cyclic pattern is not evident in the map sequences of the surface pressure.

Approved for public release; distribution unlimited

Application of Quasi-Lagrangian Diagnostics to the Study of Numerically-Simulated Oceanic Cyclones

by

William C. Tallman
Captain, United States Air Force
B.S., St. John's University, 1968
M.S., Northeast Missouri State University, 1973

Submitted in partial fulfillment of the
requirements for the degree of

MASTER OF SCIENCE IN METEOROLOGY

from the

NAVAL POSTGRADUATE SCHOOL
June, 1982

ABSTRACT

A study of two oceanic extratropical cyclones, generated by the Navy Operational Atmospheric Prediction System (NOGAPS) model (see Sandgathe, 1981), reveals a simultaneous development of the upper- and lower-tropospheric features while these features maintain their positions relative to each other. These cyclones also develop extreme shear in most synoptic fields after 120 hours of numerical simulation.

The mass budgets of these cyclones show a concentration of inward lateral transport (convergence) in the lowest model layer and outward lateral transport (divergence) in a layer centered near 300 mb. Time sections of lateral transport, vertical velocity and mass tendency reveal that these cyclones develop in two phases--an explosive cyclogenesis phase, and a quasi-steady state phase. These time sections also reveal a 12-hour cyclic pattern embedded within the two phases of cyclone evolution. This 12-hour cyclic pattern is not evident in the map sequences of the surface pressure.

TABLE OF CONTENTS

I. INTRODUCTION 12

II. ATMOSPHERIC MODEL DESCRIPTION 19

A. MODEL STRUCTURE 19

B. INITIAL CONDITIONS 23

III. SYNOPTIC DISCUSSION 25

A. OVERVIEW 25

B. LOWER-TROPOSPHERE FEATURES 28

C. MID-LEVEL FEATURES 40

D. UPPER-LEVEL FEATURES 51

E. COMPARISON TO OBSERVED CYCLONES 62

IV. QUASI-LAGRANGIAN DIAGNOSTIC TECHNIQUE 70

A. QUASI-LAGRANGIAN DIAGNOSTICS 70

B. BUDGET EQUATIONS 74

V. BUDGET ANALYSIS 76

A. INTRODUCTION 76

B. THERMAL STRUCTURE 77

C. MASS TENDENCY 79

D. LATERAL MASS TRANSPORT 85

E. VERTICAL MASS TRANSPORT 89

F. COMPARISON OF MODEL AND BUDGET VERTICAL VELOCITIES 97

VI. CONCLUSIONS 106

VII. RECOMMENDATIONS FOR FURTHER STUDIES 110

APPENDIX A. COMMONLY USED ACRONYMS AND ABBREVIATIONS . .111

APPENDIX B. QUASI-LAGRANGIAN BUDGET FRAMEWORK AND GENERALIZED BUDGET EQUATIONS 113

LIST OF REFERENCES 117

INITIAL DISTRIBUTION LIST 120

LIST OF TABLES

TABLE I. DATA FIELDS DEPICTED IN THE SYNOPTIC SUMMARY. 27

TABLE II. CENTRAL SURFACE PRESSURES OF THREE MODEL CYCLONES 30

TABLE III. QUASI-LAGRANGIAN DIAGNOSTICS BUDGET STUDIES (partially extracted from Wash, 1978) 72

TABLE IV. QUASI-LAGRANGIAN MASS BUDGET EQUATION IN SIGMA COORDINATES 75

TABLE V. GENERALIZED QUASI-LAGRANGIAN BUDGET EQUATIONS IN SIGMA COORDINATES 116

LIST OF FIGURES

Figure 1. Vertical distribution of model large-scale prognostic variables. 21

Figure 2. Horizontal distribution of model large-scale prognostic variables. 23

Figure 3. Storm tracks of two model cyclones. 28

Figure 4. Surface pressure and temperature fields valid at initial time + 96 hours. 31

Figure 5. 1000 mb height and 1000 mb to mid-layer 4 thickness fields valid at initial time + 96 hours. 32

Figure 6. Same as Fig. 4 except for initial time + 120 hours. 34

Figure 7. Same as Fig. 5 except for initial time + 120 hours. 35

Figure 8. Same as Fig. 4 except for initial time + 144 hours. 37

Figure 9. Same as Fig. 5 except for initial time + 144 hours. 38

Figure 10. Same as Fig. 4 except for initial time + 168 hours. 41

Figure 11. Same as Fig. 5 except for initial time + 168 hours. 42

Figure 12. Mid-layer 4 height and temperature fields valid at initial time + 96 hours. 43

Figure 13. Mid-layer 4 absolute vorticity (sec^{-1}) and wind fields valid at initial time + 96 hours. 44

Figure 14. Same as Fig. 12 except for initial time + 120 hours. 47

Figure 15. Same as Fig. 13 except for initial time + 120 hours. 48

Figure 16. Same as Fig. 12 except for initial time + 144 hours. 49

Figure 17. Same as Fig. 13 except for initial time + 144 hours. 50

Figure 18. Same as Fig. 12 except for initial time + 168 hours. 53

Figure 19. Same as Fig. 13 except for initial time + 168 hours. 54

Figure 20. Mid-layer 3 height and temperature fields valid at initial time + 96. 55

Figure 21. Mid-layer 3 wind vectors and isotachs valid at initial time + 96. 56

Figure 22. Same as Fig. 20 except for initial time + 120 hours. 57

Figure 23. Same as Fig. 21 except for initial time + 120 hours. 58

Figure 24. Same as Fig. 20 except for initial time + 144 hours. 60

Figure 25. Same as Fig. 21 except for initial time + 144 hours. 61

Figure 26. Same as Fig. 20 except for initial time + 168 hours. 63

Figure 27. Same as Fig. 21 except for initial time + 168 hours. 64

Figure 28. Cyclone N1 area-averaged potential temperature time section. 80

Figure 29. Cyclone S area-averaged potential temperature time section. 81

Figure 30. Area-averaged pressure tendency for cyclones N1 and S. 83

Figure 31. Central surface pressures (mb) of cyclones N1 and S. 87

Figure 32. Cyclone N1 lateral mass transport time section. 91

Figure 33. Cyclone S lateral mass transport time section. 92

Figure 34. Cyclone N1 model vertical velocity time section. 94

Figure 35. Cyclone S model vertical velocity time section. 95

Figure 36. Model vertical velocity for level 4. 98

Figure 37. Mass budget vertical velocity time section for cyclone N1. 102

Figure 38. Mass budget vertical velocity time section for cyclone S. 103

Figure 39. Budget vertical velocity error time section for cyclone N1. 104

Figure 40. Budget vertical velocity error time section for cyclone S. 105

Figure 41. Quasi-Langrangian storm budget volume coordinate system. 115

ACKNOWLEDGEMENT

I would like to take this opportunity to express my sincere gratitude to Dr. Carlyle H. Wash for his time, guidance, and patience. Without his assistance and encouragement this thesis would not have been completed. Additionally, the computer programs provided by Dr. Wash were invaluable. I would also like to thank Dr. Russel Elsberry for his guidence in editing the manuscript.

Special thanks is given to Dr. Scott Sandgathe for the numerous helpful discussions concerning his experiments from which the data for this study was obtained. I greatfully acknowledge the contributions of Mr. James Peak for always being available to assist with modifying the computer code. Mr. Michael McDermet also deserves thanks for his assistance in the preparation of the graphics.

Finally, I wish to express my deepest thanks to Julie, Jeff, and Sarah for their support, encouragement, and understanding.

I. INTRODUCTION

For many years maritime cyclones have been of interest to military and civilian communities from both a scientific and a practical point of view. Oceanic lows frequently develop rapidly and produce meteorological phenomena which can adversely impact civilian and military operations in oceanic and coastal regions. Accurate and dependable prediction of the development and movement of oceanic cyclones is required for reliable maritime forecasts.

Numerous studies of middle-latitude cyclones have focused on continental cyclones (e.g. Smith (1973), Petterssen and Smebye (1971), Johnson and Downey (1976), Chen and Bosart (1977), and others). This is primarily due to the abundant observational data which is readily available from continental regions. In contrast, relatively few studies have investigated maritime cyclones because of the limited observational data from oceanic regions. As a result, the factors influencing maritime cyclogenesis are not fully understood.

Several studies of oceanic cyclones indicate that significant differences exist in the physics involved in continental and oceanic cyclogenesis. Petterssen, Bradbury and

Pedersen (1962) compared the development of cyclones over the western North Atlantic to that of cyclones over the eastern United States. This observational study indicates that the initial development of oceanic cyclones appeared to result primarily from low-level thermal advection while continental cyclones usually developed as a result of an upper-level vorticity maximum approaching a low-level baroclinic zone. A study by Nitta and Yamamoto (1974) also suggests that maritime cyclones frequently develop in the vicinity of an ocean baroclinic zone in conjunction with nearly zonal upper-level flow. Sanders and Gyakum (1980) found that explosive cyclogenesis is predominantly a maritime, cold-season event and suggested that the roles played by cumulus convection and air-sea fluxes in cyclogenesis are not adequately understood. A numerical study by Sandgathe (1981) indicates that air-sea fluxes play a significant role in the evolution of oceanic cyclones. These studies and others suggest that the air-sea fluxes of latent and sensible heat play a significant role in oceanic storm development.

Current operational numerical models have been shown to be seriously deficient in predicting maritime cyclone deepening rates. The Sanders and Gyakum (1980) study indicated that the National Meteorological Center (NMC) primitive-equation models predicted less than one half of the deepening rates observed in explosive oceanic cyclogenesis. The failure of numerical models to predict explosive cyclogenesis is not entirely the result of the limited observational data from oceanic regions. Part of the problem lies in modeling vertical exchanges in the atmosphere. The upper troposphere is dominated by wave structures, while vortex structures dominate in the lower troposphere. Most cases of upper tropospheric wave amplification are accompanied by the development of anticyclones and cyclones in the lower troposphere. This suggests that there exists a strong interaction between these two regimes. The smaller size of oceanic cyclones presents another problem. The space scale of upper tropospheric waves is typically two to four times the space scale of oceanic cyclones. As a result, it appears that numerical models adequately simulate the large-scale processes involved in synoptic-scale systems, but do not capture the smaller-scale features embedded within synoptic-scale weather systems.

Due to the sparse observational network in oceanic regions, few quantitative studies of maritime cyclogenesis have been completed. To fill this void, studies of numerically simulated cyclone development are needed. Numerical models, having an internally consistent "data" base, eliminate errors resulting from incomplete or inaccurate observations from data-sparse regions such as oceans. In cases where there is a favorable comparison between numerically simulated cyclogenesis and real atmosphere cyclogenesis, the model may provide a greater understanding of the physics involved in cyclone development than would the incomplete observations of the real atmosphere storm. A disagreement between the model and the real atmosphere would not necessarily prove to be of little or no value. In cases where the model and the real atmosphere do not agree, the diagnostics of the real atmosphere may well isolate the reasons for the disagreement and thus lead to improvement in the model.

A basic feature of cyclogenesis is an inward mass transport (convergence) in the lower troposphere and and outward mass transport (divergence) in the upper troposphere. Associated with these horizontal mass transports is an upward vertical mass transport within the cyclone. Quantifying

this mass circulation can provide important information about the large-scale forcing within a cyclone.

Cyclones are vortices embedded in a planetary-scale pattern. Consequently, a study of the basic properties of cyclones should take advantage of their vortex nature. One such approach is the investigation of the budgets of the fundamental quantities such as mass and circulation within a volume moving with the storm. Quasi-Lagrangian transport theory, outlined by Johnson and Downey (1975 a and b), is particularly suited for the study of cyclones.

In this thesis the mass budgets of numerically simulated oceanic cyclones are investigated to ascertain the basic aspects of cyclone development and maintenance. A quantitative study of the mass circulation helps describe the intensity and physical structure of the cyclone and isolate vertical variations in the cyclone circulation.

This study follows the Ph.D. thesis investigation by Sandgathe (1981). The budget studies were applied to two storms generated by a version of the UCLA general circulation model, which includes a sophisticated parameterization scheme for planetary boundary layer (PBL) and free atmosphere interactions. The Sandgathe study demonstrated the

role of air-sea fluxes of heat and moisture in initial cyclogenesis. He showed that cyclone intensification resulted when sensible heat fluxes were removed. In contrast, the lack of moisture fluxes resulted in cyclone decay.

In this thesis, two cyclones were studied--one in the southern (spring) hemisphere and one in the northern (fall) hemisphere. Both storms are characterized by rapid development during the period from 96 to 126 hours of simulated cyclogenesis. In each case, the central surface pressure of these storms decreases at a rate of nearly one mb per hour during this 30 hour period. Thus, these storms are good examples of the explosive deepening which is not adequately handled by current operational dynamic models.

This study is one in a series of experiments designed to investigate the physical processes involved in extratropical cyclone development. The primary objectives of this study are:

- to study the synoptic features of two model-generated cyclones and compare them to observed cyclones;
- to isolate the lateral and vertical branches of the mass circulation during different stages in the evolution of a model-generated maritime cyclone; and,
- to compare vertical velocity values derived through quasi-Lagrangian diagnostics with the vertical velocity values from the models internally consistent "data" set.

The atmospheric model used for this study is briefly described in Chapter II. The results of this study begin in Chapter III with an objective review of the synoptic features of the two model storms. A description of the quasi-Lagrangian diagnostics technique and the equations used in the mass and circulation budgets are presented in Chapter IV. The generalized budget equation and the budget volume coordinate system are described in Appendix B. Chapter V contains the analysis of the mass budget results. Conclusions and recommendations for further studies are presented in Chapters VI and VII respectively.

II. ATMOSPHERIC MODEL DESCRIPTION

A. MODEL STRUCTURE

The Sandgathe experiments used the Navy Operational Atmospheric Prediction System (NOGAPS) model which is being developed by the Naval Environmental Prediction Research Facility (NEPRF). The NOGAPS model is a state-of-the-art version of the UCLA general circulation model. A brief overview of the NOGAPS model is presented in this chapter, For a more detailed description of the NOGAPS model the reader is directed to Sandgathe (1981). The UCLA model is described in detail by Arakawa and Lamb (1977).

A fine resolution grid (2 degrees latitude by 2.5 degrees longitude) within a 60 degree longitude global sector is used in this model. This grid resolution, which equates to a 222 km by 196 km grid distance at 45 degrees latitude, is sufficient to resolve shorter cyclone waves.

The prognostic variables of the model include the surface pressure minus 50 mb, π , the horizontal wind velocity, V, temperature, T, and specific humidity, q. Several other prognostic variables (to be discussed later) are associated with the PBL.

The model uses a sigma vertical coordinate system defined as:

$$\sigma = \frac{P - P_T}{\pi}$$

where:

P = pressure

$\pi = P_S - P_T$

P_S = surface pressure

P_T = pressure at the top of the model atmosphere (50 mb). Thus the top and bottomy moundaries of the model are $\sigma = 0$ and $\sigma = 1$. The NOGAPS model consists of six vertical layers (Fig. 1). In this depiction, an arbitrary surface pressure of 1000 mb has been assumed. Variables carried at the layer mid-levels are T, V, and q. The vertical velocity, $\dot{\sigma}$, is defined at the layer interfaces.

The model employes a staggered grid (Arakawa scheme C) in the horizontal (Fig. 2). The variables defined at the center points are T, q, and $\pi\dot{\sigma}$. The meridional wind component, v, is carried one degree north and south of the center point with the zonal wind component, u, carried 1.25 degrees east and west of the center point. For diabatic and frictional computations, the u and v components are averaged to the center point. A smoothing of the meridional component adjacent to the poles is implemented in theis model.

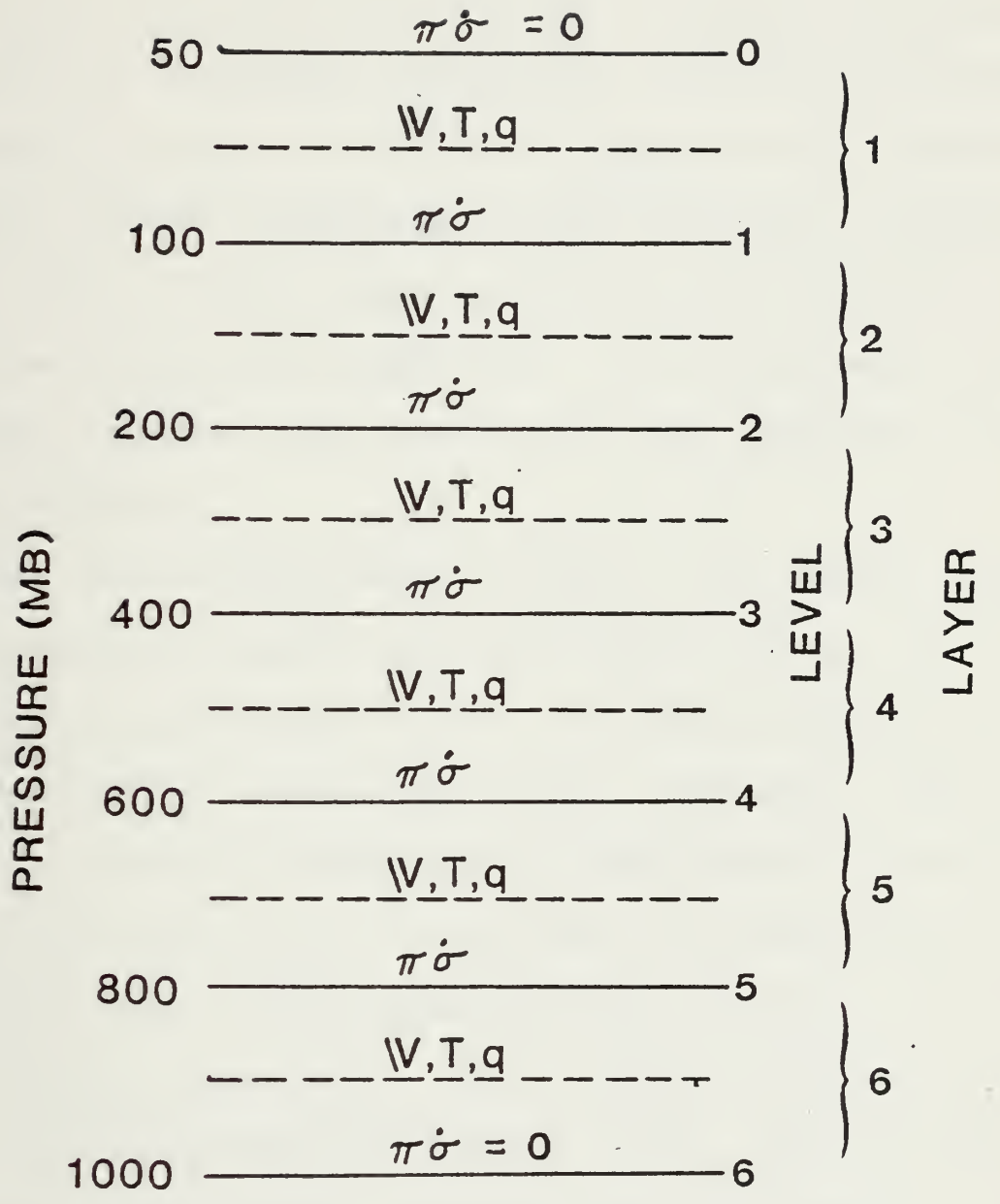

Figure 1. Vertical distribution of model large-scale prognostic variables. Pressure values of sigma levels vary with the surface pressure. A surface value of 1000 mb is assumed in this figure. (After Sandgathe, 1981)

The area used for this study, 60 degrees wide extending from pole to pole, is an open-ocean (i.e. entirely over water with no sea ice) domain which is fixed in time with two zones (centered at 45N and 35S) of maximum north-south gradients in sea-surface temperature. Continuous over-ocean propagation within the model is guaranteed by imposing cyclic boundary conditions in the east-west direction. There are 91 and 24 grid points in the north-south and east-west directions respectively. For this thesis, zero degrees longitude has arbitrarily been assigned to the western boundary.

The PBL paramererization scheme of the NOGAPS model, which follows Deardorff (1972) and Randall (1976), provides for interactions between the PBL and cumulus and/or stratus cloud ensembles at each grid point. Momentum, heat and moisture fluxes at the surface are diagnostically determined using the values of T, V, and q from the dynamic portion of the model and a bulk Richardson number which is based no sea-surface temperature. The cumulus parameterization scheme follows Arakawa and Schubert (1974) and Lord (1978). Effects of water vapor, predicted cloud distributions, and large-scale precipitation processes are included in the radiational heating package which follows Katayama (1972).

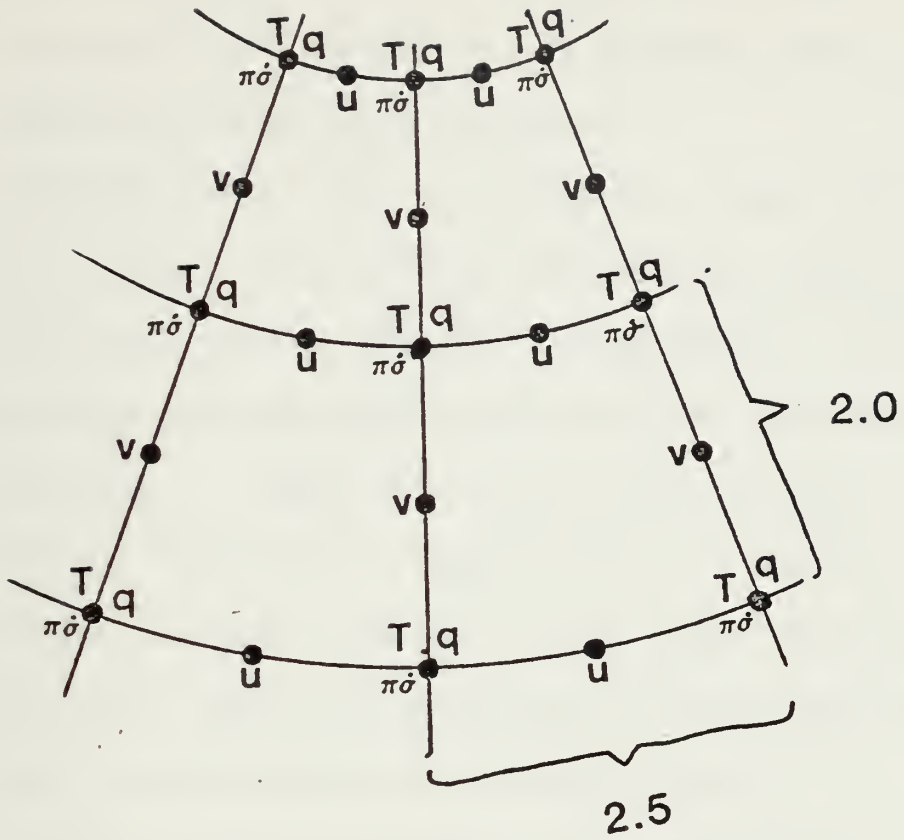

Figure 2. Horizontal distribution of model large-scale prognostic variables. This distribution follows Arakawa scheme C. (After Sandgathe, 1981)

B. INITIAL CONDITIONS

The Sandgathe study utilized initial conditions which are representative of open-ocean fall and spring regimes. The initial conditions for the model atmosphere follow Simmons and Hoskins (1977, 1978). Wind profiles for the fall hemisphere were determined using a polynomial

approximation of the January mean zonal wind profile at 30N from Oort and Rasmussen (1971). The fall hemisphere winds are multiplied by a factor of 1.5 at each level to provide the spring hemisphere wind profiles.

The model start time was 1 October. Thus, with respect to solar fluxes, the northern and southern hemispheres are the fall and spring regimes respectively. Sea-surface temperatures and atmospheric jets are also representative of these seasons. Zonal jets of 35 m sec^{-1} and 52 m sec^{-1}, centered at 45N and 35S respectively, represent possible conditions for these regimes. As shown by Simmons and Hoskins (1977, 1978), the existance of these jets guarantees the growth of baroclinically unstable waves.

Sandgathe used the conditions listed above as initial conditions in his experiments on the evolution of extratropical cyclones. A small amplitude sinusoidal perturbation in wave number six was added to the meridional wind component at each level. The maximum value of the perturbation was .5 m sec^{-1} at 45N/S. The perturbation at the equator and the poles was zero. The associated perturbation in the surface pressure field was approximately one millibar.

III. SYNOPTIC DISCUSSION

A. OVERVIEW

An initial objective of this thesis is a comparison of the synoptic features of numerically simulated and observed oceanic cyclones. This discussion will focus on the significant features in the model "data" fields. Available "data" consists of model output at three-hour intervals from hour 96 to hour 168 inclusive. Except for the 1000 mb heights and surface pressures, all fields in this discussion are generated from mid-layer model data. With the exception of the wind fields, a three point zonal smoothing technique was applied to all data fields represented in this chapter. The u and v wind components were averaged to the height grid points for the wind field representations.

The synoptic summary of the two model cyclones begins with a presentation of the significant features in the lower troposphere using surface pressure and temperature fields, the 1000 mb height fields and the 1000 mb to mid-layer 4 (approximately 1000-500 mb) thickness fields (Figs. 4 to 11). This is followed by a summary of mid-tropospheric

features (mid-layer 4, approximately 500 mb) of the height, temperature, wind, and vorticity fields (Figs. 12 to 19). Significant features in the mid-layer 3 (approximately 300 mb) height, wind, and temperature fields are described in the fourth section (Figs. 20 to 27). This chapter concludes with a brief comparison of the development of the model cyclones and observed cyclones.

Table I contains a list of synoptic fields relevent to this summary. Fields valid at 96, 120, 144, and 168 hours after the initial time are presented. With respect to the synoptic summary and the figures presented in this thesis, the indicated times represent the number of hours of numerical simulation. The storm tracks of the two numerically simulated cyclones used for the budget studies of this thesis are shown in Fig. 3.

The figures presented in this chapter depict two adjacent 60 degree sectors based on the cyclic continuity assumption of the model. Six and nine degree budget volume circles, centered on the surface pressure minimum, are depicted on each chart. Radii six and nine were chosen because they include the more intense portion of the cyclones during the early and latter stages of the study

respectively. In following discussions, inner radius and outer radius refer to the six and nine degree budget radii respectively. Both the northern hemisphere (NH) and southern hemisphere (SH) cyclones are discussed, relative to each figure, to point out differences and similarities in their development.

TABLE I

DATA FIELDS DEPICTED IN THE SYNOPTIC SUMMARY

SIGMA LEVEL (OR LAYER)	APPROXIMATE PRESSURE LEVEL(S)	FIELDS
level 6	surface	pressure (mb)/ temperature
(1000 mb)/ mid-layer 4	1000/ 500 mb	1000 - 500 mb thickness/ 1000 mb height
level 6	surface	pressure/ temperature
mid-layer 4	500 mb	vorticity/ height
mid-layer 4	500 mb	temperature/ height
mid-layer 3	300 mb	temperature/ height
mid-layer 3	300 mb	wind vectors/ isotachs

a.

b.

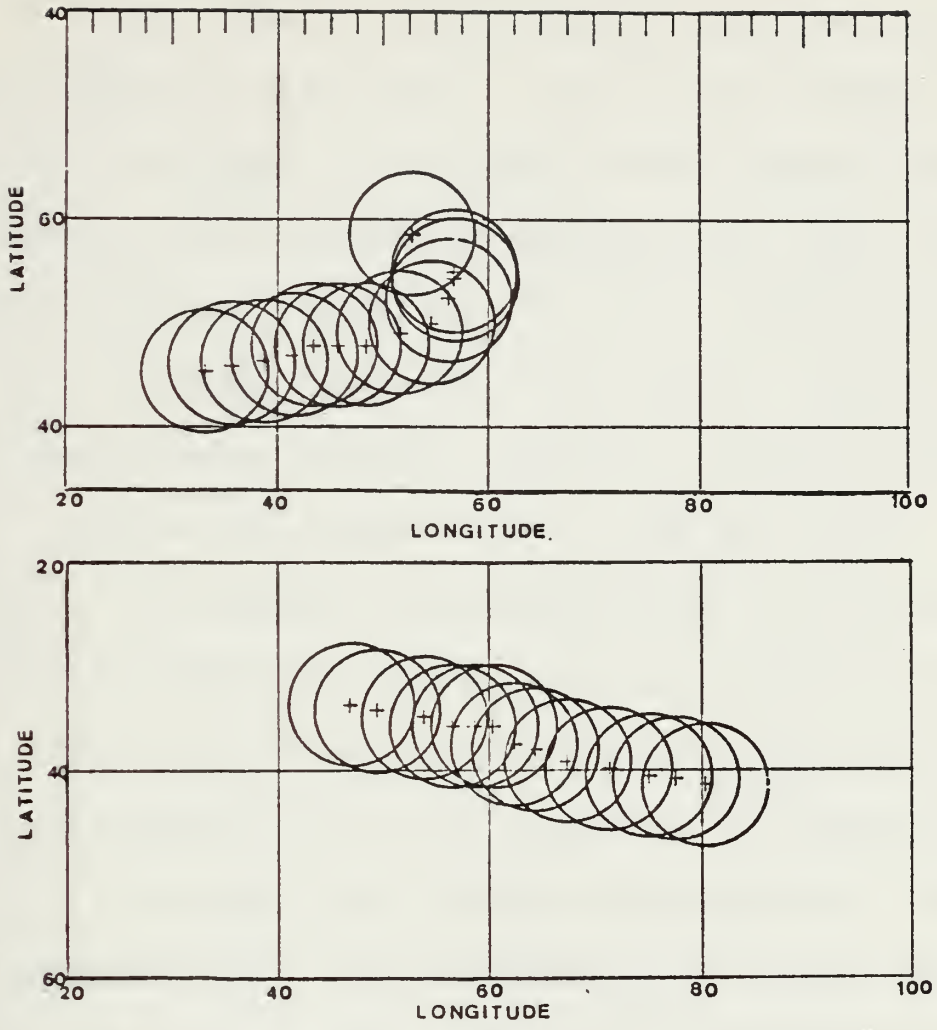

Figure 3. Storm tracks of two model cyclones. Indicated locations are for six hour intervals from hour 96 through hour 168. Circle radius is 6° latitude. a. Northern hemisphere. b. Southern hemisphere.

B. LOWER-TROPOSPHERE FEATURES

Surface pressure and temperature fields valid at hour 96 are shown in Fig. 4. The 1000 mb height and 1000 mb to mid-layer 4 (approximately 1000 - 500 mb) thickness fields

for the same time are presented in Fig. 5. Weak thermal ridges, at 32 (92) and 57 (117) degrees longitude respectively, are apparent in the NH. A 1011 mb low (cyclone N1) is located in the thermal ridge near 32 (92) degrees longitude. A somewhat more intense low (cyclone N2), with a central surface pressure of 1007 mb, is in the thermal ridge near 57 (117) degrees longitude. Initially, cyclone N2 appears to be the main feature; however, within 24 hours, cyclone N1 becomes the dominant low in the NH sector. A third area of low pressure approximately 1000 nm northeast of cyclone N1 develops very little, but does persist through hour 156. This low pressure area will be discussed briefly later in this section. In the SH, a 1003 mb low (cyclone S) is located in a thermal ridge oriented south-southwest (SSW) to north-northeast (NNE) and centered near 40 degrees longitude. Table II contains the central surface pressure values of the three cyclones discussed in this synoptic summary. Cyclones N1, N2, and S all display typical lower-tropospheric thermal advection patterns with warm advection ahead of, and cold advection behind and equatorwardof the developing cyclones.

TABLE II

CENTRAL SURFACE PRESSURES OF THREE MODEL CYCLONES

(in mb)

TIME	CYCLONE N1	CYCLONE N2	CYCLONE S
96	1011	1007	1003
99	1008	1002	1001
102	1006	1001	998
105	1006	1002	996
108	1005	1001	994
111	1000	998	992
114	997	996	989
117	995	998	988
120	992	998	986
123	988	997	984
126	987	997	979
129	988	998	979
132	989	1000	979
135	989	1001	978
138	987	1001	976
141	989	1004	975
144	990	1005	975
147	988	1006	975
150	987	1006	976
153	988	1008	978
156	988	1008	980
159	985	1006	978
162	985	1006	979
165	985	1006	980
168	984	1006	981

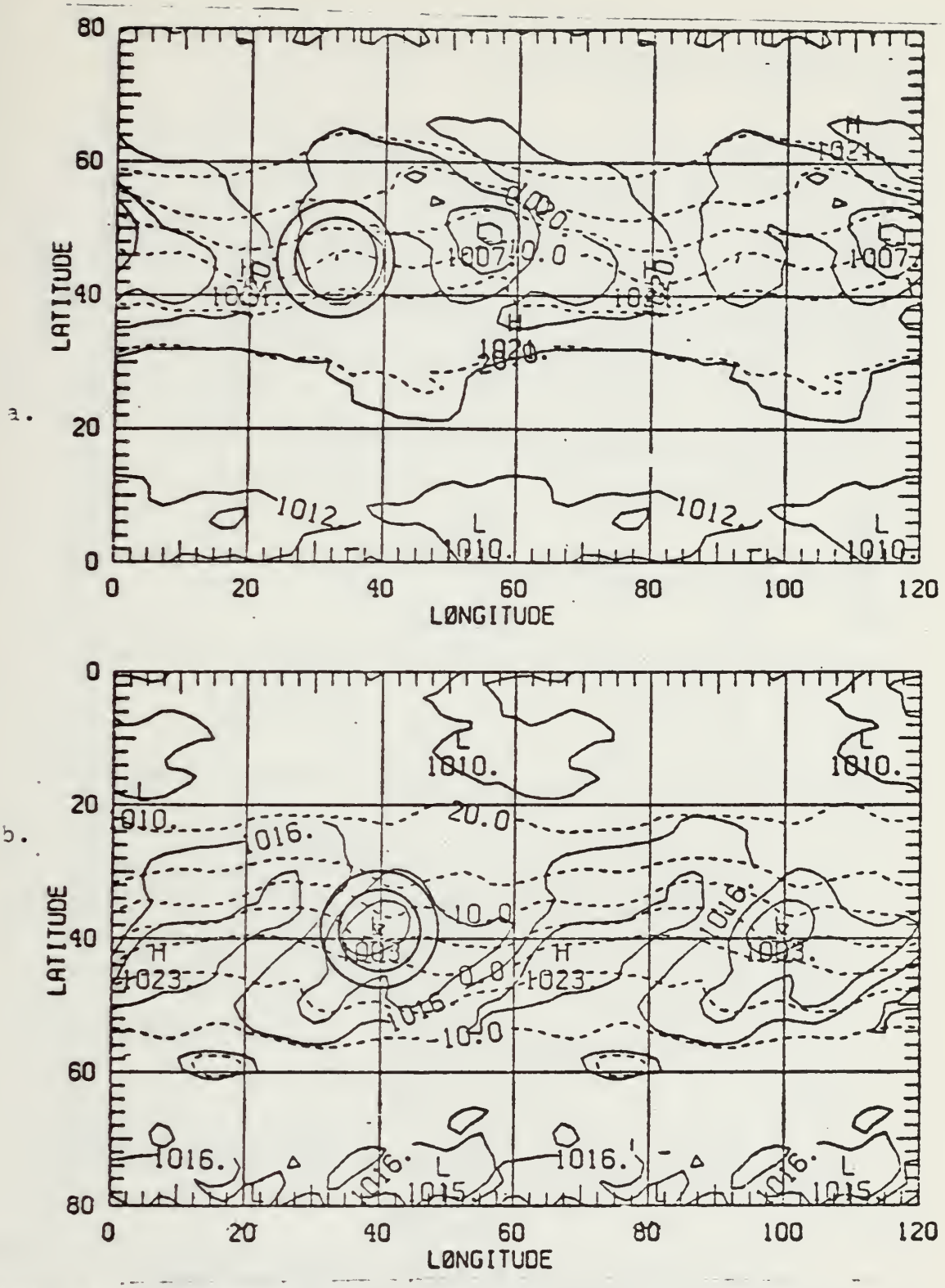

Figure 4. Surface pressure and temperature fields valid at initial time + 96 hours. Isobars (solid) are in millibars. Isotherms (dashed) are in °C.
a. and b. as in Fig. 3.

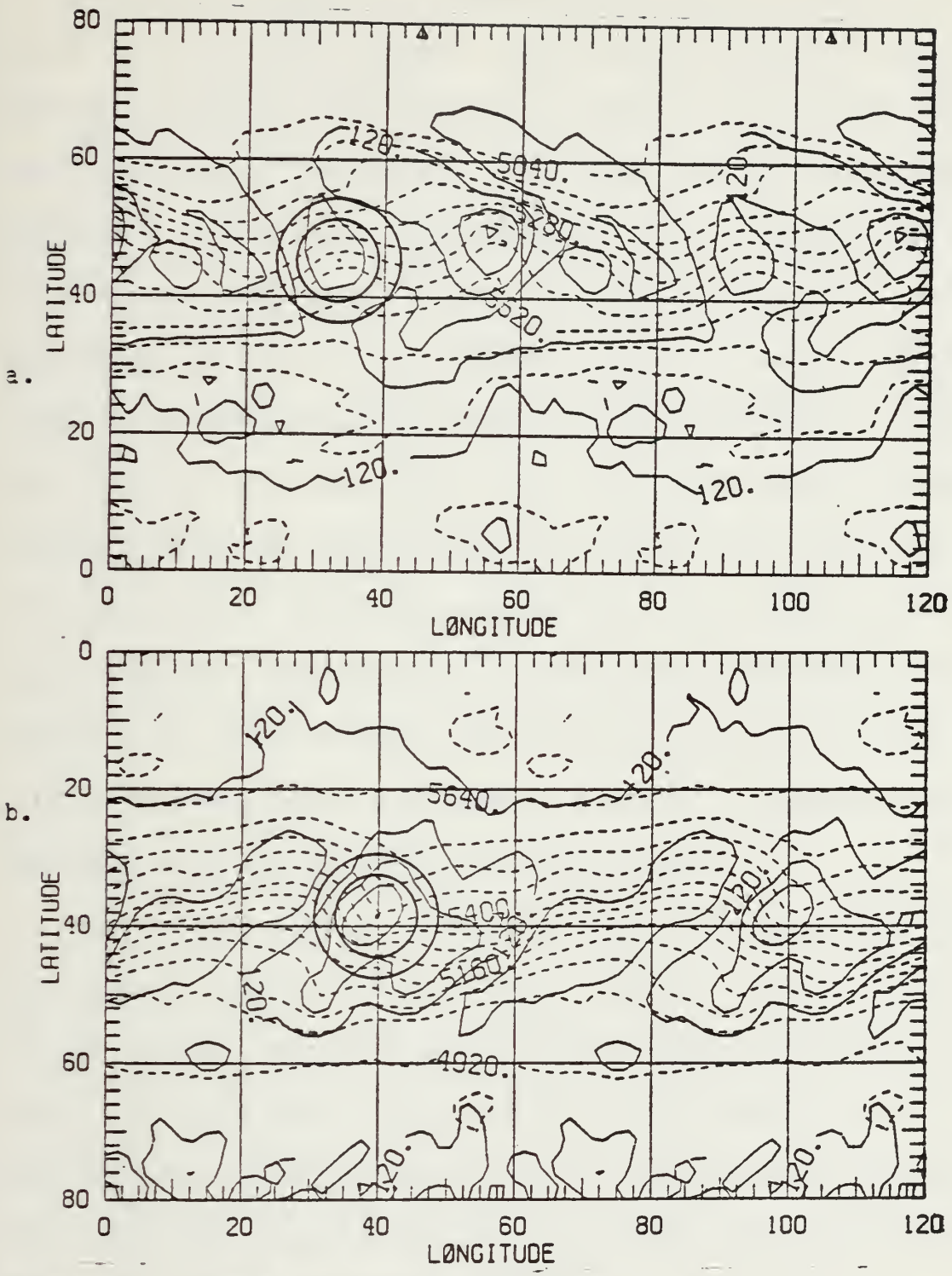

Figure 5. 1000 mb height and 1000 mb to mid-layer 4 thickness fields valid at initial time + 96 hours. 1000 mb height contours (solid) and thickness contours (dashed) are in meters. a. and b. as in Fig. 3.

Surface pressure and temperature fields at hour 120 are given in Fig. 6 with height and thickness fields in Fig. 7. During the period from hour 96 to hour 120, the NH lows move approximately 700 nm to the east while moving only slightly poleward. Cyclone N1 decreases to 992 mb and becomes the main surface low, while cyclone N2 decreases to only 998 mb. Approximately 70% of the surface pressure decrease experienced by cyclone N1 occurs during the latter half of this 24 hour period. In contrast, more than half of the surface pressure decrease experienced by cyclone N2 occurs during the first three hours of this period. It should be noted that cyclone N1 experiences a rapid central surface pressure decrease of 17 mb between hour 108 and hour 123. In the SH, cyclone S decreases to 986 mb at a nearly constant rate of approximately two millibars per three hours.

The thermal ridges associated with cyclones N1 and S are more pronounced than at hour 96; however, thermal advection at the surface increases very little during the period from hour 96 to hour 120. By the end of this period, pockets of warm air are coincident with the low pressure centers in the NH. However, cyclone N2 does not continue to develop and thus will not be discussed further.

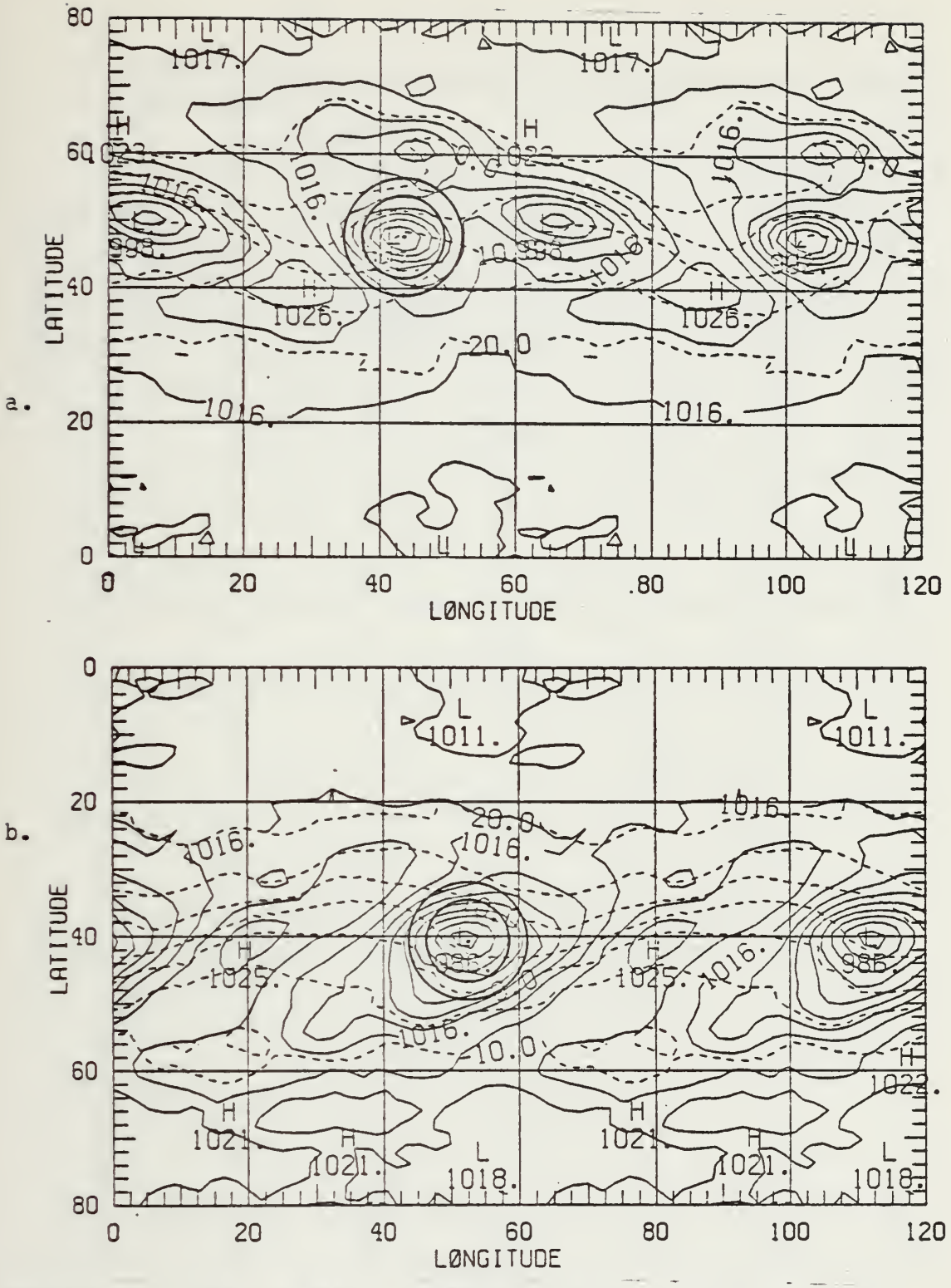

Figure 6. Same as Fig. 4 except for initial time + 120 hours.

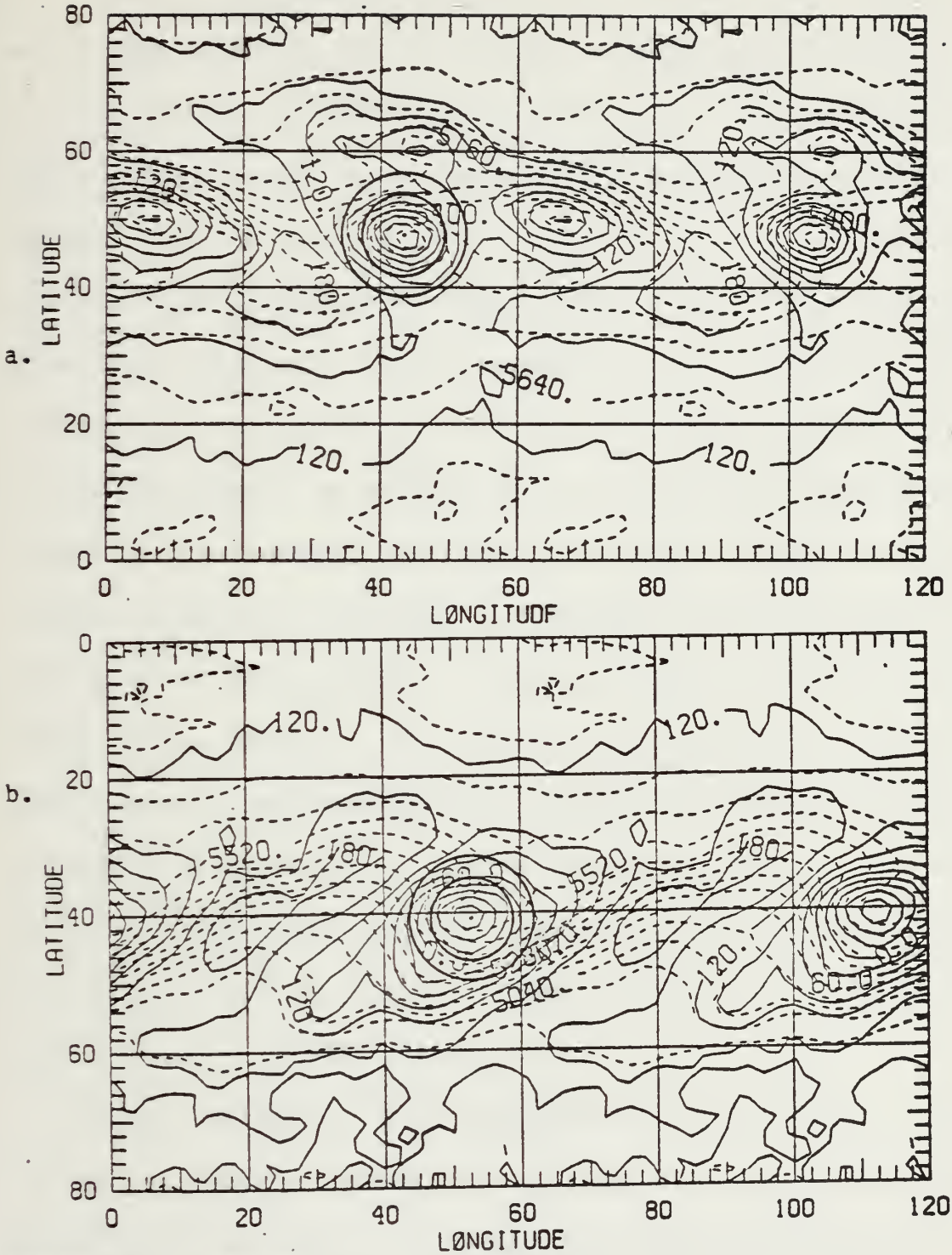

Figure 7. Same as Fig. 5 except for initial time + 120 hours.

The analyses for hour 144 are presented in Figs. 8 and 9. During the period from hour 120 to hour 144, cyclone N1 moves approximately 700 nm to the east-northeast (ENE) while cyclone S moves approximately 600 nm to the east-southeast (ESE). Cyclone N1 experiences little intensification as the central surface fluctuates between 992 and 987 mb with the lowest value occurring at hours 126 and 138. The low pressure area, initially to the northeast of cyclone N1, intensifies slightly and moves to a location approximatey 1000 nm to the northwest of cyclone N1 in an area of lower-tropospheric warm advection. During this same period, the central surface pressure of cyclone S decreases to 975 mb with more than half of this decrease occurring during the first three hours of the period. At hour 132 (not shown), a pocket of warm air is coincident with the surface center of cyclone S. A significant feature of the NH thickness field is the north to south orientation and the amplitude of the thermal ridge. In contrast, the SH thermal ridge is oriented nearly west to east and is extremely elongated.

Surface pressure and temperature fields valid at hour 168 are presented in Fig. 10 with the height and thickness fields given in Fig. 11. During the period from hour 144 to

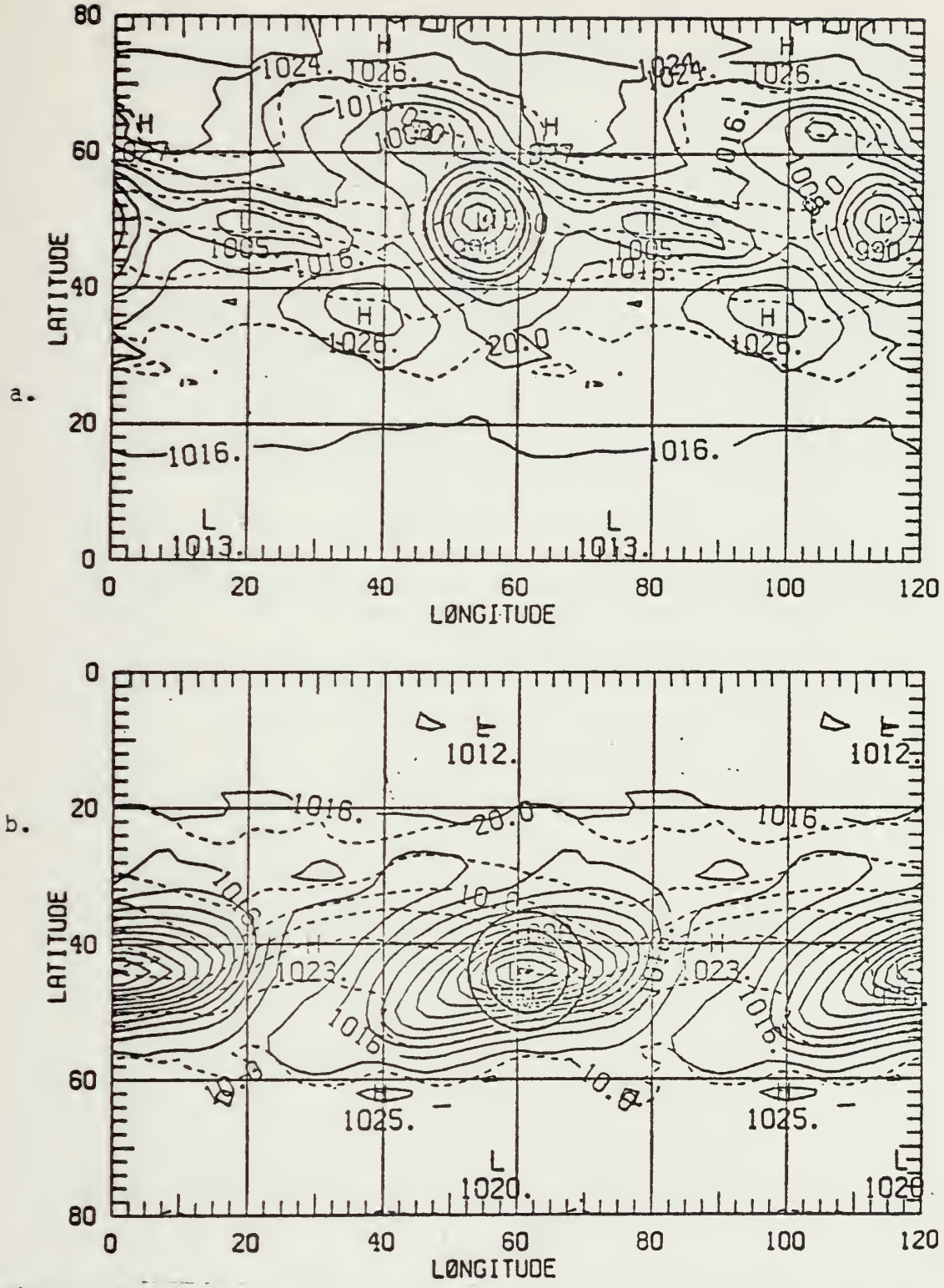

Figure 8. Same as Fig. 4 except for initial time + 144 hours.

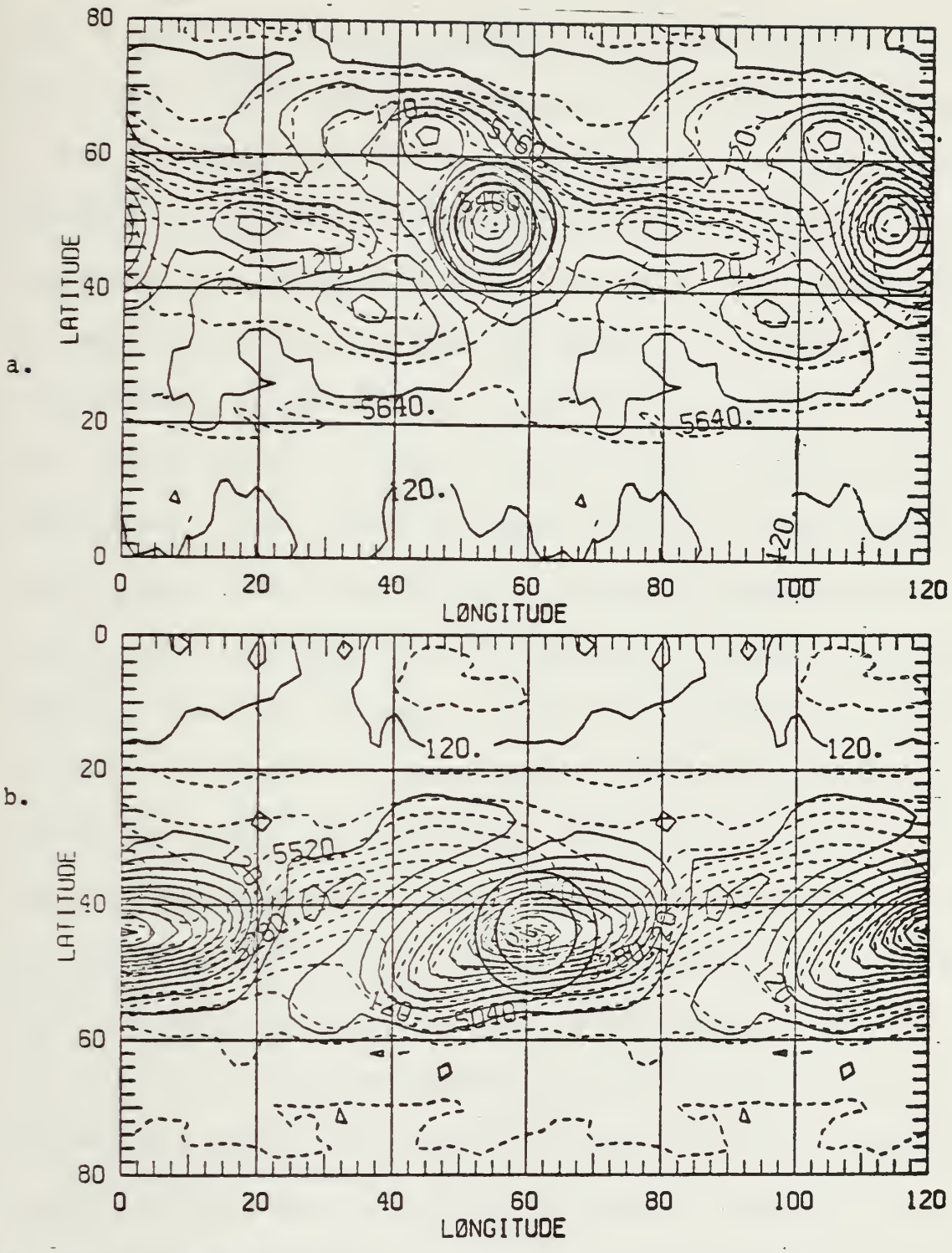

Figure 9. Same as Fig. 5 except for initial time + 144 hours.

hour 156 hours, cyclone N1 remains relatively steady-state with a central surface pressure of approximately 988 mb while the central surface pressure of cyclone S rises 5 mb to 980 mb. From hour 156 to hour 168, the central surface pressure of cyclone N1 decreases to 984 mb while cyclone S remains nearly constant at about 980 mb. During the final 24 hours of this study, the NH thermal ridge shifts from a north-south orientation to a northwest-southeast orientation. However, the SH thermal ridge maintains its west-east orientation. The 1000 mb height contours nearly parallel the thickness contours poleward of each cyclone so there is little warm advection in the vicinity of these cyclones; however, cold air advection continues equatorward of each cyclone. During the period from hour 144 to hour 162, cyclone N1 moves approximately 300 nm to the NNE. It appears that cyclone N1 moves approximately 360 nm during the last six hours of this study; however, this apparent rapid movement may actually be a reformation of the low in the vicinity of the low pressure area located northwest of cyclone N1 at hour 144. Cyclone S also exhibits an apparent rapid movement during the final 24 hours of simulation, moving approximately 720 nm to the ESE. Approximately 500 nm

of this movement occurs during the period from hour 150 to hour 162 as the central surface pressure increases three millibars to 979 mb. As in the NH, it is possible that this apparent rapid movement is a reformation of cyclone S. However, unlike the NH case, there is no secondary low or warm pocket in the vicinity of the new location of cyclone S.

C. MID-LEVEL FEATURES

In this section mid-tropospheric features are discussed using mid-layer 4 of the model (approximately 500 mb). Mid-layer 4 height and temperature fields valid at hour 96 are depicted in Fig. 12 with the vorticity and wind fields given in Fig. 13. A weak short wave within nearly zonal flow is apparent in each hemisphere. The height and temperature fields are nearly in phase so there is little thermal advection in either hemisphere. Developing cyclones N1 and S are located under the short wave ridges in the respective hemispheres with a weak vorticity maximum located 300 to 400 nm to the west of each cyclone. Mid-tropospheric wind flow patterns indicate weak cyclonic vorticity advection (CVA) over each cyclogenesis area.

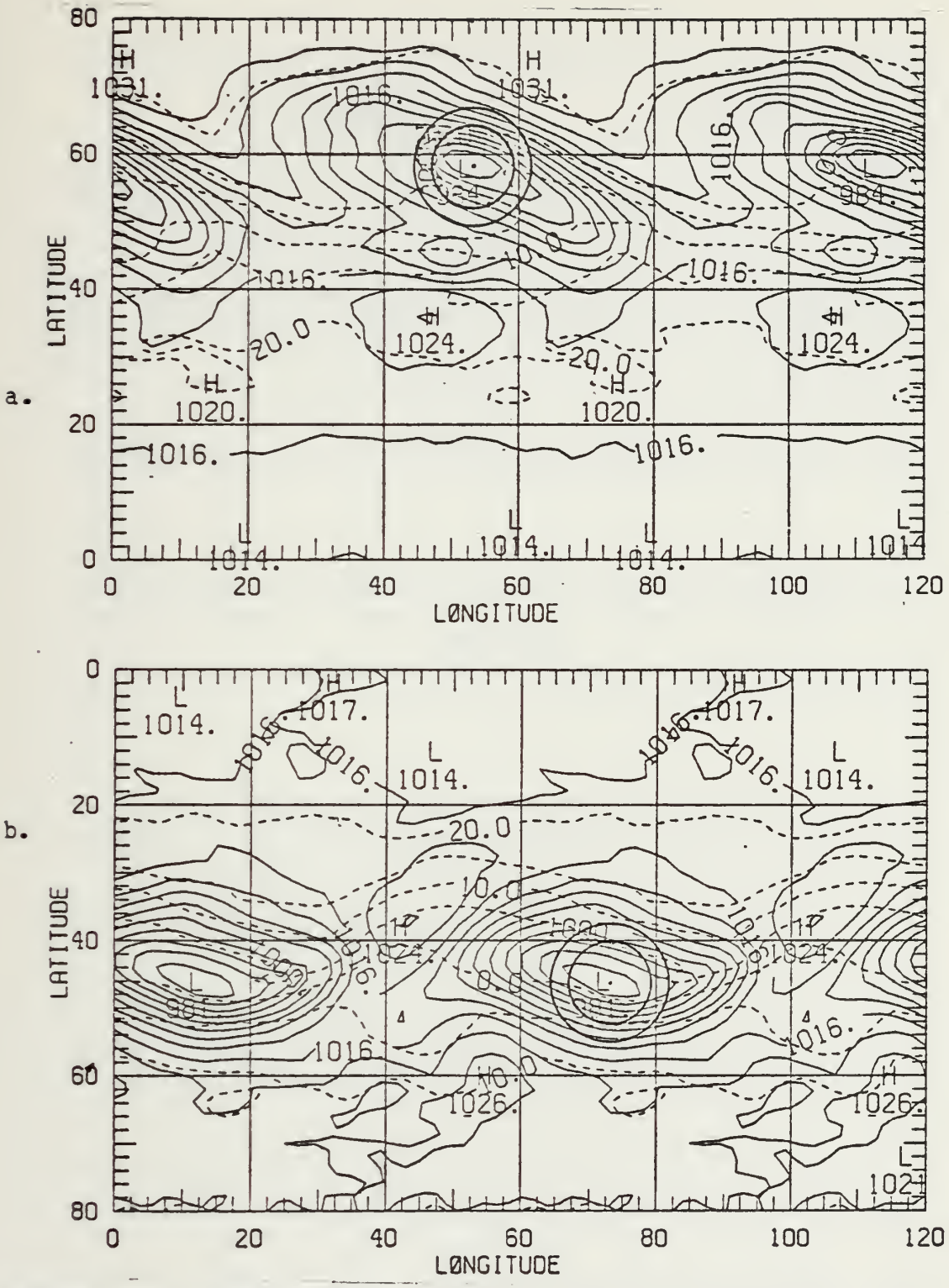

Figure 10. Same as Fig. 4 except for initial time + 168 hours.

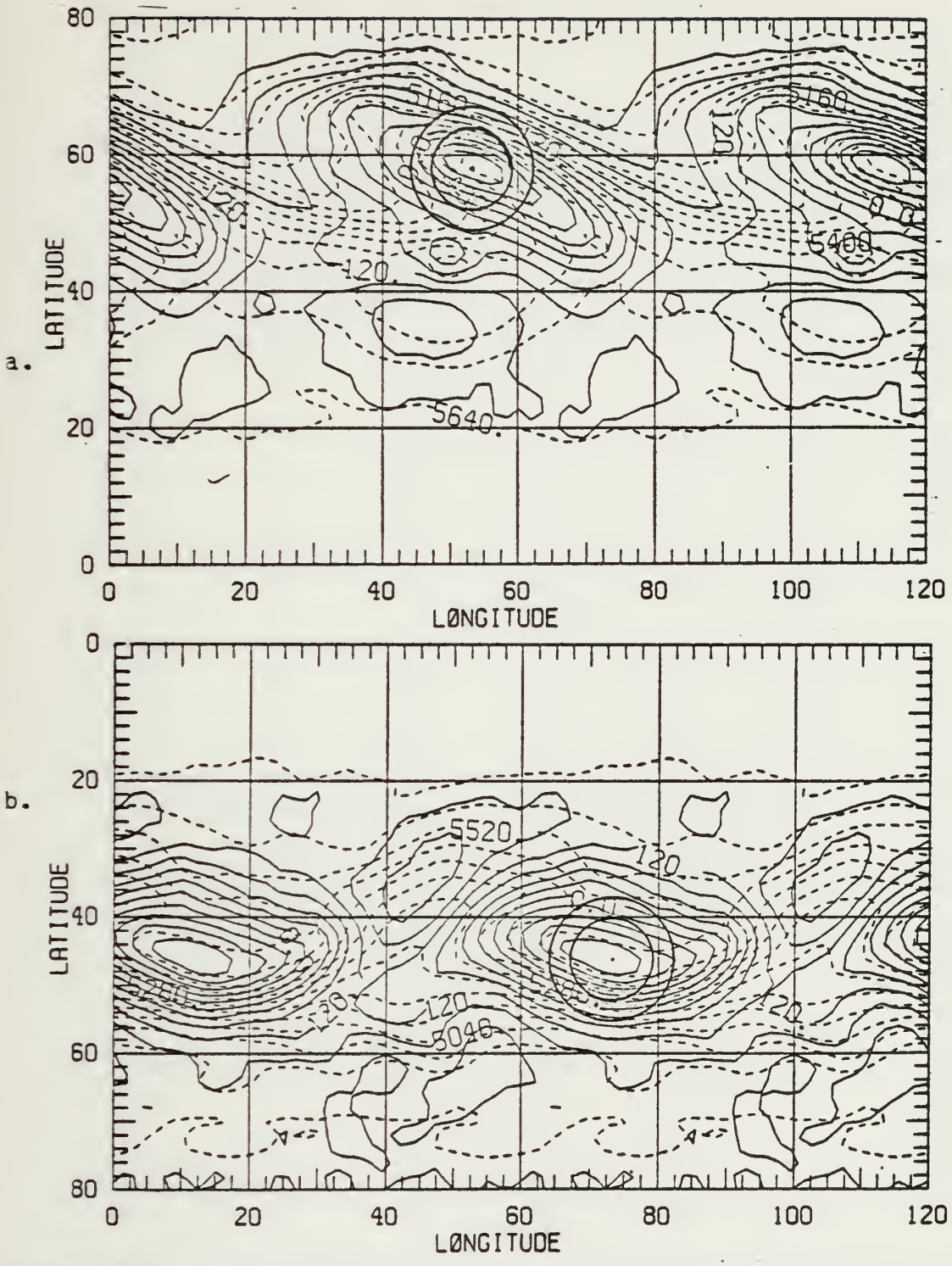

Figure 11. Same as Fig. 5 except for initial time + 168 hours.

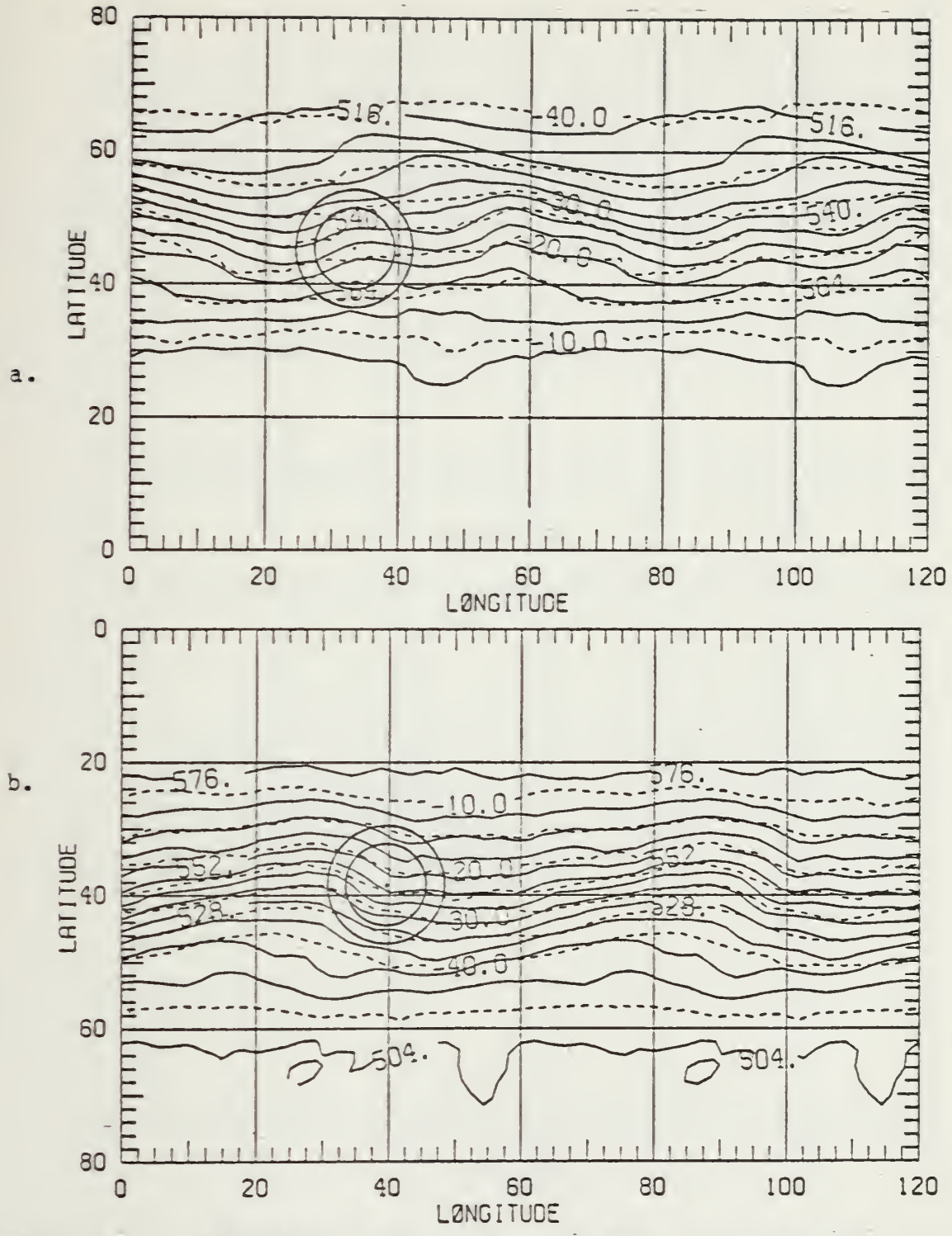

Figure 12. Mid-layer 4 height and temperature fields valid at initial time + 96 hours. Height contours (solid) are in decameters. Isotherms (dashed) are in °C. a. and b. as in Fig. 3.

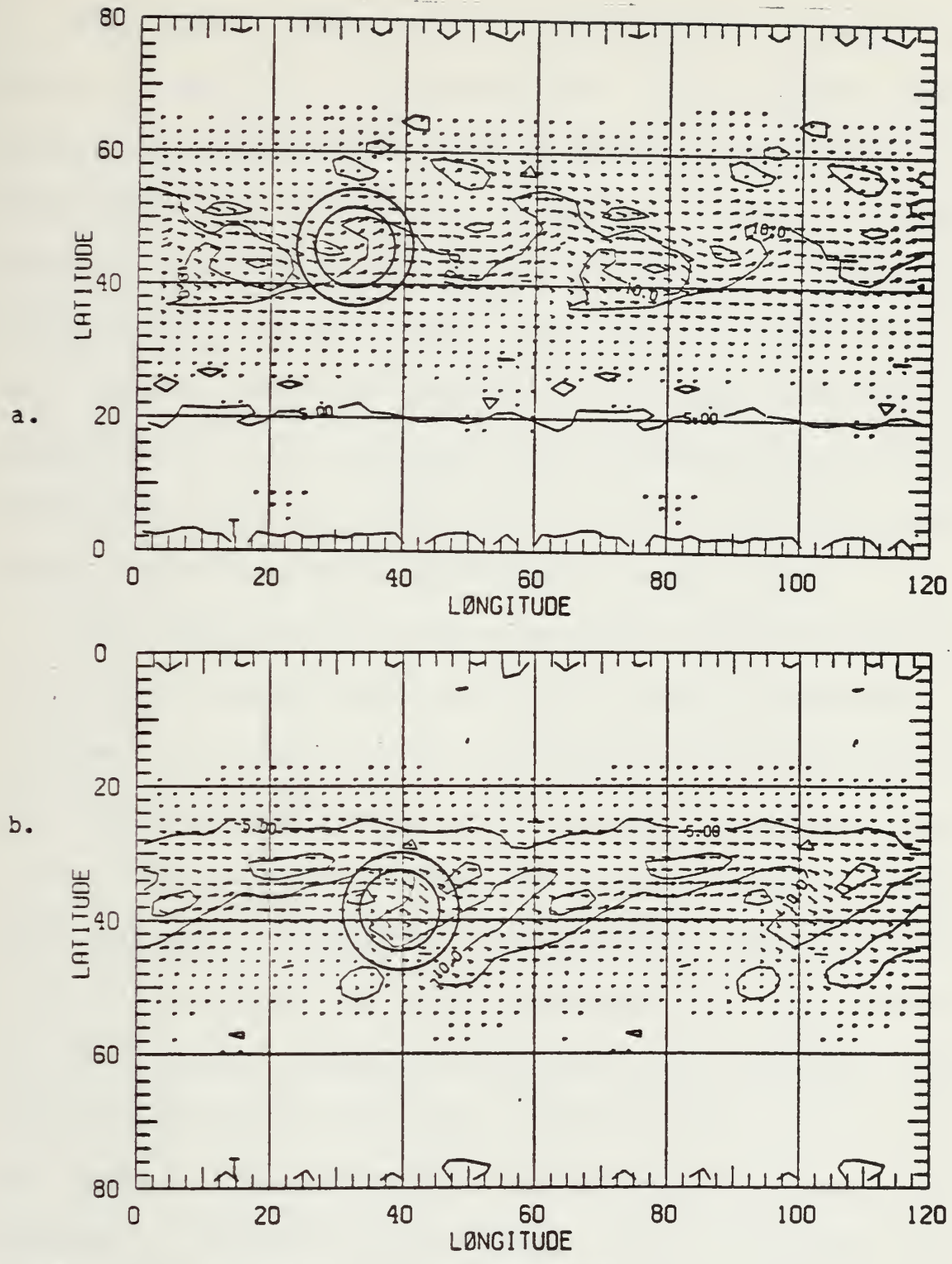

Figure 13. Mid-layer 4 absolute vorticity (sec^{-1}) and wind fields valid at initial time + 96 hours. Absolute vorticity ($\times 10^{-5}$) contours are solid. a. and b. as in Fig. 3.

Mid-layer 4 fields valid at hour 120 are presented in Figs. 14 and 15. The height and thermal fields remain nearly in phase with weak cold advection immediately to the west of the center of cyclone N1 and warm advection approximately 5 degrees longitude further to the west. During the first 24 hours of this study, the amplitude of the NH short wave doubles while that of the SH short wave increases by approximately 70%. This amplitude intensification is nearly simultaneous with the most rapid surface development which occurs during the period from hour 96 to hour 126.

The orientation of the NH short wave trough is northwest to southeast while that of the SH short wave is southwest to northeast as each cyclone maintains its position relative its associated short wave. The cyclonic vorticity maximum in the NH increases in magnitude and is located directly over cyclone N1 resulting in anticyclonic vorticity advection (AVA) west of the center of cyclone N1. The increase in the vorticity maximum at mid-layer 4 and the most rapid surface development also occur simultaneously. In the SH, the cyclonic vorticity maximum also increases in magnitude; however, in contrast to the NH case, the SH vorticity maximum does not move over the storm center. Instead the

vorticity maximum moves to the east as cyclone S moves southeasterly to a position poleward of the vorticity maximum. As in the NH case, intensification of the vorticity maximum occurs simultaneously with the most rapid surface development. Zero vorticity advection occurs over cyclone S while strong CVA occurs to the north and northeast.

Mid-tropospheric fields valid at hour 144 are given in Figs. 16 and 17. The amplitude of each short wave continues to increase and the orientation of the trough axes becomes more west-east. Extremely sheared flow is evident in the SH and, to a lesser degree, in the NH. The short waves and their associated cyclones maintain their positions relative to each other during the period between hours 120 and 144 as the height and thermal fields remain nearly in phase. Although maintaining its position over cyclone N1, the vorticity maximum in the NH weakens, having reached a peak at hour 132 (not shown). As in the NH case, the SH vorticity maximum reaches its peak at hour 132 and maintains its position relative to cyclone S. In each case, the vorticity patterns are quite elongated, because of the extreme shear present in the wind field.

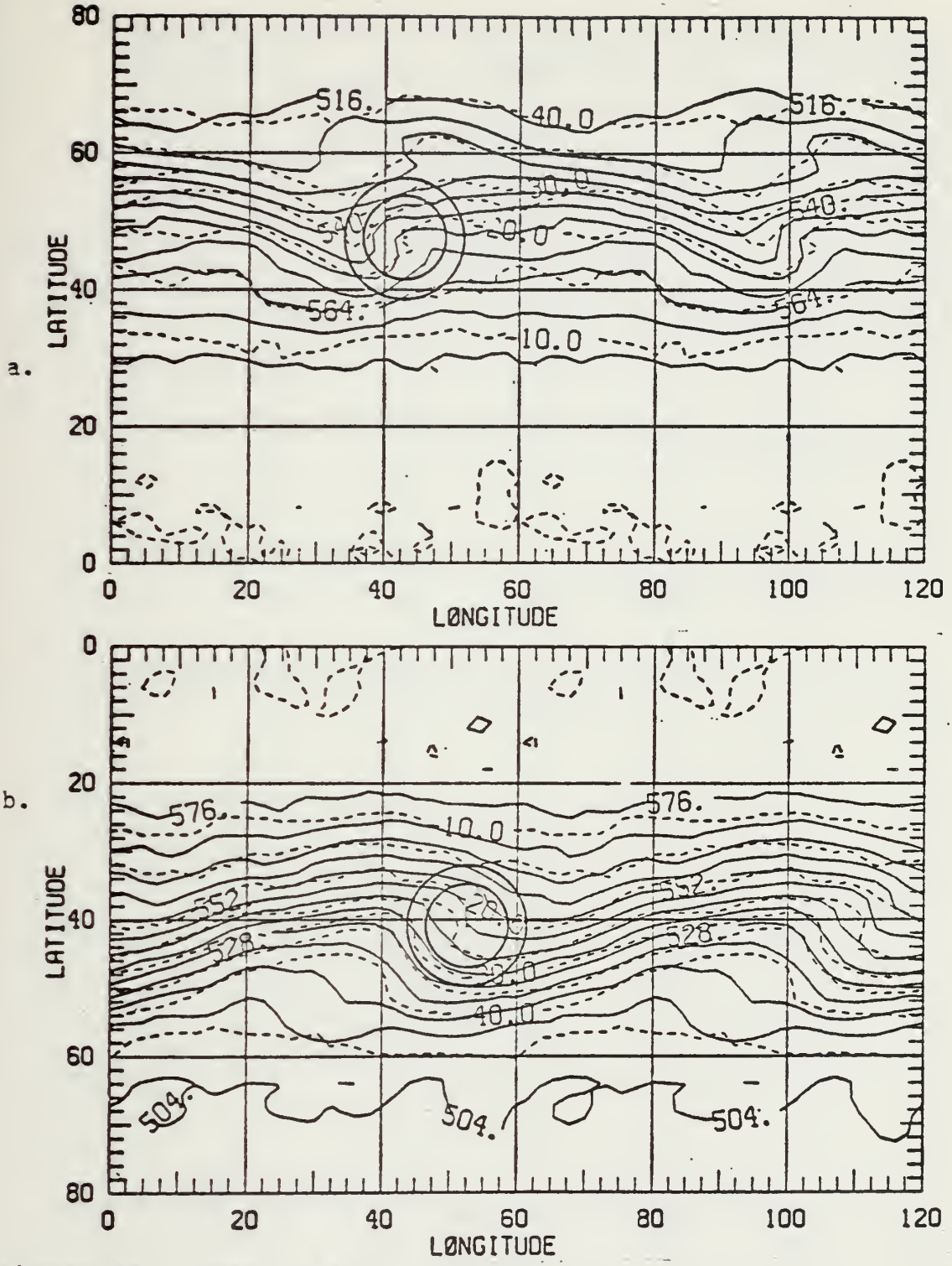

Figure 14. Same as Fig. 12 except for initial time + 120 hours.

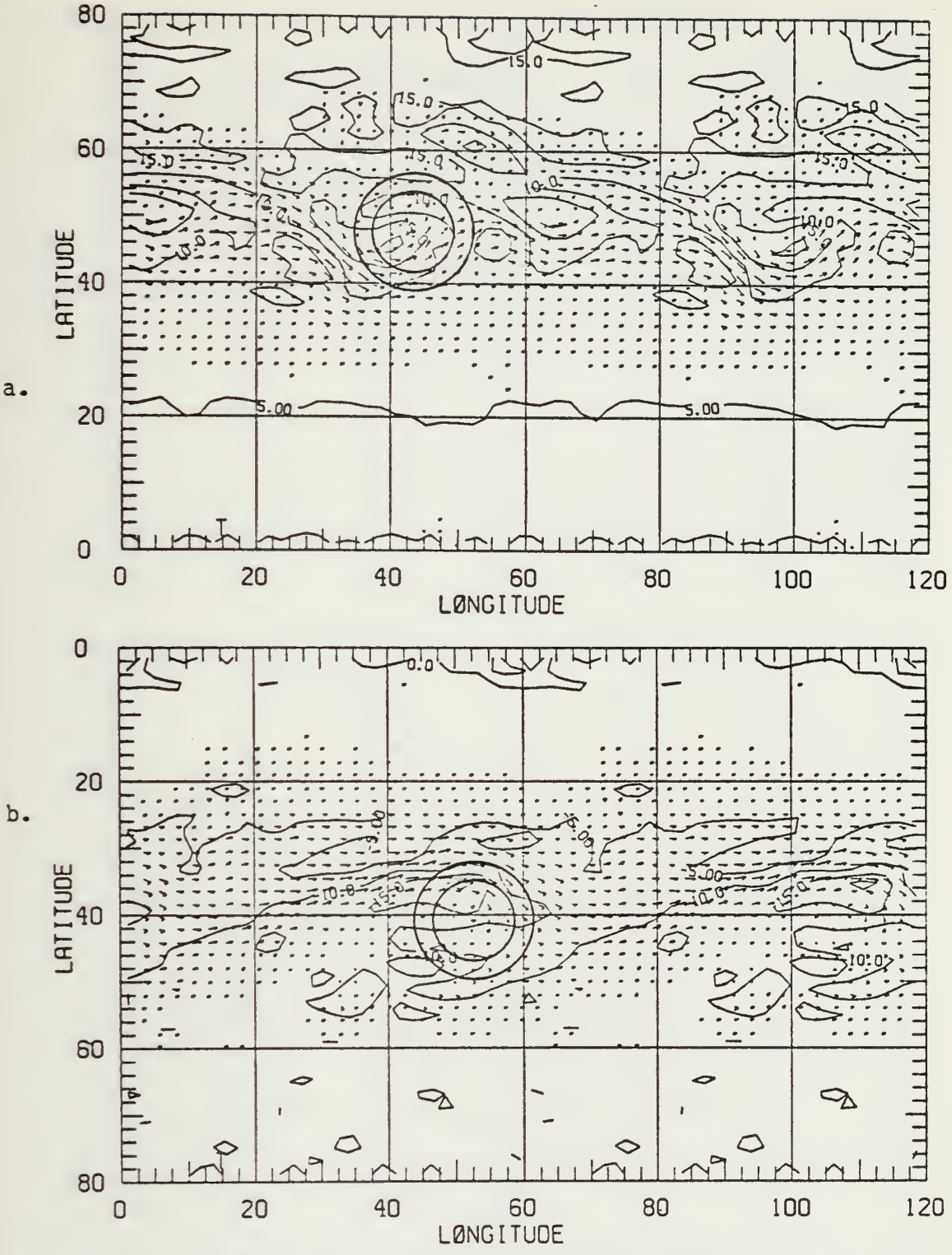

Figure 15. Same as Fig. 13 except for initial time + 120 hours.

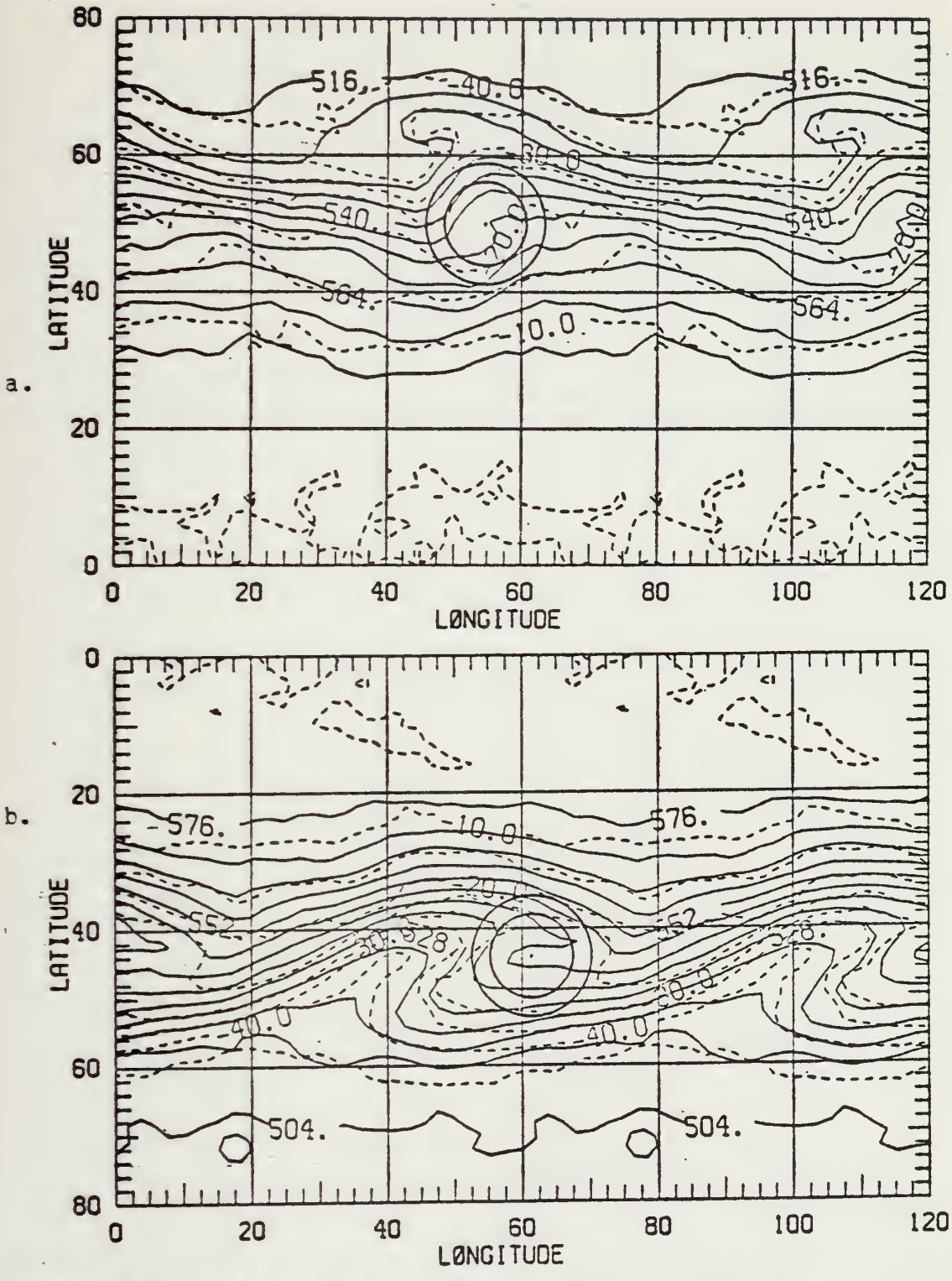

Figure 16. Same as Fig. 12 except for initial time + 144 hours.

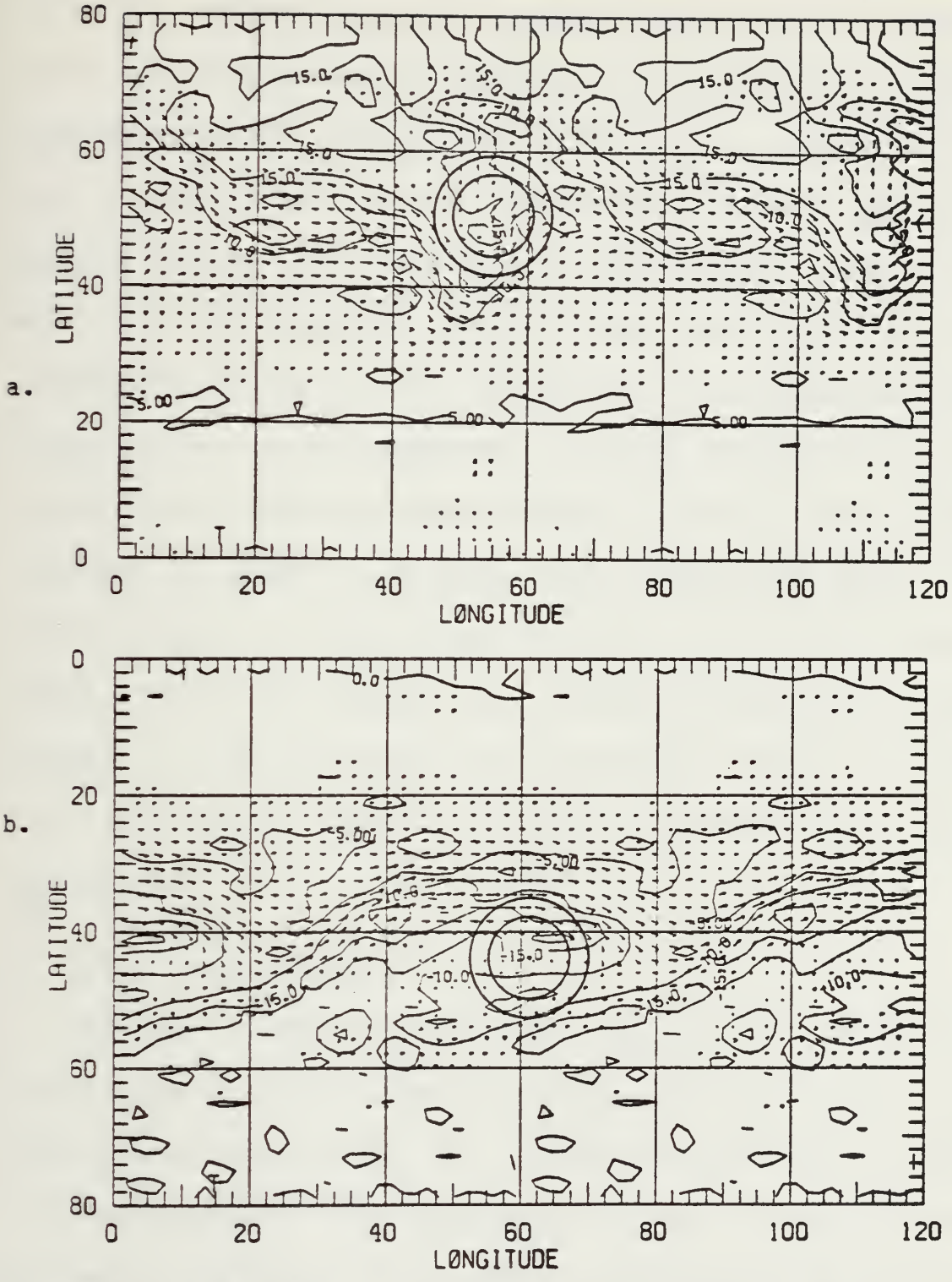

Figure 17. Same as Fig. 13 except for initial time + 144 hours.

At hour 168 (Figs. 18 and 19), cyclone N1 is positioned under the inflection point ahead of the trough. The NH short wave continues to amplify and the shearing is more pronounced as the axis of the short wave is nearly east to west. Between hours 144 and 168, the SH upper trough fills leaving a split flow pattern with nearly zonal flow to the south and the weakening trough to the north of 46S, the latitude of cyclone S. A weak closed low appears approximately 700 nm to the northwest, however cyclone S fails to develop into a deep cold core vortex. The vorticity fields continue to weaken and become more elongated during the final 24 hours of this study. Broad, relatively uniform areas of cyclonic vorticity are located equatorward of each cyclone. These vorticity patterns nearly parallel the wind flow indicating little vorticity advection in either hemisphere.

D. UPPER-LEVEL FEATURES

Mid-layer 3 (approximately 300 mb) height and temperature fields valid at hour 96 are given in Fig. 20 with the wind fields given in Fig. 21. Nearly zonal flow is evident with weak cyclonic flow 700 nm to the west of each cyclone and weak anticyclonic flow 1000 nm and 2000 nm to the east

of cyclones N1 and S respectively. The two jets, centered near 45N and 35S, are nearly zonal and somewhat stronger than those in the initial field. The NH and SH jet maxima, approximately 45 m sec^{-1} and 55 m sec^{-1} respectively, are located 900 to 1500 nm to the west of the developing cyclones.

During the first 24 hours of this study, the flow immediately to the west of each cyclone becomes increasingly cyclonic as the amplitude of the trough/ridge system increases. At hour 120 (Figs. 22 and 23) the cyclones are positioned slightly east and poleward of the base of the trough. The jet maximum in the NH increases only slightly while the SH jet maximum increases to over 60 m sec^{-1}. These jets are located approximately 600 nm west of the base of the respective troughs.

The upper-level charts valid at 144 hours are shown in Figs. 24 and 25. In the NH, cyclone N1 is located ahead of the trough under nearly meridional flow with a jet maximum of over 40 m sec^{-1} located approximately 500 nm to the southeast and a secondary jet maximum, also greater than 40 m sec^{-1}, located near the top of the ridge, approximately 600 nm to the north of cyclone N1. In the SH, there are two

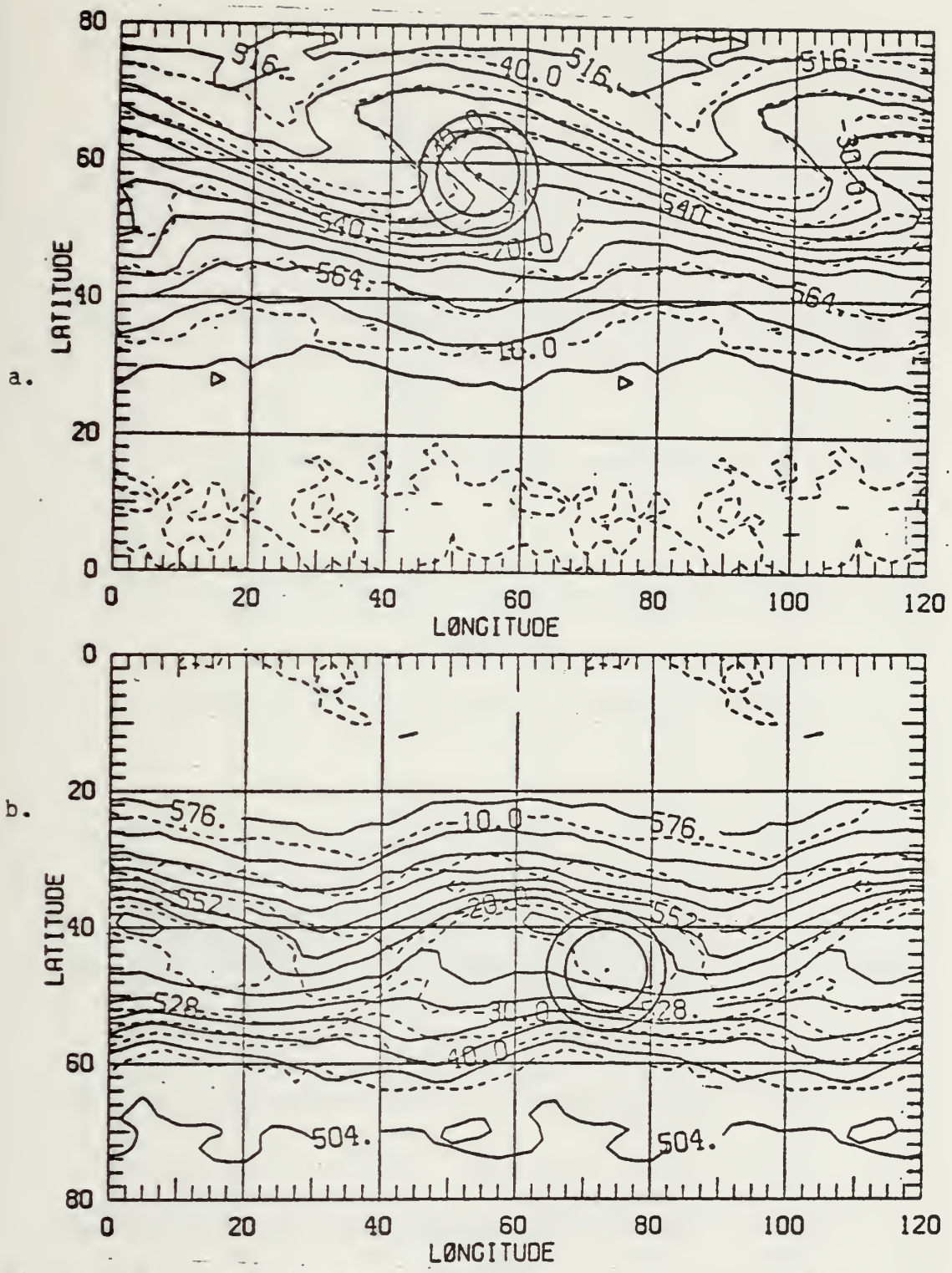

Figure 18. Same as Fig. 12 except for initial time + 168 hours.

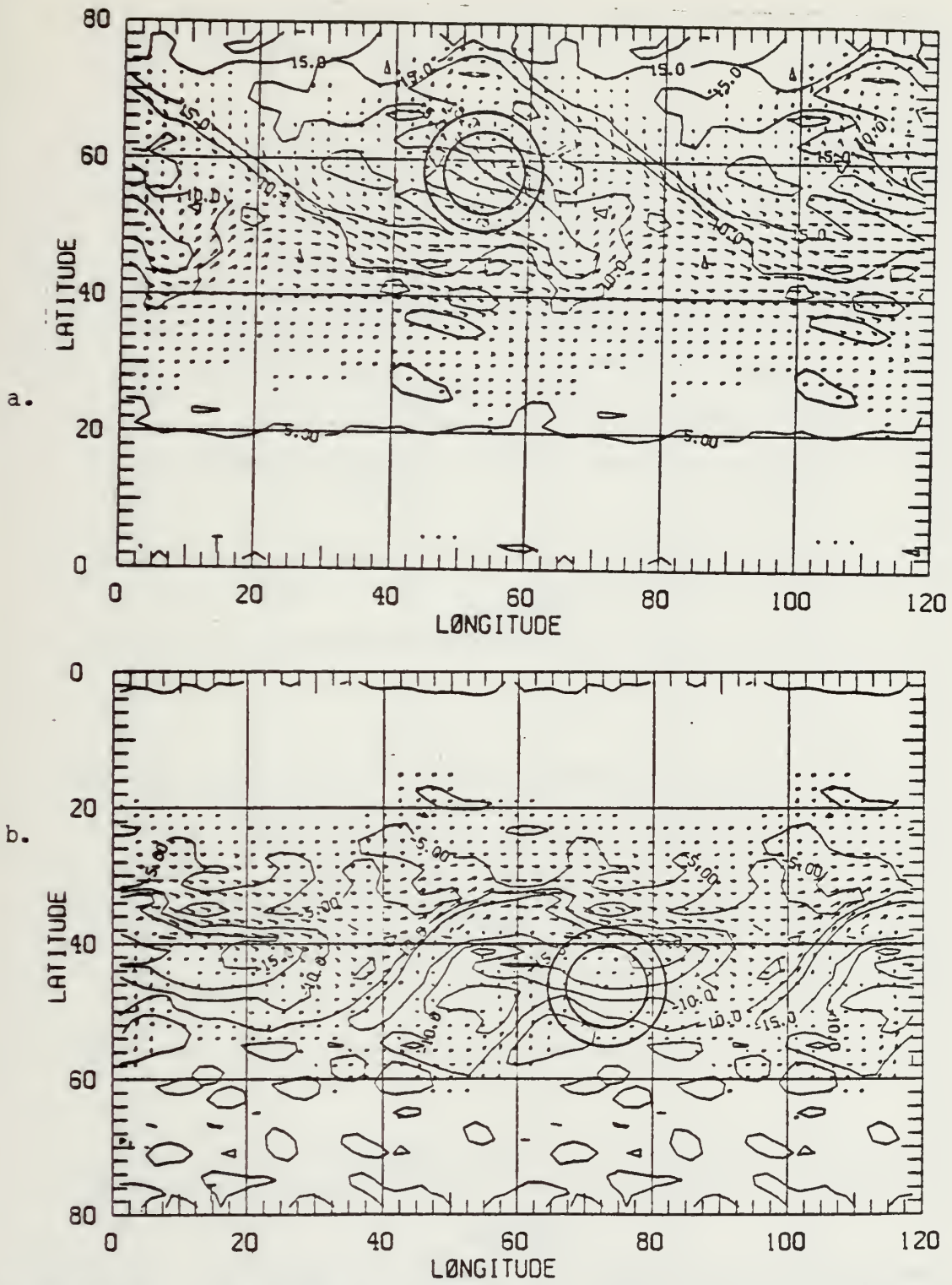

Figure 19. Same as Fig. 13 except for initial time + 168 hours.

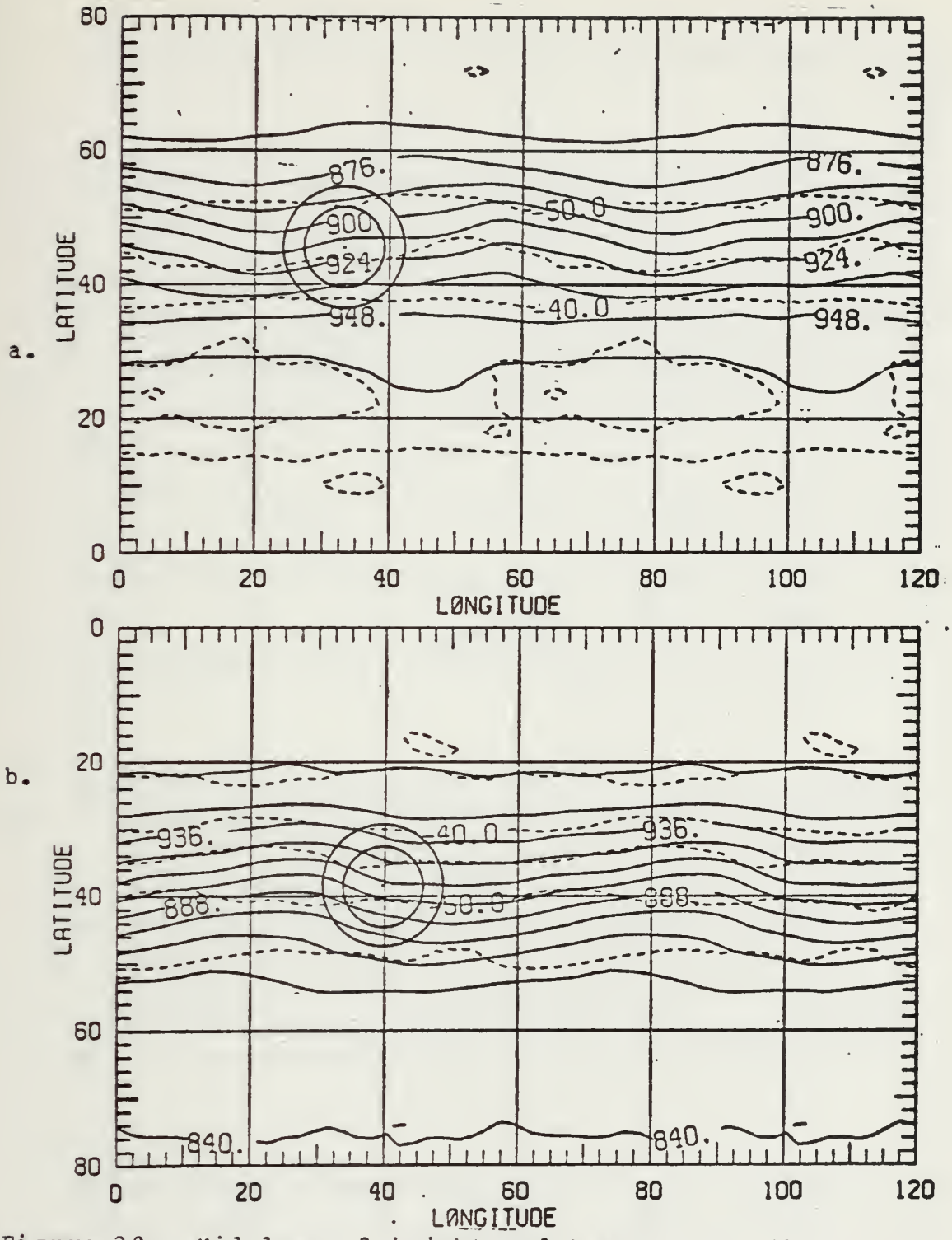

Figure 20. Mid-layer 3 height and temperature fields valid at initial time + 96. Height contours (solid) are in decameters. Isotherms (dashed) are in °C. a. and b. as in Fig. 3.

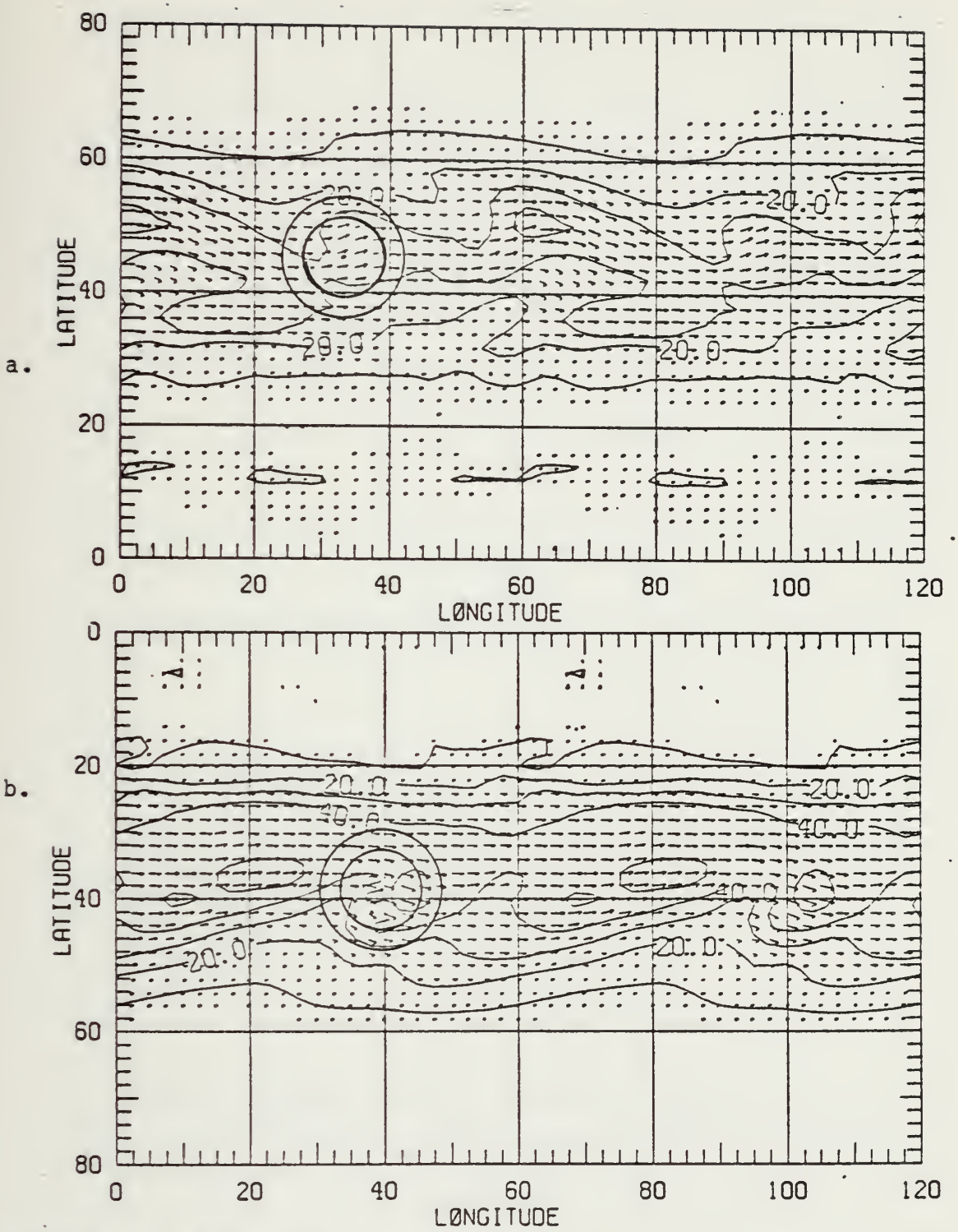

Figure 21. Mid-layer 3 wind vectors and isotachs valid at initial time + 96. Isotachs (solid) in m sec^{-1}. a. and b. as in Fig. 3.

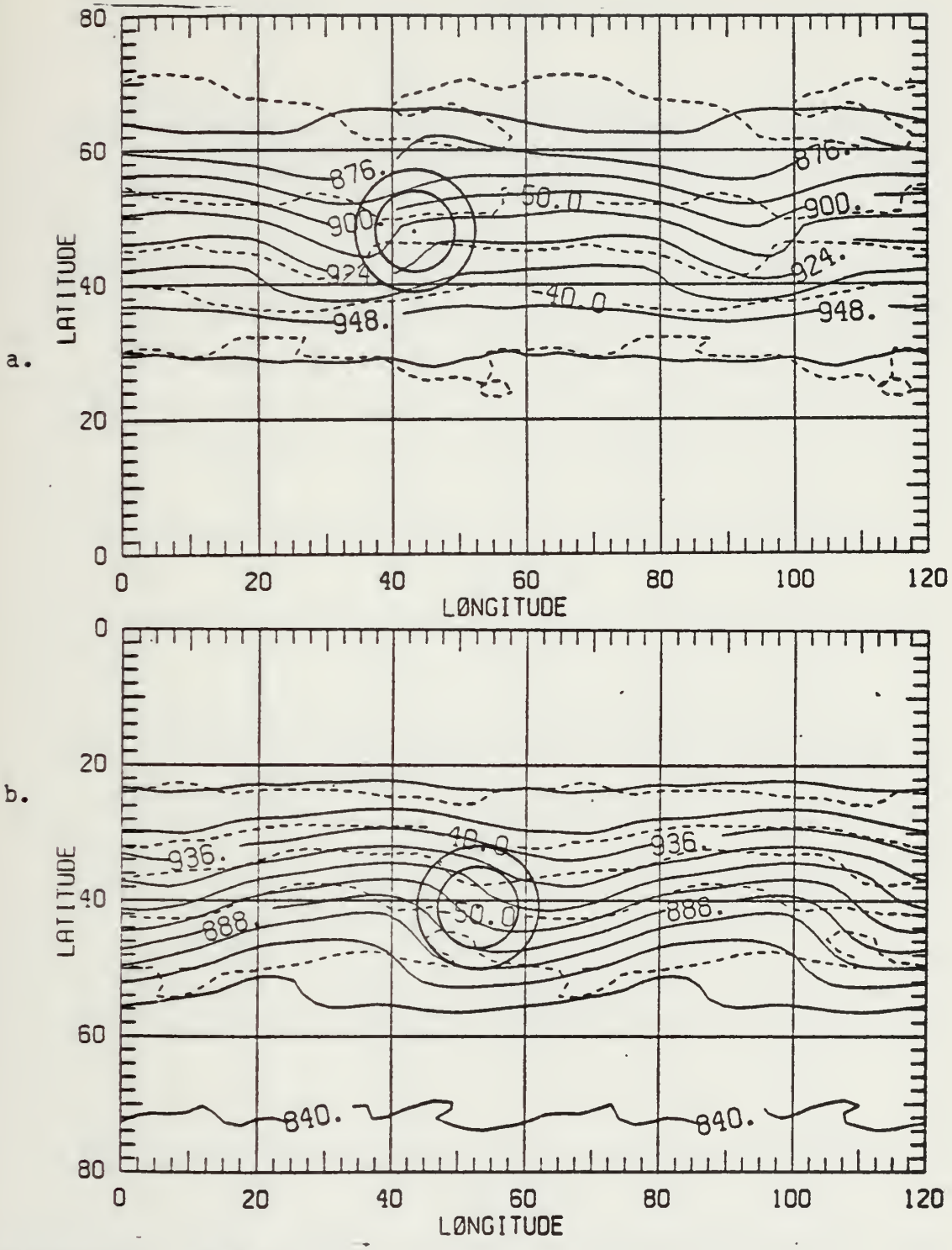

Figure 22. Same as Fig. 20 except for initial time + 120 hours.

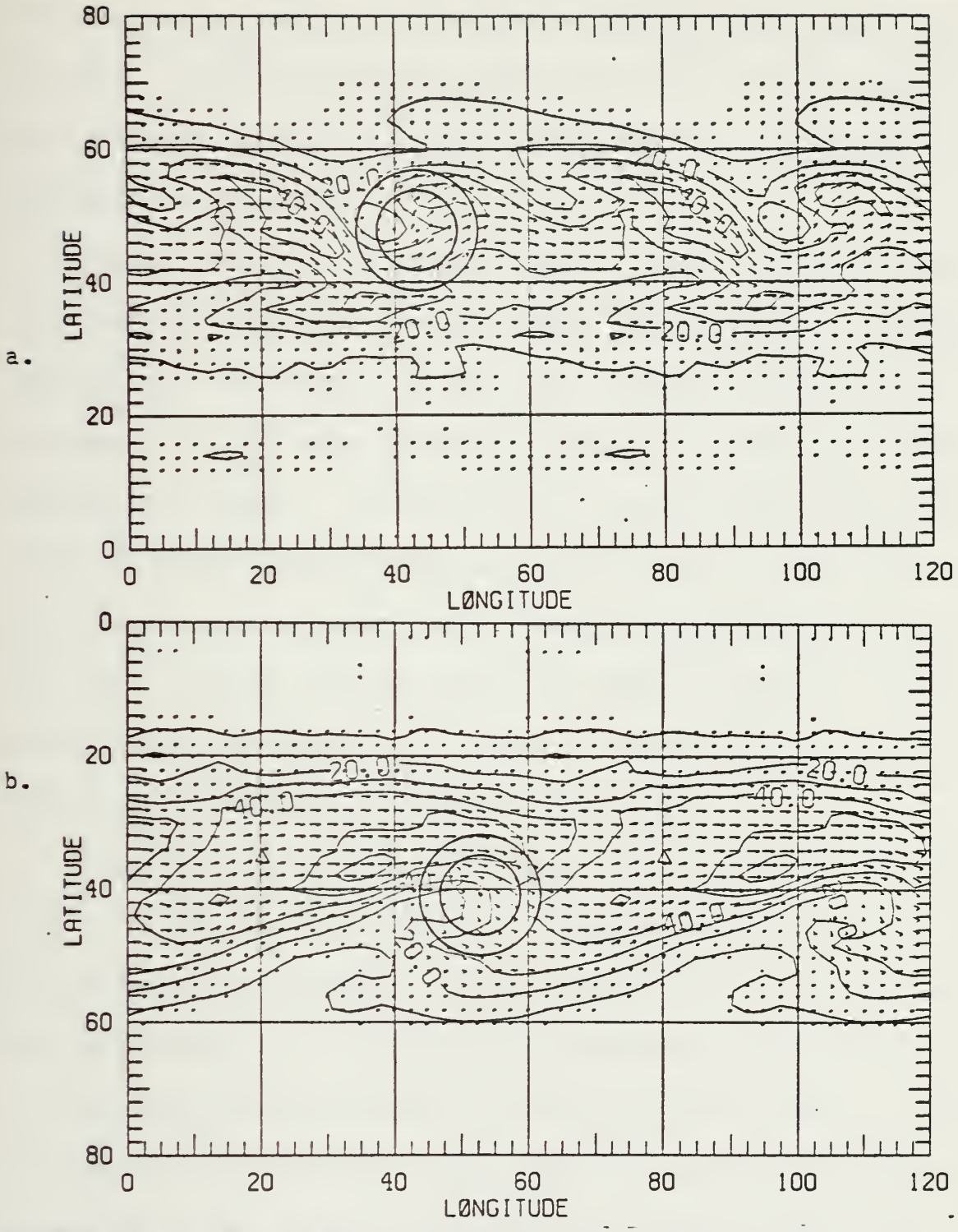

Figure 23. Same as Fig. 21 except for initial time + 120 hours.

jet maxima (each greater than 50 m sec^{-1}) associated with cyclone S--one behind the trough and one in the base of the trough. In each hemisphere the flow ahead of the trough is basically meridional and the short waves are continuing to increase in amplitude.

The mid-layer 3 wind field valid at hour 156 (not shown) is characterized by several small disjointed jet maxima greater than 40 m sec^{-1} in the NH. There appears to be no organization to these areas as some are ahead and some behind the trough. By this time, the SH trough has tilted back on itself and is oriented nearly west to east and the flow south of the trough is now zonal. A developing cut-off low is indicated by the extreme shear in the SH height field. Similar directional shear is present in the NH, although not to the extent of that in the SH.

Figs. 26 and 27 depict the mid-layer 3 patterns at hour 168. In the NH, the position of cyclone N1 relative to the trough remains unchanged during the final 24 hours of this study. However, an organized jet maximum of over 40 m sec^{-1} to the west is approaching the base of the trough. This maximum is a result of the cyclic continuity assumption employed by the model and is the same maximum which was in

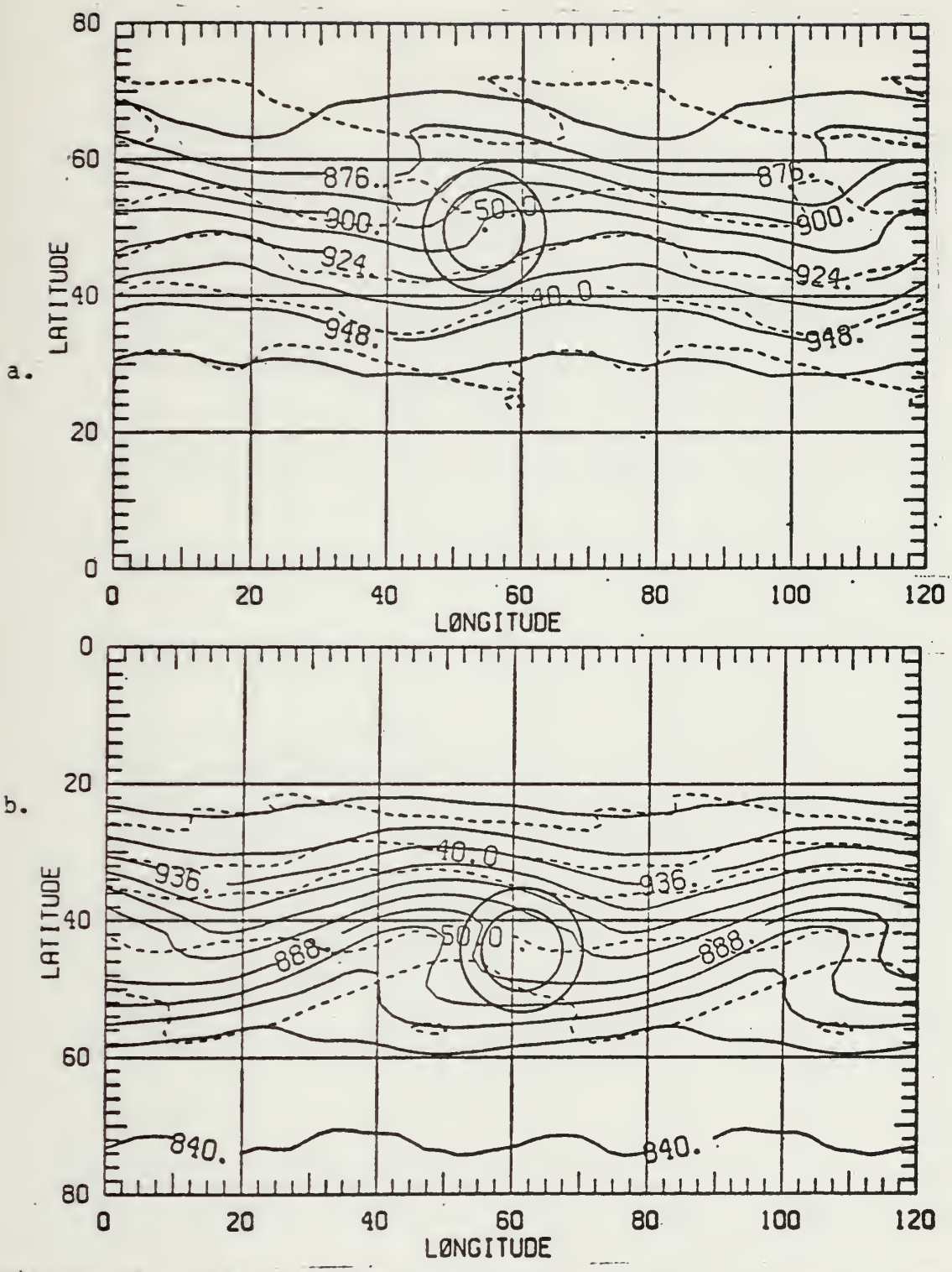

Figure 24. Same as Fig. 20 except for initial time + 144 hours.

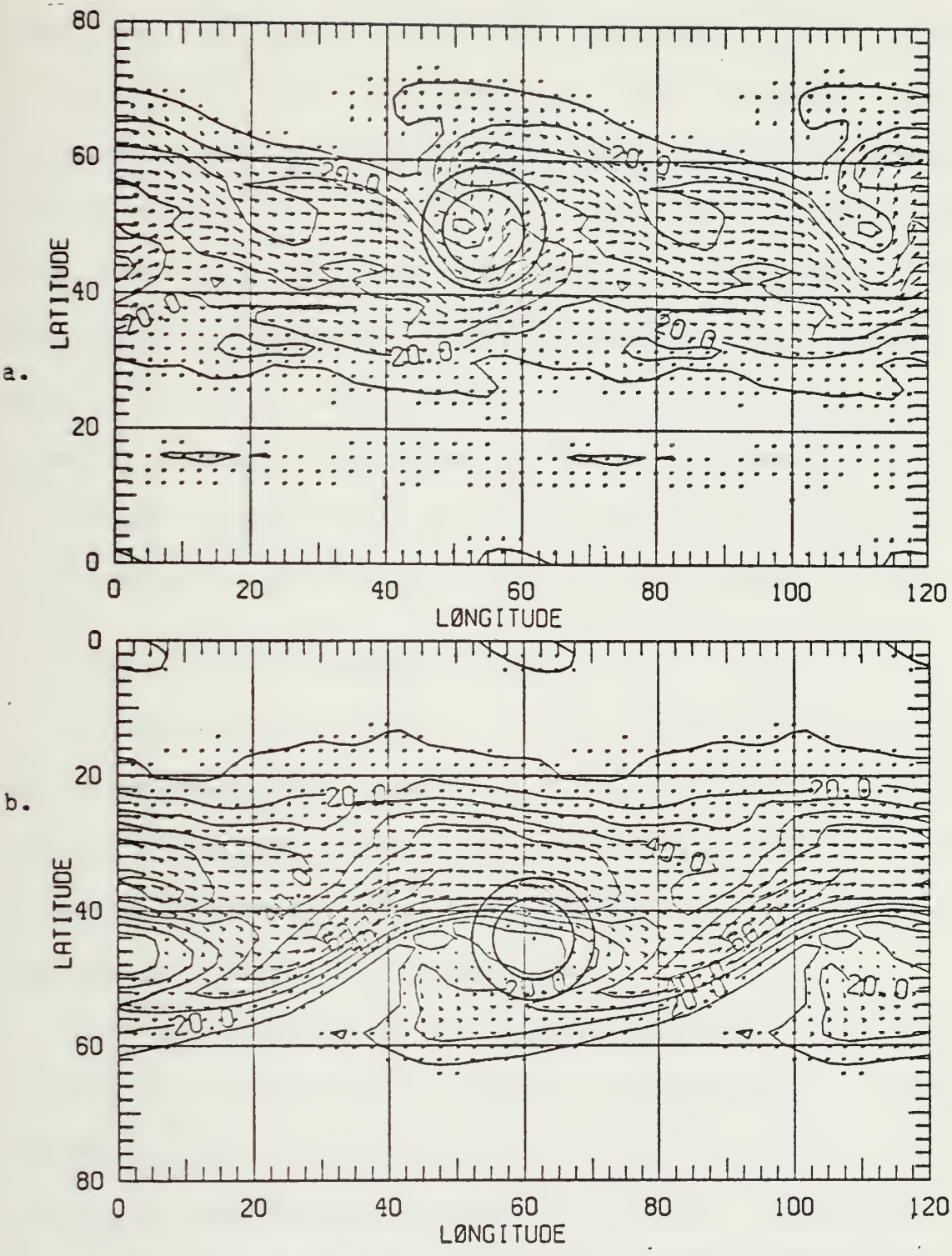

Figure 25. Same as Fig. 21 except for initial time + 144 hours.

the downstream ridge (north of the cyclone) at approximately hour 144. The flow directly over and north of the cyclone N1 remains basically meridional but shifts somewhat to the northwest producing stronger directional shear to the northwest of cyclone N1. In the SH, a jet maximum greater than 60 m sec^{-1} is centered in the base of the trough 750 nm equatorward of cyclone S, which is located under a region of very weak flow at mid-layer 3. A weak closed low at mid-layer 3 is located approximately 700 nm northwest of cyclone S, almost directly over the weak closed low at mid-layer 4. The flow equatorward of each cyclone continues to be zonal.

E. COMPARISON TO OBSERVED CYCLONES

A superficial analysis of model cyclogenesis might give the impression that these storms are realistic in every aspect. A closer examination reveals them to have a number of unusual features. In this section, the realistic and anomalous features will be summarized.

Although cyclone S is more intense, the overall development of both model cyclones resembles that of storms observed in the North Atlantic by Petterssen, et al. (1962). The model cyclongenesis begins in the lower troposphere in the vicinity of a baroclinic zone, under nearly zonal flow

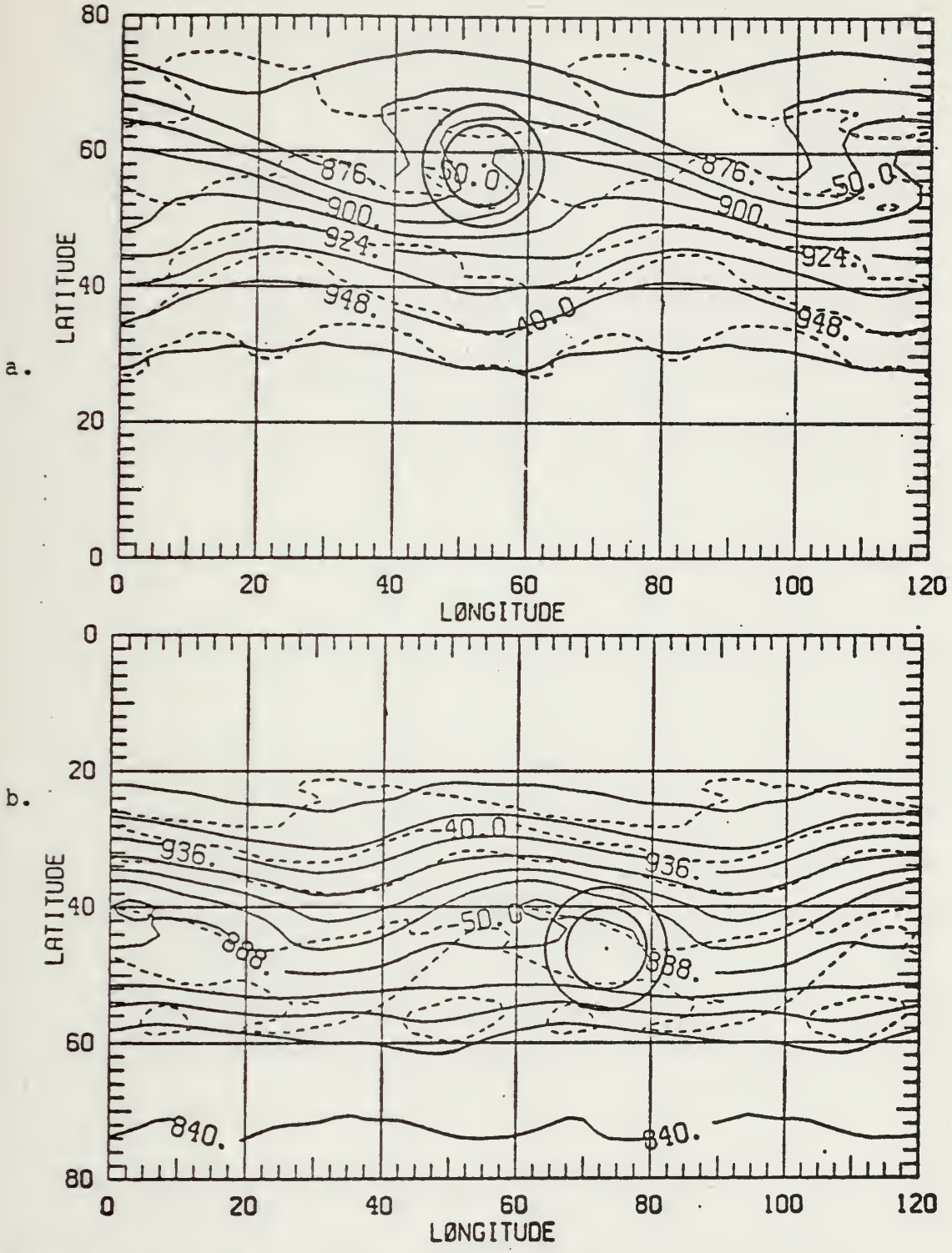

Figure 26. Same as Fig. 20 except for initial time + 168 hours.

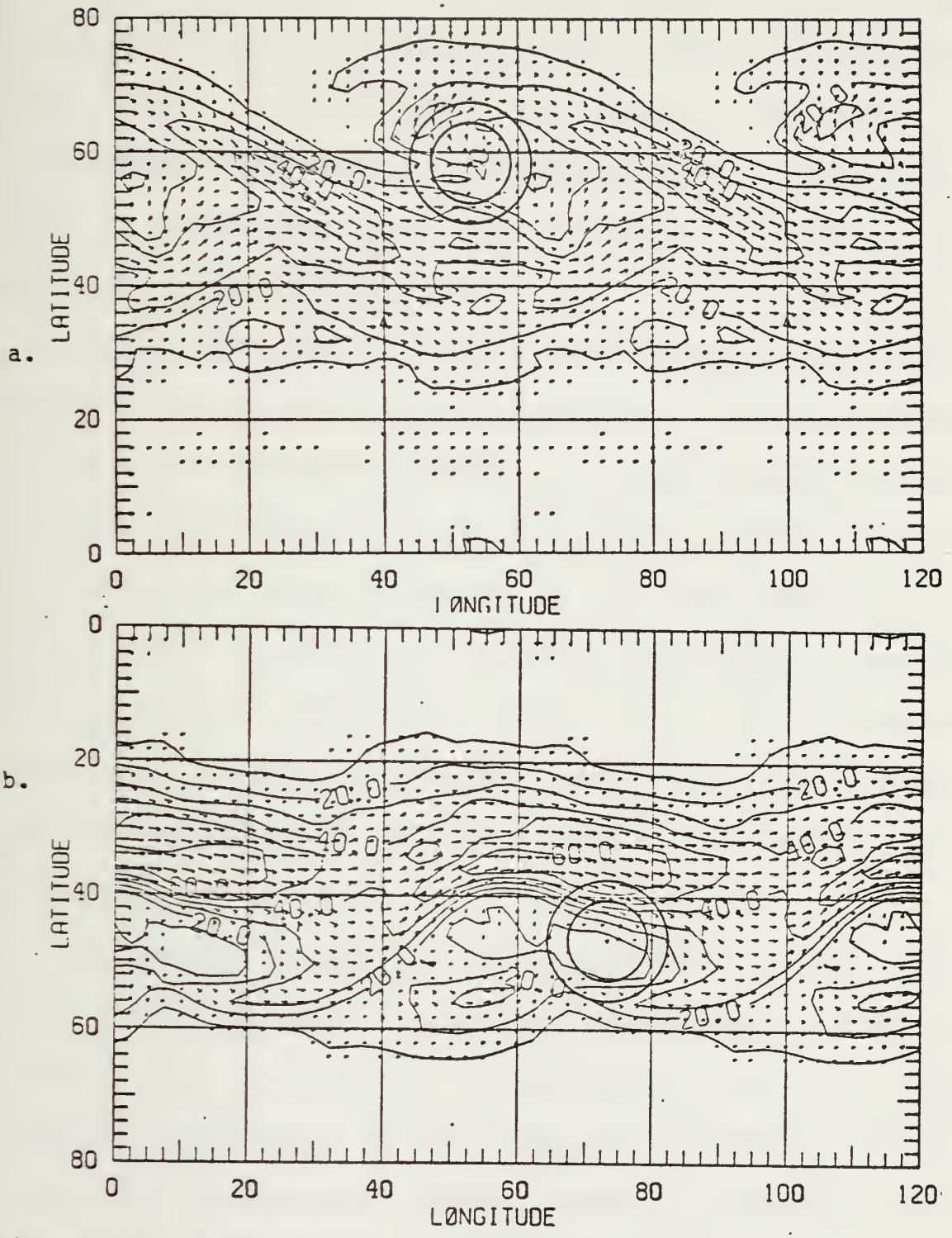

Figure 27. Same as Fig. 21 except for initial time + 168 hours.

aloft, and with no significant vorticity advection. The upper-level cold trough and the low-level cyclone develop simultaneously while maintaining their position relative to each other. In addition, the primary contribution to development is provided by lower-tropospheric thermal advection (at least during the early stages of development) and not upper-level vorticity advection.

During the early stages of cyclogenesis, the lower-tropospheric features are very realistic. Near the surface, the simulated cyclones resemble the classical cyclone model with the cold air on the west side of the cyclone and warm air on the east side. Cyclones N1 and S are nearly symmetrical for the first 24 to 48 hours of this study. However, the subsequent development results in a very elongated structure. Although asymmetrical cyclones are not uncommon, the extreme elongation of these cyclones does appear to be atypical.

The lower-tropospheric thermal patterns are also realistic during the first half of the period studied. The warm advection in the vicinity of the storm during the early stages of development and the warm air coincident with the storm center during the latter stages of simulation would

tend to support cyclogenesis. However, the elongated thickness patterns and the orientation of the thermal ridges in each hemisphere during the later stages are unusual.

The Nitta and Yamamoto (1974) observational study supports the findings of Petterssen, et al. (1962). In addition, they noted that oceanic cyclones generally predominate in the lower troposphere. The development of the two cyclones used in this study is generally limited to the lower troposphere although cyclone S developes weak closed lows at mid- and upper-tropospheric levels. These features, however, are extremely weak and do not appear until hour 168. It is not surprising that cyclone S developes to the upper troposphere, however the vertical coupling of this development is somewhat unusual. This feature will be discussed in more detail later in this section.

The above characteristics of the model storms which appear to be realistic are basically associated with the lower troposphere. On the other hand, the anomalous features are generally associated with the vertical configuration of the cyclones and the structure of the mid- and upper-tropospheric levels of the model, mid-layer 4 and mid-layer 3 respectively. The development of the short

waves in the middle and upper troposphere appears to be atypical. In particular, the orientation of these waves and the resulting shear are quite unusual. As noted earlier, troughs in each hemisphere eventually tilt back on themselves creating extreme directional shear.

The height and thermal fields at mid-layers 4 and 3 are nearly in phase throughout the 72 hours of this study. Furthermore, a close examination of the height fields at these two levels reveals them to be nearly identical in shape and vertically stacked throughout the entire period of this study. This is a reflection of a self-amplification process and is likely related to the lack of occlusion and shallow structure of the mature cyclones. In addition, the upper troughs and the cyclones maintain their positions relative to each other throughout the period of this study. These two features are consistent with the observations of Petterssen, et al. (1962); however, the distance between cyclone S and the weak upper lows which develop in the SH after 168 hours of simulation is unusual. The closed upper lows are vertically aligned but they are nearly 700 nm to the northwest of the surface center. By the time the upper lows develop, cyclone S has reached its peak intensity (975

mb between hours 141 and 147) at the surface and has begun to weaken somewhat (to 981 mb). One might expect the upper-level lows to be more intense and vertically aligned with the surface low during the mature stage of the cyclone.

The development of the patterns in the mid-layer 4 vorticity fields also appears to be anomalous. In particular, the location of the vorticity maxima with respect to the cyclones (over cyclone N1 and equatorward of cyclone S) during the final 48 hours of this study is unusual. The extremely elongated regions of relatively uniform vorticity which parallel the wind flow also appear to be unusual.

In conclusion, these model storms are characterized by both realistic and unusual features. The realistic features are generally in the lower troposphere with the atypical features generally in the middle and upper troposphere. The vertical resolution of the model's upper troposphere could possibly be a factor in the development of these unusual features. Although all aspects of these storms are not typical of oceanic cyclones, they are realistic enough to be useful in determining the mass and circulation budgets of numerically simulated cyclones. Quasi-Lagrangian diagnostic

techniques are described in the next chapter. An analysis of the mass budgets of these storms is presented in Chapter V.

IV. QUASI-LAGRANGIAN DIAGNOSTIC TECHNIQUE

A. QUASI-LAGRANGIAN DIAGNOSTICS

A primary goal of this thesis is to describe cyclone development quantitatively through an analysis of mass budgets. The quasi-Lagrangian diagnostics approach provides a means of achieving this goal. Wash (1978) demonstrated the validity of the quasi-Lagrangian diagnostics approach in budget studies of observed and numerically-predicted cyclones. Basic quasi-Lagrangian diagnostics techniques are presented in this section with the mass budget equation presented in the following section. A description of the generalized quasi-Lagrangian diagnostics budget equation and the budget volume coordinate system (Wash, 1978) are presented in Appendix B.

Traditionally, budget studies have employed a stationary budget volume which is positioned so that the feature being studied moved through or remained within the budget volume during the period of the study (e.g. Smith (1973), Kung and Baker (1975), and others). Since the horizontal extent of a stationary budget volume is greater than that of a cyclone

scale feature, it is not possible to isolate a cyclone from the environment in which it is moving. In addition, budget studies employing stationary budget volumes provide a qualitative estimate of the large scale forcing processes involved in cyclone development and decay. Therefore, the use of a stationary budget volume is not particularly suited to budget studies of cyclones.

The quasi-Lagrangian technique is ideal for budget studies of cyclones because the budget volume moves with the velocity and direction of the cyclone. A translating budget volume affords a method of distinguishing between the effects of storm translation and actual cyclone development. Thus a translating budget volume is, in fact, an instrument for examining the fluxes across the budget volume boundaries by eliminating the distortion that results from the movement of the storm.

Budget studies which employ a storm-following budget volume provide a view of the interaction between the smaller scale cyclone and the planetary scale environment in which it is embedded. Through the transport relation and other governing equations, the quasi-Lagrangian budget approach provides a method of calculating the underlying scale

interaction processes. This approach emphasizes the transports of mass through the boundaries and the changes in the circulation within the budget volume. Quasi-Lagrangian diagnostics incorporates transports into and out of the budget volume, as well as internal sources and sinks of these basic properties.

The quasi-Lagrangian diagnostics approach has been used in a variety of cyclone studies. Table II, partially extracted from Wash (1978), is an updated list of several recent budget studies which applied quasi-Lagrangian diagnostics to observed and/or simulated cyclones.

TABLE III

QUASI-LAGRANGIAN DIAGNOSTICS BUDGET STUDIES
(partially extracted from Wash, 1978)

PROPERTY	RESEARCHER(S)
Available Potential Energy	Spaete 1974
Circulation	Wash 1975
Mass	Johnson and Downey 1976
Absolute Angular Momentum	Johnson and Downey 1976
Kinetic Energy	Chen and Bosart 1977
Absolute Angular Momentum	Wash 1978
Mass	Roman 1981
Circulation/ Angular Momentum	Conant 1982

As mentioned earlier, quasi-Lagrangian transport theory provides a diagnostic framework which is ideally suited to the study of cyclone-scale circulations. In addition, the internally consistent "data" base of numerically simulated cyclones limits computational errors to those resulting from interpolation from a rectangular grid to the circular grid of the budget volume and to round-off errors. With the quasi-Lagrangian diagnostics approach, a cylindrical budget volume is placed around the model storm and is moved with the storm center. For this study, the surface pressure minimum is used to indicate the storm center. The budget volume extends from the earth's surface to the top of the atmosphere with the axis of the budget volume normal to the earth's surface. The budget volume is actually a portion of a cone with its vertex at the earth's center. However, since the tropospheric height is much less than the radius of the earth, the budget volume radius is assumed to be constant in the vertical. The budget volume for this study consists of the seven model sigma levels as defined in Chapter II. The radius of the budget volume is defined in degrees latitude relative to the storm center. Having defined the location and radius of the budget volume,

the budget of any basic storm properties (e.g. mass, circulation, angular momentum, kinetic energy, and moisture) can be studied.

B. BUDGET EQUATIONS

For this study the quasi-Lagrangian diagnostics technique is applied to mass budgets of two numerically simulated cyclones. The model experiments defined vertical motion to be zero at the upper and lower boundaries of the atmosphere. Thus vertical transports across these boundaries are eliminated in the mass budget equations.

Table IV contains the mass budget equation in the sigma coordinates of the model. In its most basic form, the generalized budget equation consists of three terms: lateral transport, vertical transport, and source (or sink).

Since there are no sources or sinks of mass, the source (sink) term of the generalized equation is zero. The remaining terms in the mass budget equation represent the lateral mass transport (convergence/divergence) and vertical transport (residual) respectively. When the limits of integration are $\sigma = 0$ and $\sigma = 1$ (where $\dot{\sigma} = 0$), the budget residual term must be zero. If not, the lateral mass transport term for the various model layers are adjusted so that the

integrated residual vanishes. Lateral mass transport and mass tendency are computed within the mass budget and residual imbalances are then computed from the time averages of these quantities. Vertical integration of the layer residuals produces a vertical mass transport which is then expressed as a vertical velocity field.

TABLE IV

QUASI-LAGRANGIAN MASS BUDGET EQUATION IN SIGMA COORDINATES

(after Wash, 1978)

(See Appensix B for budget notation and generalized budget equation.)

For the mass budget $f = 1$ and $\frac{df}{dt} = 0$.

Substitution of these values into the generalized budget equation results in the following mass budget equation:

$$\frac{dM}{dt} = \int_{\sigma_B}^{\sigma_T} \int_{0}^{2\pi} \frac{p_*}{g} (U-W)_\beta \, r \sin\beta d\alpha(-d\sigma) \Big|_{\beta_B}$$

$$+ \int_{\sigma_B}^{\sigma_T} \int_{0}^{\beta_B} \int_{0}^{2\pi} \frac{p_*}{g} \frac{\partial \dot{\sigma}}{\partial \sigma} r^2 \sin\beta d\alpha d\beta(-d\sigma).$$

V. BUDGET ANALYSIS

A. INTRODUCTION

The analysis of the quasi-Lagrangian mass budget begins with a presentation of the thermal structure of the cyclones in terms of potential temperature (Section B). This is followed by a discussion of the pressure (mass) tendency (Section C) and the total lateral mass transport (Section D). Vertical mass transports are discussed relative to the model vertical velocities (Section E). In an effort to determine the accuracy of the vertical velocities computed in the mass budget, budget vertical velocities are compared to the model vertical velocities (Section F).

Most figures presented in this chapter are layer/time period cross-sections. Budget calculation values at levels and "data" times were averaged to produce layer and time period midpoint values respectively for the time sections. Exceptions are indicated where appropriate. Inward and upward transports are represented by positive values in all these figures.

B. THERMAL STRUCTURE

Area-averaged mid-layer and "data" time potential temperatures are presented in Figs. 28 and 29. The vertical structures are similar in the two cyclones. The patterns for radii six and nine are nearly identical. In the upper troposphere, the potential temperature increases slightly, while decreases are seen in the middle and lower troposphere during the last half of the study. During the period of most intense cyclogenesis (hours 96 to 125) only small fluctuations are seen in the area-averaged potential temperature. The cooling, which occurs during a quasi-steady state period for each cyclone, is more pronounced in cyclone N1. This cooling within each budget volume is a consequence of the development and poleward movement of the cyclones. In addition, although the troposphere of cyclone N1 cools more than cyclone S, its average potential temperature is only slightly lower at the final "data" time, since cyclone N1 was initially warmer in the low troposphere. These potential temperature cross-sections show that cyclone N1 initially had weaker vertical stability than cyclone S. However, by the end of the study, the two cyclones have similar vertical stability characteristics.

The cooling in cyclone N1 gives the appearance of a cold core structure. This however is not the case since the center of each cyclone is actually located in the warmest air within each budget volume (see Fig. 11). The cooling is likely a result of cold advection into the equatorward half of each budget volume. The low-tropospheric thermal pattern can be seen in the 1000 mb to mid-layer 4 thickness pattern for hour 168 (see Fig. 11). The thickness pattern shows a warm tongue extending from the east through the center of cyclone N1, while a similar warm tongue extends east to west through the radius nine budget volume of cyclone S. The thickness pattern also reveals that the cold air occupies more of the budget volume of cyclone N1 than cyclone S, thus resulting in the slightly lower average temeperatures for cyclone N1.

Although the model atmosphere has no specified tropopause, Figs. 28 and 29 clearly show the existence of a strong tropopause and a stratosphere during the 72 hours of this simulation study. Level 2 (approximately 200 mb) effectively functions similar to a tropopause layer with slight warming and strong vertical stability above 200 mb. The potential temperature evolutions are characterized by

slight fluctuations below level 2. These fluctuations provide a hint of a cyclic evolution pattern during the development of these storms, although the period of the cycle is not evident.

C. MASS TENDENCY

There are no sources or sinks of mass within the atmosphere, however it is possible for a limited volume of atmosphere to gain or lose mass. The time rate of change of mass within a storm-following budget volume provides a quantitative measure of cyclogenesis. Within the mass budget, the total mass within each specified budget volume is computed for each "data" time. From these values, the mass tendency between "data" times is determined, and subsequently converted to a pressure tendency.

The mass tendency at 3-hour intervals for both cyclones is presented in Fig. 30. A cyclic pattern is clearly indicated. These time profiles also indicate that the development of the model cyclones occurs in two phases--an initial explosive cyclogenesis period (hours 96 to 126) and a quasi-steady state period (hours 126 to 168). A 12-hour oscillation is clearly evident throughout these two phases. During the explosive cyclogenesis phase, the cycle in the

a.

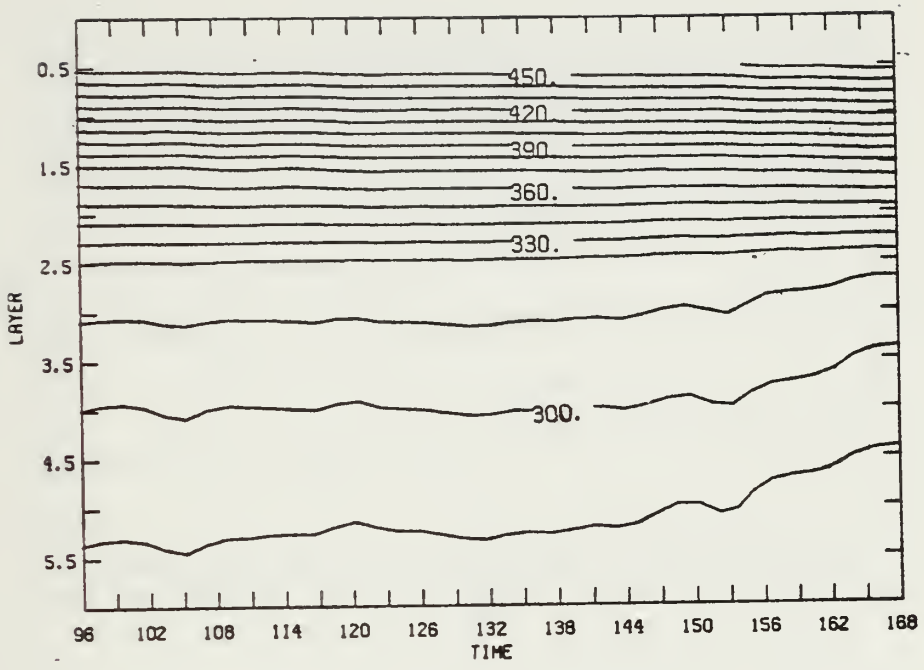

b.

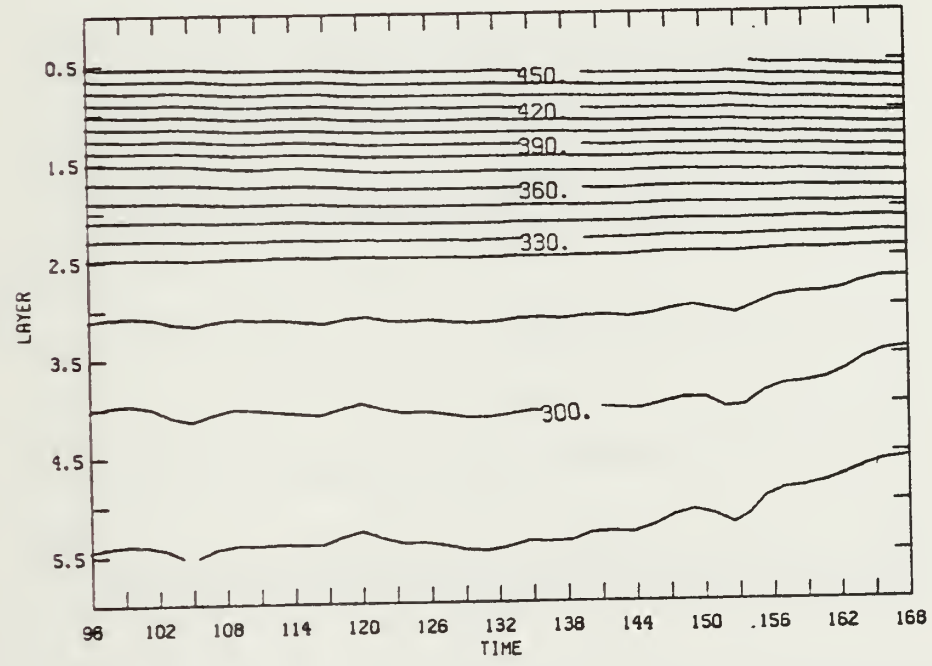

Figure 28. Cyclone N1 area-averaged potential temperature time section. (°K) a. radius nine. b. radius six.

a.

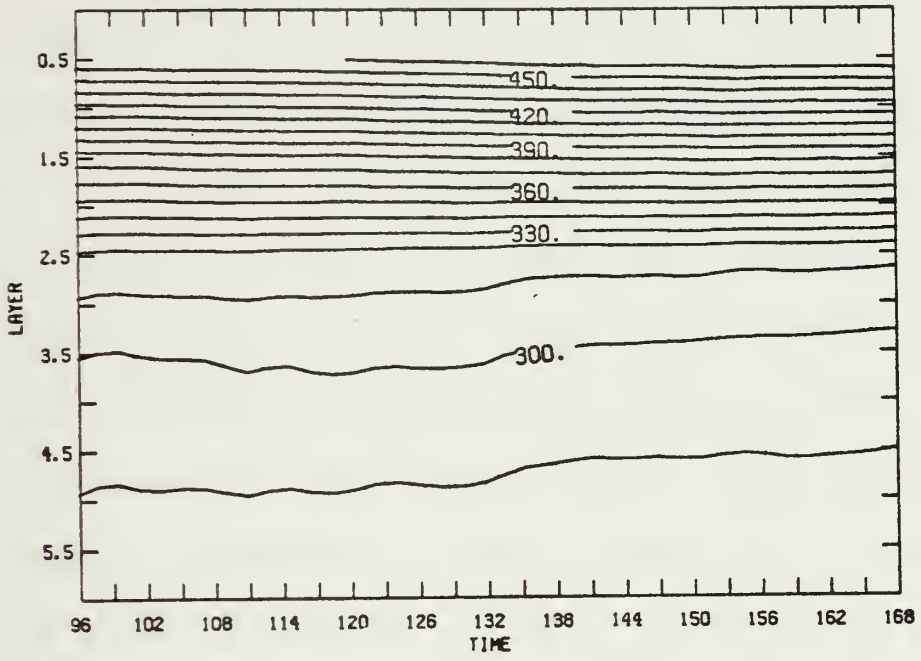

b.

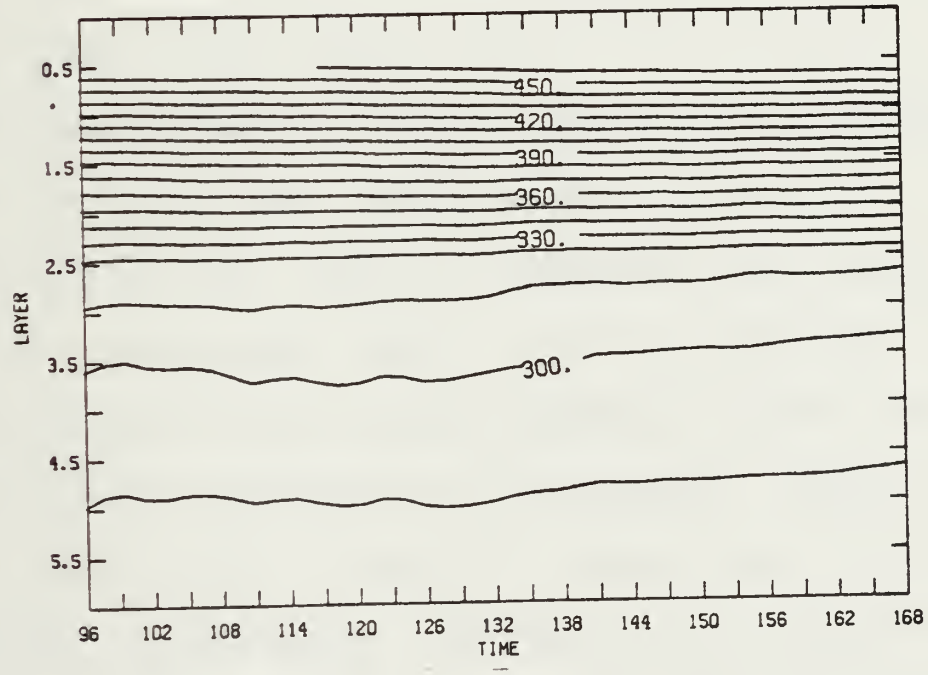

Figure 29. Cyclone S area-averaged potential temperature time section. (°K) a. and b. as in Fig. 28.

radius six budget consists of a maximum 3-hour pressure fall followed by a 9-hour period of relatively smaller surface pressure change. The cyclic pattern during the quasi-steady state phase is characterized by alternating periods of deepening and filling. The 12-hour cycle can be seen in the pressure tendency patterns for both the inner and outer radii. The pressure tendency trace for each budget volume shows that thecyclone's area-averaged surface pressure drops in discrete intervals like a step function rather than showing continuous deepening. These oscillations could be removed by using an highpass filter. Filtering would also serve to emphasize the deepening during the first 24 hours and the filling which occurs later.

The pressure tendency oscillations are not as pronounced in the graphs of the central surface pressures of these cyclones (Fig. 31). This is especially true during the explosive cyclogenesis phase, when a generally steady decrease is seen in the surface pressure. However, the rate of change nearly corresponds to the pressure tendency fluctuations in Fig. 30. During the second phase of cyclone development, oscillations are seen in the central surface pressure, however they are not as large as those the pressure tendency.

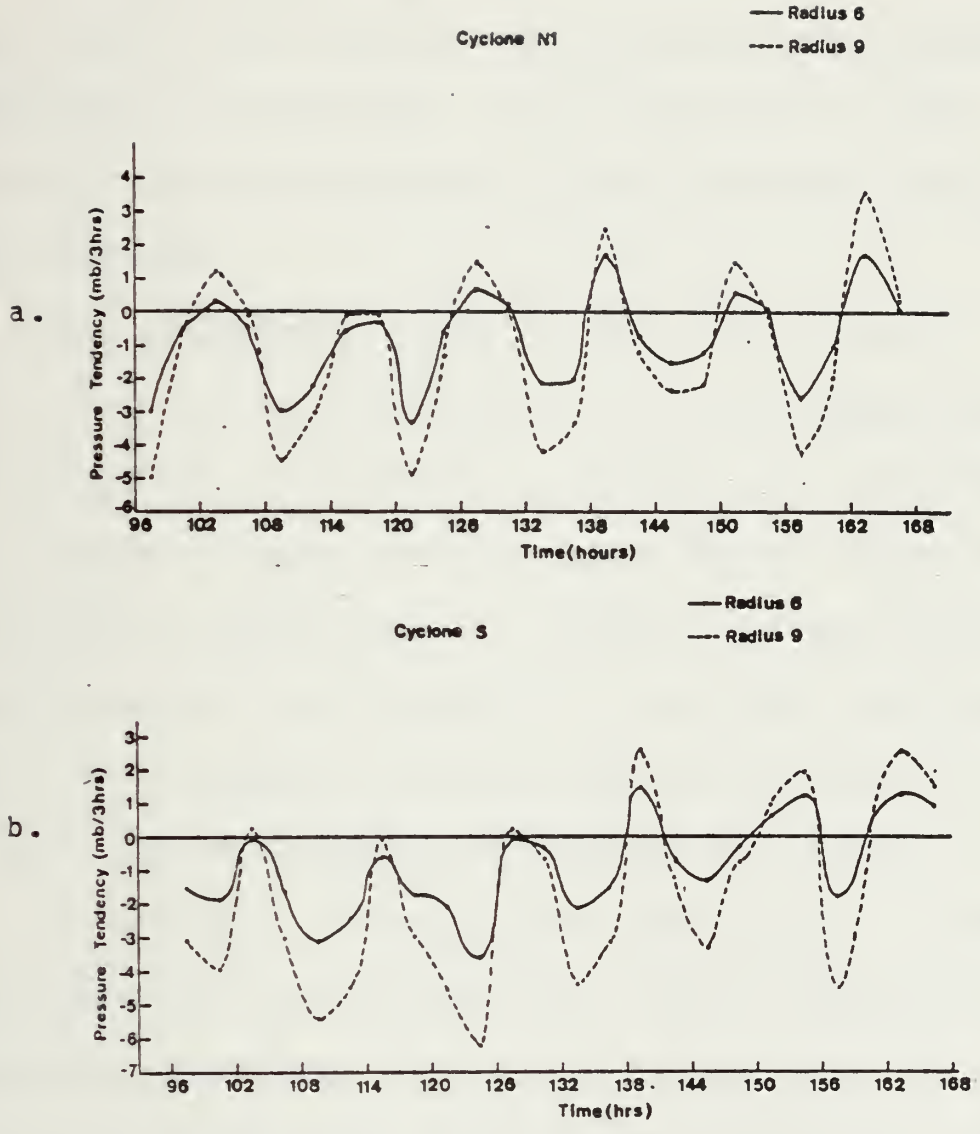

Figure 30. Area-averaged pressure tendency for cyclones N1 and S. (mb/3 hours) a. Cyclone N1. b. Cyclone S.

The cause of these mass fluctuations is not known. One possibility is that the cycle is the reflection of an external gravity wave propagating within the model. An external wave would have a similar effect on the surface pressures of neighboring anticyclones. For this reason a study of the central surface pressures of model-generated anticyclones was completed.

This preliminary study of five highs (three in the NH and two in the SH) for periods of 48 to 72 hours (the length of the period was dependent on whether the anticyclone was an analyzed feature at a particular "data" time) strongly indicates a cyclic pattern of surface pressure fluctuations (approximately two millibars) in the model anticyclones as well. The pressure oscillations of the cyclones and anticyclones suggest a propagating external wave within the model.

The pressure tendency traces show larger fluctuations for radius nine than radius six. This indicates that the pressure falls/rises for the area between radii six and nine are larger than those for the area within the radius six budget circle. An examination of other budget radii showed that the magnitude of the pressure tendency fluctuations increases for larger radii. This also suggests a

large-scale (perhaps hemispheric or global) sloshing. Because the scale of this feature is much larger, and it does not interact with the synoptic-scale features, the slosh is independent of cyclone development. A more detailed investigation of the model surface pressure field is required to isolate this phenomena and determine if it adversely affects the numerical simulations.

D. LATERAL MASS TRANSPORT

One goal of this thesis is to isolate the lateral and vertical branches of the mass circulation of the model cyclones. The lateral mass transport which is the mass flux through a specified budget volume boundary. The lateral mass transport time sections (Figs. 32 and 33) graphically describe a classical cyclone structure of low-level convergence (surface to approximately level 4: surface to 600 mb) and upper-level divergence (approximately level 4 to mid-layer 2: 600 to 150 mb). A similar pattern is noted at radius nine, however the level of nondivergence (LND) is slightly higher (approximately mid-layer 4: 500 mb). The lateral mass transport time sections indicate that the mass circulation does not extend into the top two model layers. This further substantiates the existance of tropopause and stratosphere behavior within the model.

The maximum inflow at the inner and outer radii of each cyclone occurs in the lowest model layer (centered at approximately 900 mb), while the maximum outflow is centered near mid-layer 3 (approximately 300 mb) at the tropopause. In addition, the mass circulation at radius nine of each cyclone is more intense during the quasi-steady state phase than during the rapid cyclogenesis phase. This is a further indication that the the second phase of development is actually an outward growth period more than a deepening period for these cyclones.

A cyclic pattern is evident at the levels of maximum inflow and outflow at both the inner and outer radii of each cyclone. Looking first at cyclone N1 (Fig. 32), the maximum outflow at radius six occcurs at hour 117 with secondary maxima centered at hours 140, 150, and 168 while nearly equal inflow maxima are seen at approximately these times. The maxima at hour 117 occur during the period of intense surface development (as indicated by changes in the central surface pressure, Fig. 31), while the maxima at later times occur during the quasi-steady state phase of cyclone N1. The lateral mass transports at radius nine of cyclone N1 are also characterized by oscillations in the basic

inflow-outflow pattern. The cyclic variation in the lateral mass transport are coupled with the oscillations in the pressure field.

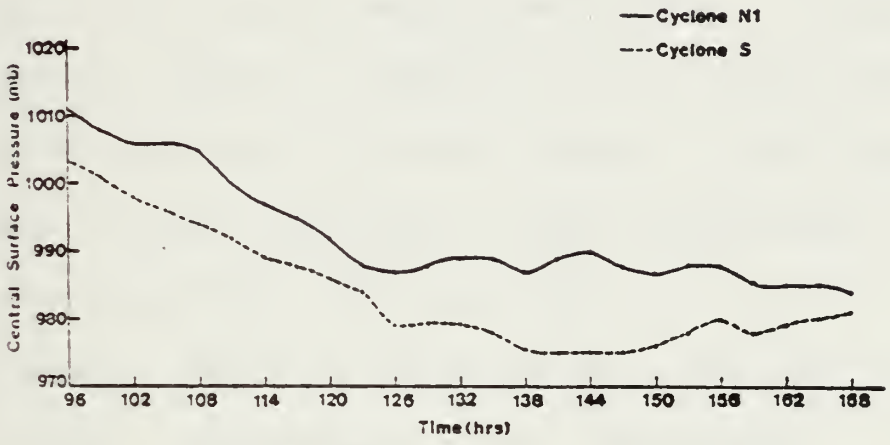

Figure 31. Central surface pressures (mb) of cyclones N1 and S.

A dramatic increase at 6° and a decrease at 9° in the height of the level of LND is also seen during the quasi-steady state phase of cyclone N1. The LND height change for radius nine (approximately hour 135) is related to the intensification of the mass circulation during the second stage of development and the growth of the cyclone to the 9° budget volume boundary.

The lateral transport time sections for cyclone S also exhibit the classical mass circulation pattern. However,

the cyclone S lateral transport pattern is noticeably different from that of cyclone N1. Specifically, the cyclone S lateral mass transports at radius six are more intense than those of cyclone N1. This is a reflection of the greater intensity of the spring hemisphere cyclone. In addition, the height of the LND at radius six of cyclone S gradually lowers from about 500 mb to near 700 mb, and is generally lower than its NH counterpart (which remains near 600 mb throughout this study) after hour 132.

The radius nine time sections for these two cyclones also display similarities and differences. As in cyclone N1, there is a simultaneous decrease in the height of the LND and the intensification of the lateral mass transports. However, this occurs earlier in cyclone S (hour 120 for cyclone S and hour 135 for cyclone N1), and the decrease in the LND height is more dramatic (from 500 mb to 700 mb for cyclone S and about 475 mb to 600 mb for cyclone N1). The sharp decrease in the height of the radius nine LND in cyclone S occurs simultaneously with the outward growth of the cyclone to the outer budget volume boundary. As with radius six, the radius nine lateral transports are more intense in cyclone S.

Of special note is the abrupt weakening of the cyclone S mass circulation during the final 21 hours of this study. This weakening is most noticeable and occurs earlier at radius six. The decrease in the mass transport intensity can be seen in both the inflow and outflow branches, however it is more pronounced in the outflow branch. This weakening of the lateral mass transports is indicative of the decay of cyclone S and is reflected in a corresponding increase in the central surface pressure of cyclone S. In contrast, the lateral mass transports at the cyclone N1 budget radii continues to be strong at the last "data" time when cyclone N1 reaches its lowest central surface pressure (984 mb).

E. VERTICAL MASS TRANSPORT

The vertical branch is an integral part of a cyclone's mass circulation. Since the vertical mass transports are the area-averaged vertical velocity structures within the cyclone (in both isobaric and sigma coordinates), time sections of the model vertical velocities (Figs. 34 and 35) are used for the following discussion of the vertical transports. This discussion points out similarities and differences in the patterns of these two storms. In general, upward motion is seen below level 2 (approximately 200 mb)

at the inner and outer radii. Alternating periods of weak upward and downward motion are seen above level 2 in the model stratosphere. The upward motion is quite intense at radius six of each cyclone. The level of maximum upward vertical motion coincides with the LND indicated in the lateral mass transport time sections (Figs. 32 and 33). periods of maximum upward vertical motion coincied (as they must) with the periods of most intense lateral mass transport. transport. The upward vertical motion at radius nine is weaker than at radius six. However, the intense upward vertical motion occurs only within the troposphere.

Considering first the six degree budget volume, two distinct periods of maximum upward vertical motion are evident in each cyclone. For cyclone N1, the first period (hour 107 to 123) occurs during the explosive cyclogenesis phase, while the second period (after hour 147) occurs during the quasi-steady state phase. The subsequent radius six maximum occurs simultaneously with a similar maximum at radius nine, and results from the outward growth of the cyclone to the outer budget volume boundary.

Cyclone S also experiences two periods of intense upward vertical motion (centered at hours 117 and 138). As in

a.

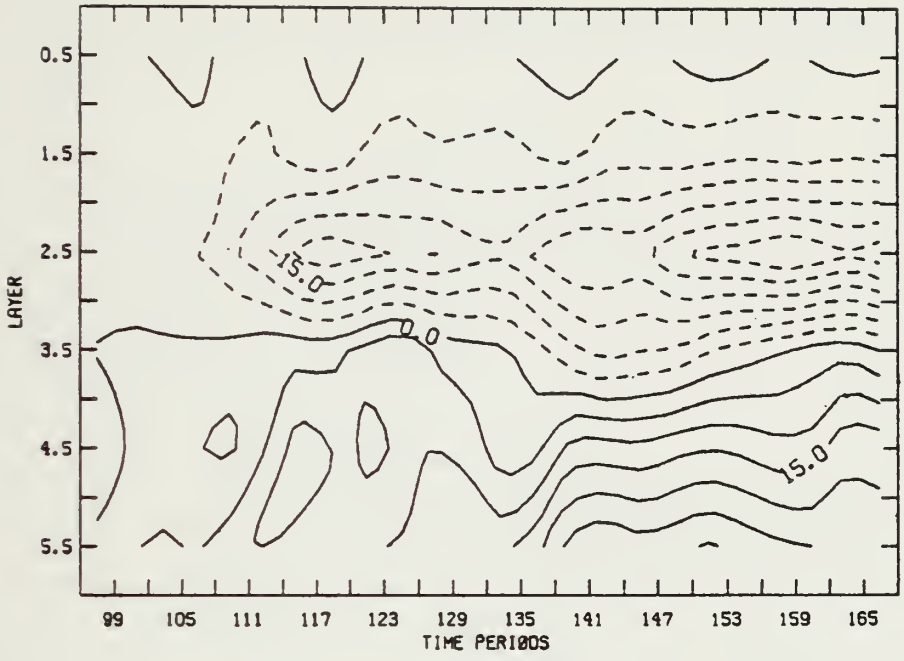

b.

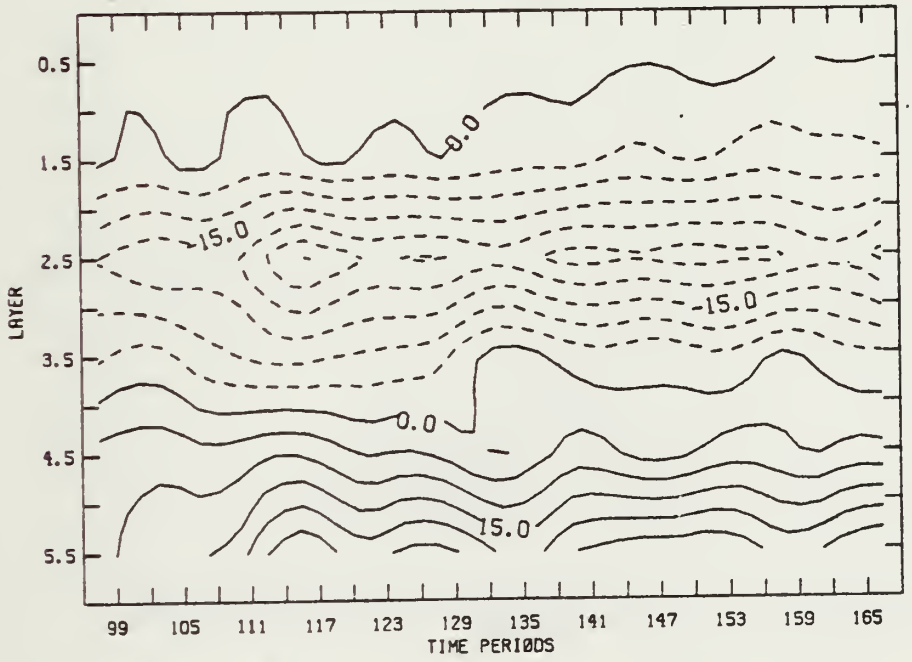

Figure 32. Cyclone N1 lateral mass transport time section. ($\times 10^{12}$ g sec^{-1}) a. and b. as in Fig. 28.

a.

b.

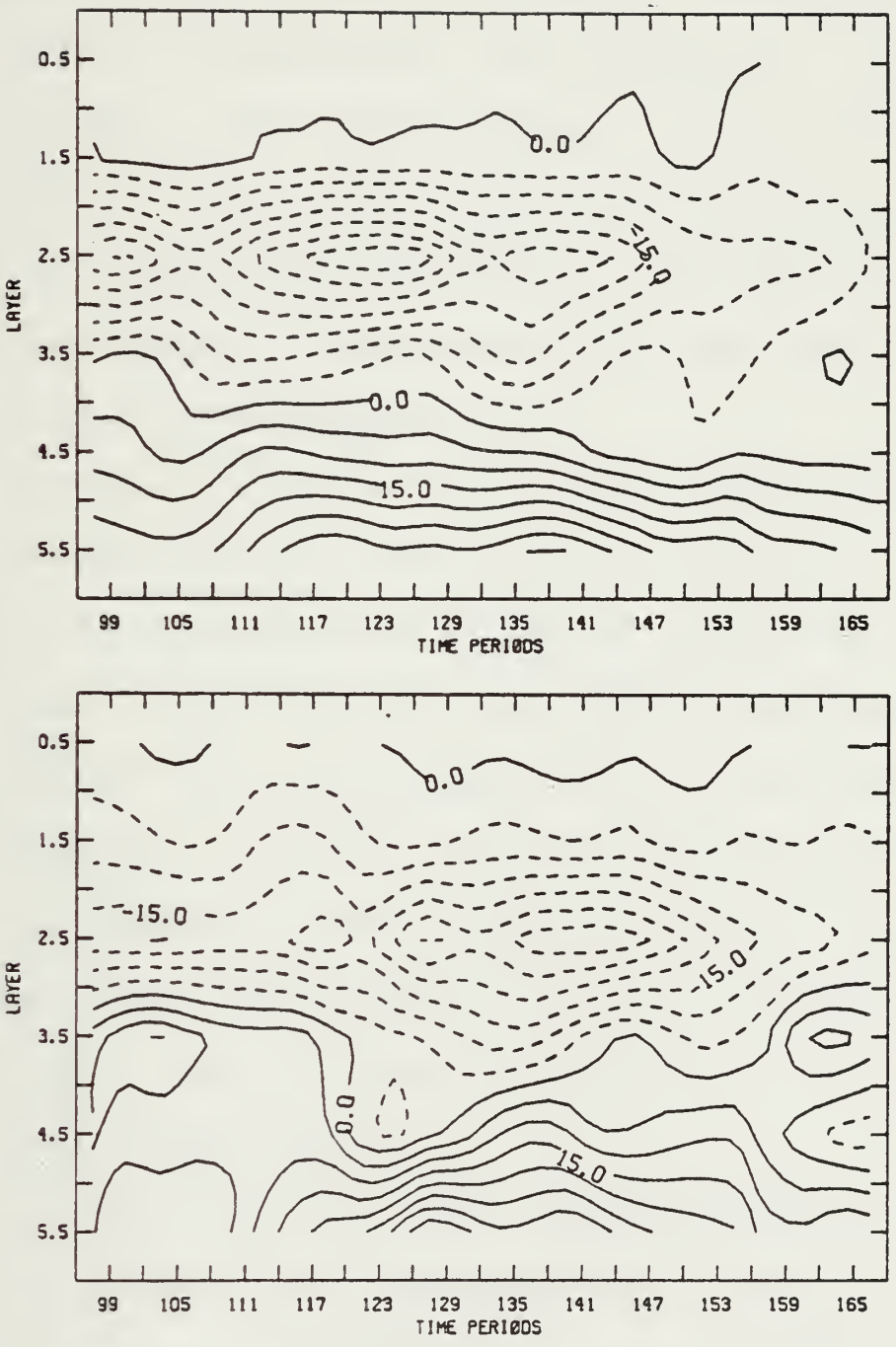

Figure 33. Cyclone S lateral mass transport time section. (X 10^{12} g sec^{-1}) a. and b. as in Fig. 28.

cyclone N1, the first maximum occurs during the explosive cyclogenesis phase while the second maximum and its radius nine counterpart occur during the period of outward lateral growth. Near the beginning of the integration, a third period of intense upward vertical motion is evident for each budget radius. However, its significance is unclear due to the lack of the preceeding model data. In addition, the decay of the cyclone is indicated by the rapid decrease in upward vertical motion after hour 159.

An interesting feature of the cyclone S radius nine time section is the downward vertical motion indicated in the lower two layers between hours 101 and 111. This requires a downward motion within the 6°-9° area which more than offsets the upward motion within radius six. This indicates strong subsidence around the cyclone compensating for the intense upward vertical motion associated with the explosive cyclogenesis phase when cyclone S is still within the 6° budget volume. This is a possible reflection of the cyclic evolution of the model cyclones.

Time traces of area-averaged vertical velocities for level 4 of cyclones N1 and S are presented in Fig. 36. The two major periods of strong upward vertical motion which

a.

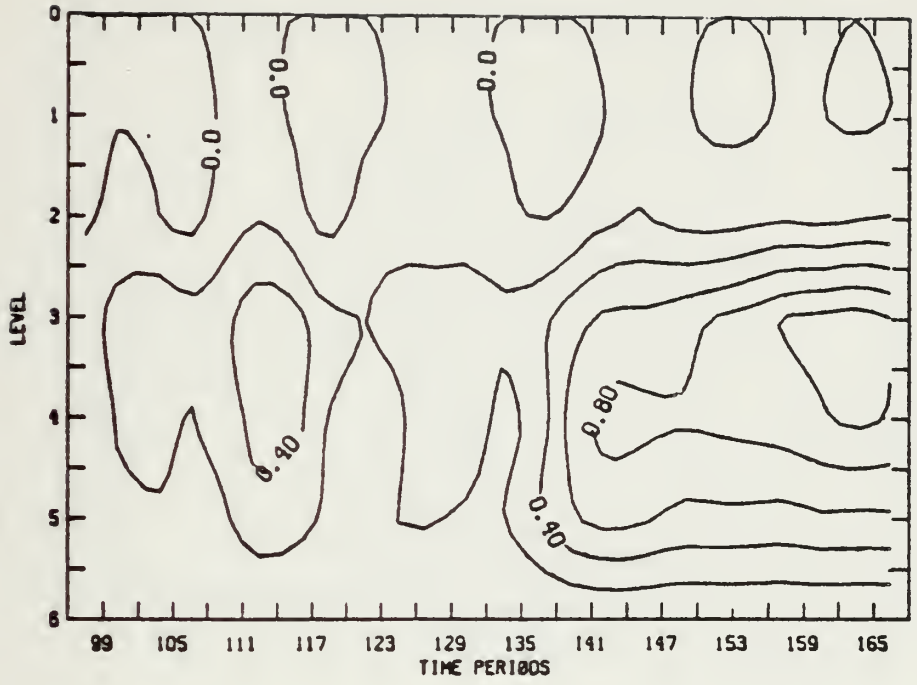

b.

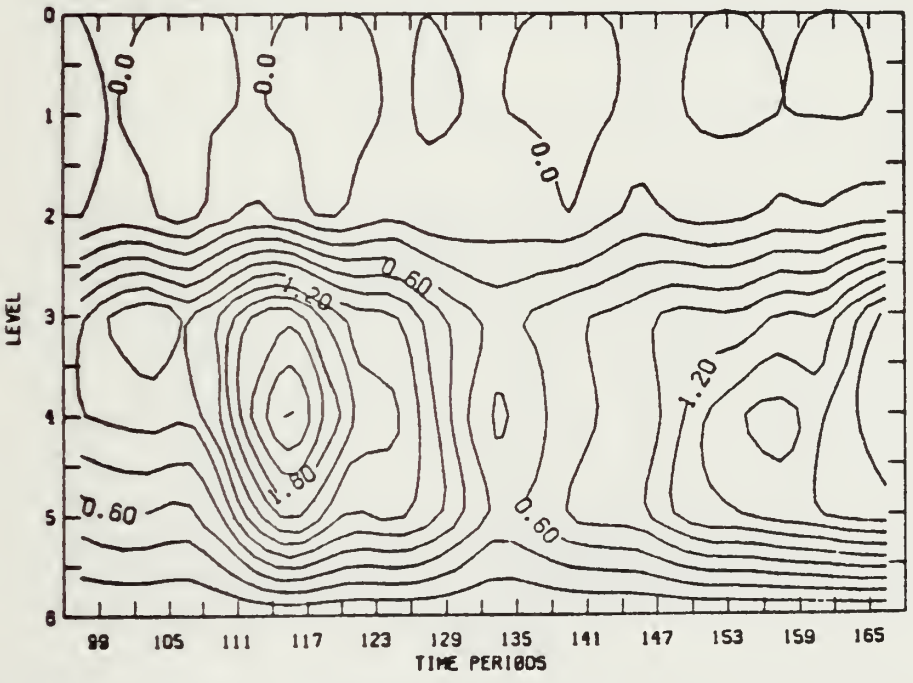

Figure 34. Cyclone N1 model vertical velocity time section. ($-\mu$ bar sec^{-1}) a. and b. as in Fig. 28.

a.

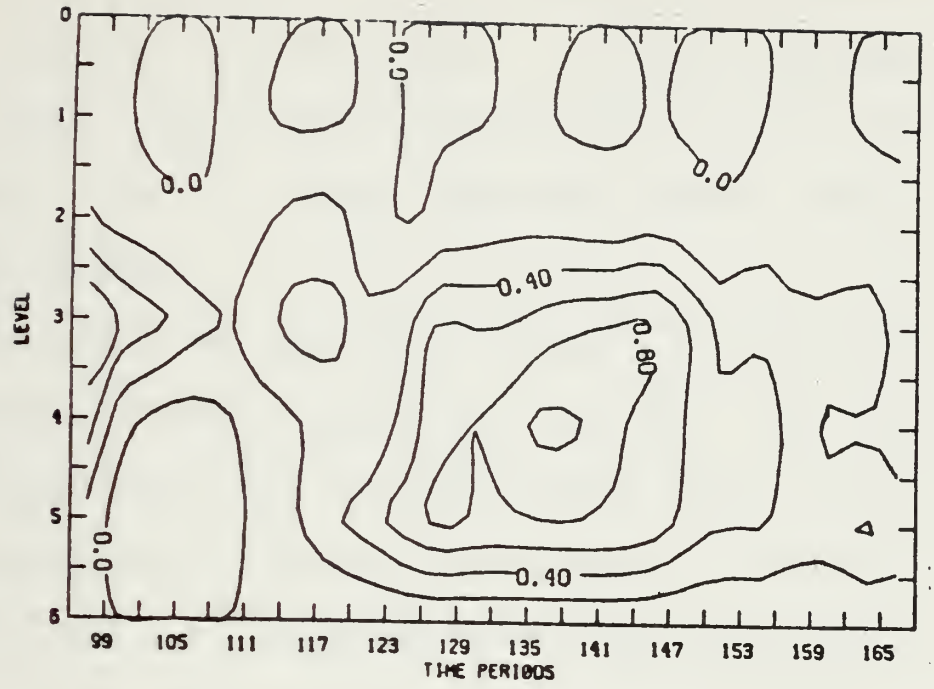

b.

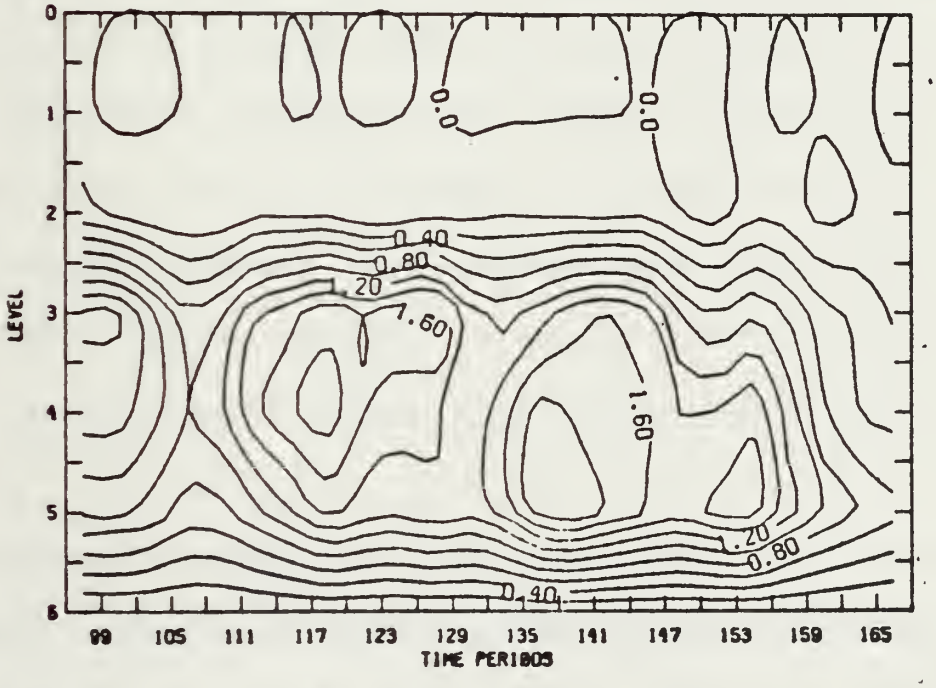

Figure 35. Cyclone S model vertical velocity time section. ($-\mu$ bar sec^{-1}) a. and b. as in Fig. 28.

correspond to the two-phase cyclone development are clearly depicted. The outward growth phase of each cyclone is vividly displayed in these traces. A dramatic increase in the radius nine area-averaged vertical velocities is seen as the lateral growth of these cyclones exceeds the 9° budget volume boundary.

The radius six trace for cyclone N is characterized by two distinct maxima at hours 115 and 168. The radius nine trace essentially has a single maximum which occurs during the second phase of cyclone development. The extreme maximum at hour 115 is approximately in the middle of the rapid cyclogenesis phase when the central surface pressure decreases 17 mb between hours 108 and 123 (see Fig. 31).

A surprising feature of the vertical velocities occurs between hours 141 and 150 when the magnitude within radius nine actually exceeds the corresponding value for radius six. This implies that the vertical velocities within the 6°-9° region exceed those within the radius six budget circle.

Although the cyclic pattern seen in cyclone S is similar to that of cyclone N, there are significant differences. As in cyclone N, two maxima are seen at radius six

(hours 118 and 136), however the time interval between these two occurrances is much shorter than in cyclone N. The first maximum occurs during the first phase of cyclone development when the central surface pressure decreases 22 mb between hours 99 and 126. The second maximum, which occurs during the quasi-steady state phase of cyclone S, coincides with the single maximum at radius nine. The maximum at radius nine of cyclone S is larger than its cyclone N counterpart. The decay of cyclone S is clearly indicated by the sharp decrease in the level 4 vertical velocities at both six and nine degrees.

F. COMPARISON OF MODEL AND BUDGET VERTICAL VELOCITIES

One objective of this thesis is a comparison of the model vertical velocities with those computed in the mass budget. The vertical divergence of the vertical mass transport (budget residual) and the mass tendency are computed within the mass budget (see Tables IV and V). A vertical integration of these values (from an upper boundary value of = 0 at = 0) describes the vertical mass transport, which is then converted to an area-averaged vertical velocity. Thus the budget vertical velocities are essentially kinematic omega values for the specified budget volume.

a.

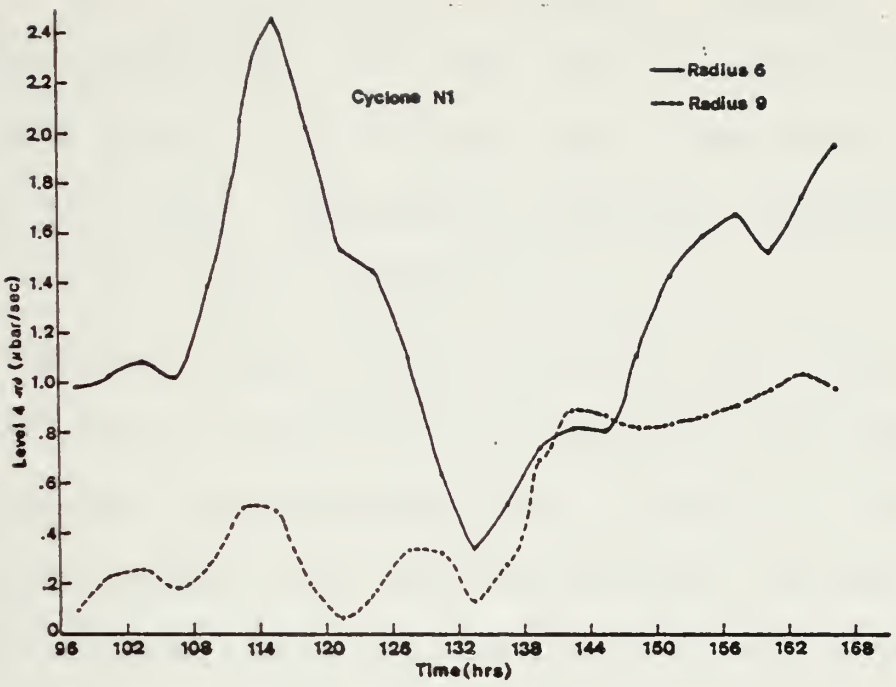

b.

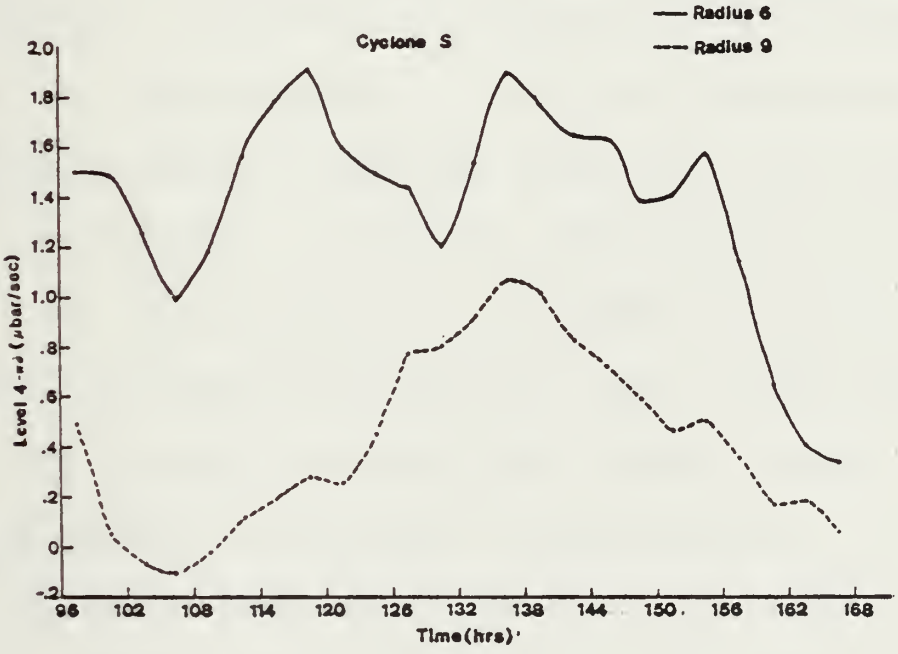

Figure 36. Model vertical velocity for level 4. ($-\mu$ bar sec^{-1}) a. and b. as in Fig. 30.

This approach has been used in atmospheric studies to infer vertical velocities and vertical transports of mass and other properties. In this study, vertical velocities are available as part of the model "data" base. This affords the unique opportunity to test the accuracy of the budget-derived vertical velocities.

The basic patterns in the model vertical velocity time sections (Figs. 34 and 35) are contained in the budget vertical velocity time sections (Figs. 37 and 38). The budget vertical velocities for radii six and nine of each cyclone are most intense below the tropopause (approximately mid-layer 3). Very weak vertical motion is seen in the model stratosphere. At radius six of each cyclone, two maxima are seen in the budget vertical velocities time sections, with the earlier maximum occurring during the first phase of cyclone development. As in the model vertical motion pattern, the second maximum in the budget vertical velocity time section occurs in conjunction with a radius nine maximum. This again indicates the lateral growth of the cyclones beyond the 9° budget volume boundary. For each budget radius of cyclone S there is a significant decrease in the budget vertical velocities after hour 159 when

cyclone S begins to fill. This feature is also seen in the model vertical velocities.

Although the patterns in the model and budget vertical velocity time sections are similar, significant differences were noted in the magnitudes of the budget vertical velocities. Timesections of the differences between these two values (budget value minus model value) are presented in Figs. 39 and 40. With the exception of the stratosphere, the budget vertical velocities were larger than those of the model. It appears that the largest departures occur where the vertical velocities (both model and budget) are largest.

Since the model has an internally consistent "data" base there are two possible sources for the errors in the budget-derived vertical velocities. Errors can result from the interpolation of the winds from the rectangular grid of the model to the circular grid of the mass budget. Other errors arise from the vertical distribution of the imbalances between the integrated divergence and the mass tendency, which must balance since there are no sources or sinks of mass. The comparison of the budget and model vertical velocities indicates that the lateral mass transports are too large after the interpolation and balancing proceedures

are completed within the mass budget. Given the consistent "data" of the model, these errors are generally larger than one might anticipate. A detailed examination of the interpolation scheme and the vertical distribution of the budget residuals should be conducted in an effort to isolate the source of these errors.

a.

b.

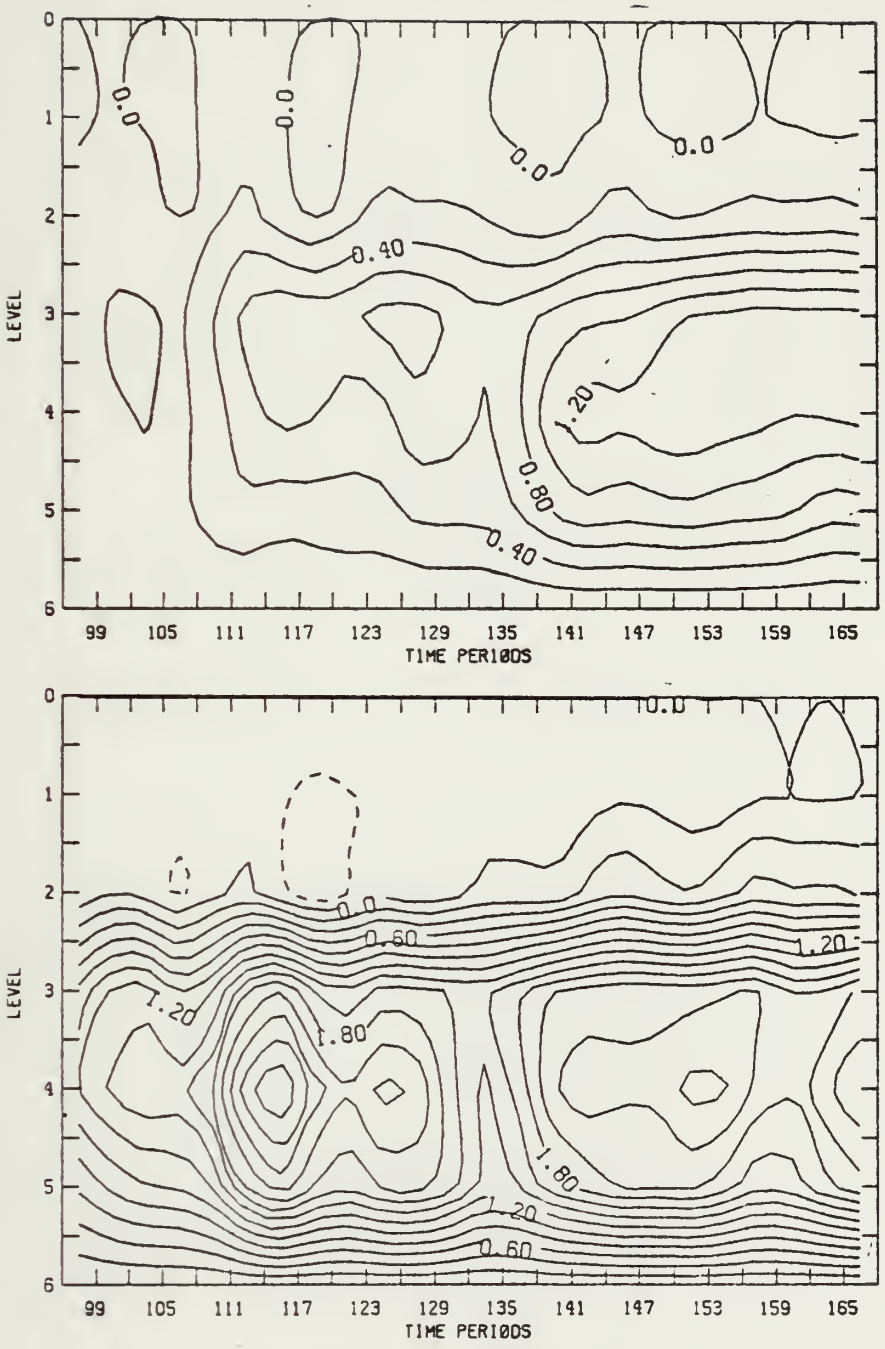

Figure 37. Mass budget vertical velocity time section for cyclone N1. ($-\mu$bar sec^{-1})
a. and b. as in Fig. 28.

a.

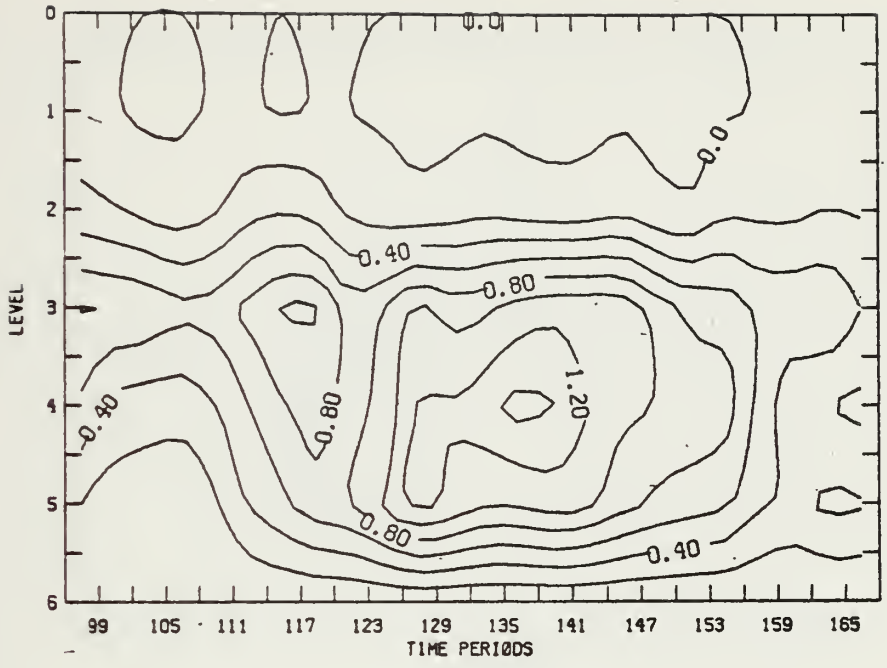

b.

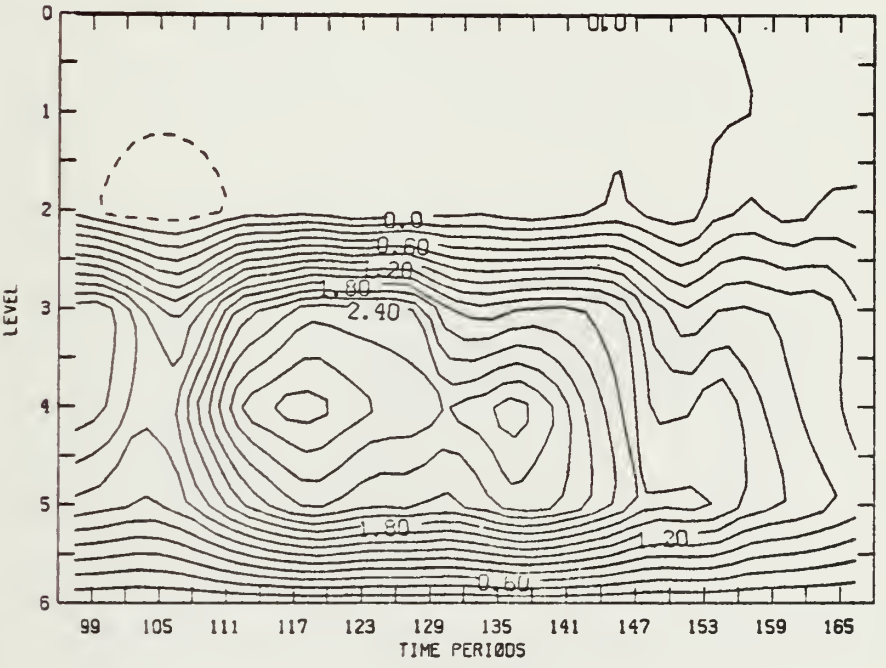

Figure 38. Mass budget vertical velocity time section for cyclone S. ($-\mu$ bar sec^{-1})
a. and b. as in Fig. 28.

a.

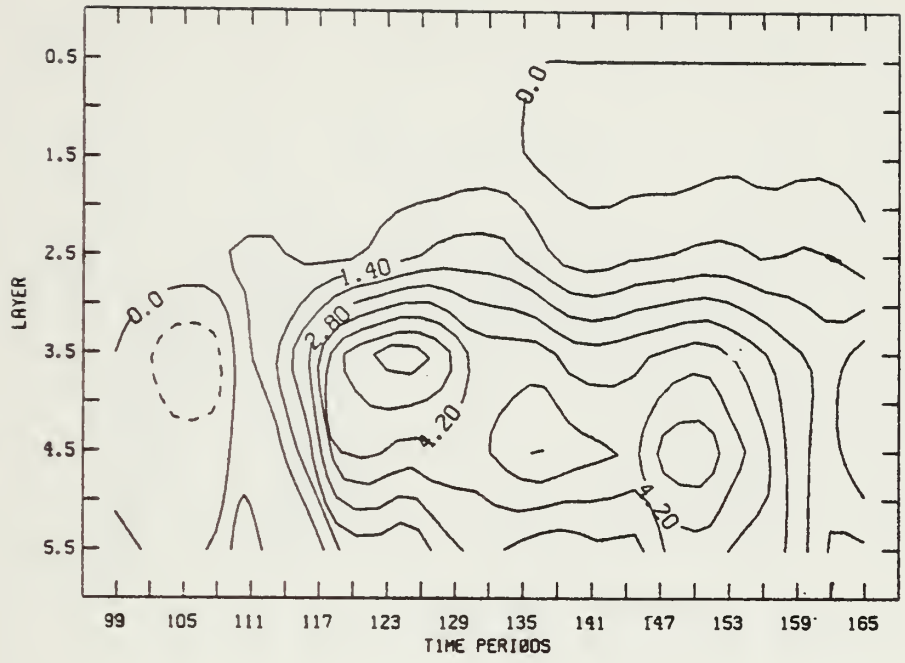

b.

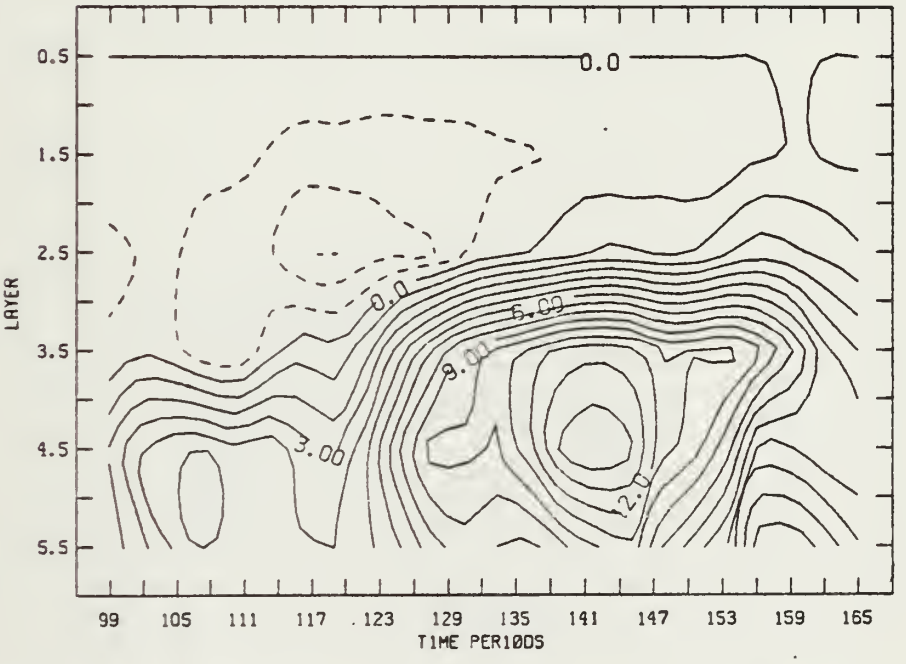

Figure 39. Budget vertical velocity error time section for cyclone N1. Model vertical velocities minus budget vertical velocities. ($-\mu$ bar sec^{-1}) a. and b. as in Fig. 28.

a.

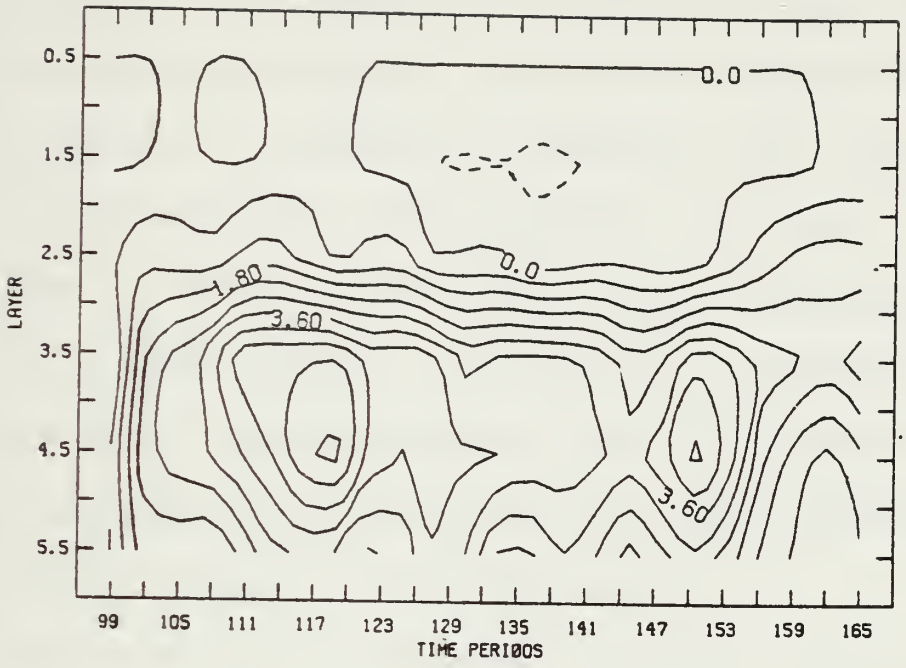

b.

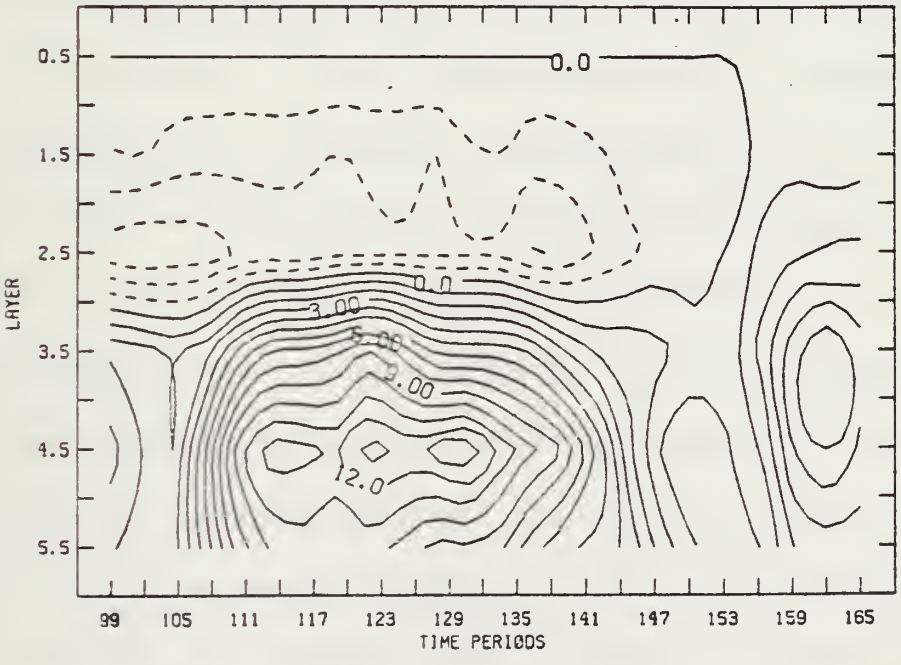

Figure 40. Budget vertical velocity error time section for cyclone S. Model vertical velocities minus budget vertical velocities. ($-\mu$ bar sec^{-1}) a. and b. as in Fig. 28.

VI. CONCLUSIONS

In this thesis two numerically simulated oceanic extratropical cyclones were studied. Initially a synoptic study of these cyclones, including a comparison with observed cyclones, was completed. These cyclones were found to be characterized by both realistic and unusual synoptic features. In a general sense, the realistic features were associated with the lower troposphere while the unusual features were associated with the middle and upper troposphere and the vertical coupling of the model layers.

These cyclones also were studied through the application of quasi-Lagrangian diagnostics. This diagnostic study of the mass circulation of model cyclones showed a concentration of inward lateral transport (convergence) in the lowest model layer and outward lateral transport (divergence) in a layer centered near 300 mb. Although the model has no specified tropopause, the basic patterns of the lateral and vertical mass transports and the thermal structure revealed the existence of a tropopause near mid-layer 3 of the model.

Traces of the mass tendency within 6° and 9° budget volumes revealed a 12-hour cyclic pattern imbedded in a

two-phase cyclogenesis pattern. The first phase of cyclone development was a period of explosive deepening while the second phase was a quasi-steady state period. The 12-hour cycle was most easily seen in the pressure tendency trace. During the first phase of cyclone development, the cycle consisted of a maximum 3-hour pressure fall followed by a 9-hour period of little surface pressure change. During the second phase, the cycle was characterized by alternating pericds of pressure falls and rises. It was also noted that the fluctuations in the pressure tendency increased for successively larger budget radii. The two-phase cyclone development was seen in the traces of the central surface pressures. However, the 12-hour cyclic pattern was not easily detected in these traces. This 12-hour cycle produces a step function decrease in the area-averaged surface pressure of these cyclones rather than a steady deepening. This step function evolution is not clearly indicated by the central surface pressure traces (see Fig. 31). A possible cause of this cycle is an external wave propagating within the model. However, further studies are needed to isolate the source of these oscillations.

The lateral mass transport and the vertical mass transport (converted to a vertical velocity) clearly described the mass circulation of these cyclones. Time sections of these terms also indicated two-phase cyclone develpment. Two maxima were seen at radius six of each cyclone--one during each phase of development. The one maximum seen at radius nine occurred in conjunction with the second maximum at radius six and indicated the outward growth of the cyclones beyond the outer budget volume boundary. Maxima in the lateral mass transport and vertical velocity time sections generally occurred simultaneously. In addition, the onset of the decay of cyclone S was indicated by the rapid decrease in the intensity of the lateral mass tendency and vertical motion near the end of the study.

Area-averaged vertical velocities were computed within the mass budget and were compared to area-averaged model vertical velocities. Although the time sections of these terms have similar basic patterns, significant differences were found in their magnitudes. It appeared that the departures were largest where the vertical velocity (both model and budget) were the largest. The two possible sources of these errors are interpolation of the wind from the model

grid to the budget volume grid, and imbalances in the vertical distribution of the mass budget residuals. Further studies are required to isolate the relative magnitudes of these two errors.

VII. RECOMMENDATIONS FOR FURTHER STUDIES

The results of the synoptic study and the mass budget analysis suggest that further diagnostic studies of the basic properties of these cyclones are needed to fully understand their dynamic structure. In addition, further studies are needed to determine the source of the errors in the budget derived vertical velocities. With this in mind, the following recommendations are made:

- Examine the budget technique for computing area-averaged vertical velocities and the interpolation scheme employed within the mass budget to isolate the sources of the errors in the budged derived vertical velocities.
- Perform budget studies on the model cyclones during earlier and later time periods than covered in this study.
- Perform budget studies on model generated anticyclones to determine if they are characterized by the 12-hour cyclic pattern of the model cyclones.
- Study the cyclic oscillations by differencing successive pressure fields.
- Perform budget studies on cyclones and anticyclones generated in the Sandgathe (1981) adiabatic experiments.
- Perform budget studies of other properties on these model cyclones and on model anticyclones.

APPENDIX A

COMMONLY USED ACRONYMS AND ABBREVIATIONS

NOGAPS	Navy Operational Atmospheric Prediction Model
UCLA	University of California, Los Angeles
NNW	Naval Environmental Prediction Research Facility
ENE	east-northeast
ESE	east-southeast
NNE	north-northeast
SSW	south-southwest
LND	level of nondivergence
AVA	anticyclonic vorticity advection
CVA	cyclonic vorticity advection
PBL	planetary boundary layer
sec^{-1}	per second
mb	millibar
^{o}C	degree Celcius
^{o}K	degree Kelvin

NH northern hemisphere

SH southern hemisphere

nm nautical miles

M mass

N north

S south

m meters

APPENDIX B

QUASI-LAGRANGIAN BUDGET FRAMEWORK AND GENERALIZED BUDGET EQUATIONS

The purpose of this appendix is to present the formulation of the storm budget volume coordinate system and the generalized budget equations which can be applied to any desired atmospheric property. The information contained herein is extracted from Wash (1978) as adopted from Johnson and Downey (1975 a).

The storm budget volume in spherical coordinates is depicted in Fig. 41. The following notation is relevant to this figure:

α	Azimuthal coordinate
β	Angular radial coordinate
$\underset{\sim}{r}$	Position vector from earth's center
$\underset{\sim}{R}$	Position vector from storm center to any point in budget volume
$\underset{\sim}{m},\underset{\sim}{l},\underset{\sim}{k}$	Orthognal unit vectors along meridional, azimuthal and vertical directions of spherical coordinates for storm
$\underset{\sim}{U}$	Wind velocity relative to earth

$\underset{\sim}{W}$	Horizontal velocity of reference axis
$\underset{\sim}{W}_o$	Horizontal velocity of any point on the volume boundary.

Table VI contains a listing of the generalized budget equations. The following is an explanation of the notation used in these equations:

σ	The vertical coordinate system
V	Volume
T	Top boundary
B	Bottom boundary
$(U-W)_\beta$	Horizontal wind component relative to budget volume normal to lateral boundary
$(d\dot{\sigma}/dt)$	Vertical velocity divergence into a layer within the volume
$r\sin\beta$	Radius of budget volume
p_*	Surface pressure
f	Specific budget property (per unit mass)
$\dot{\sigma}$	Vertical velocity ($d\sigma/dt$)
g	Acceleration due to gravity

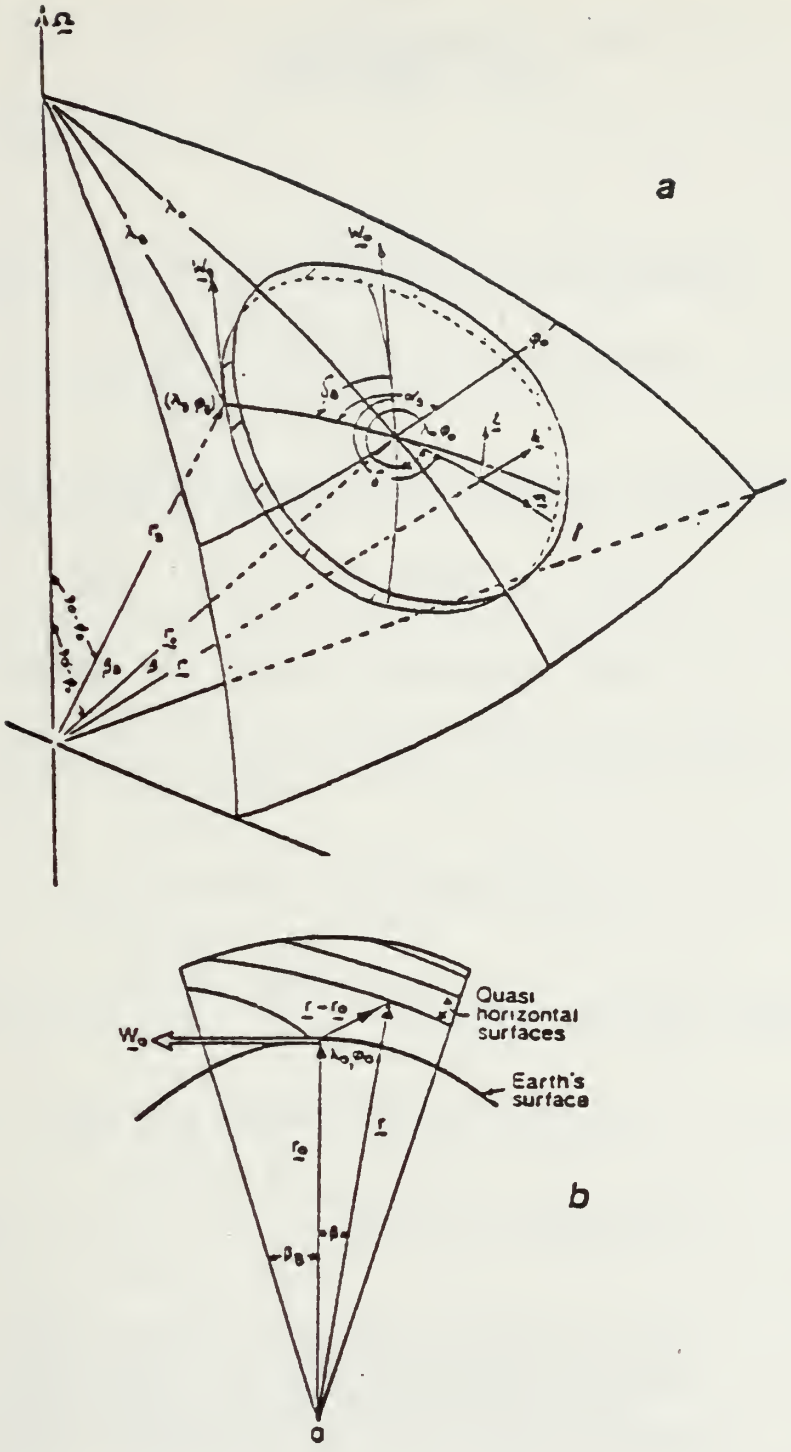

Figure 41. Quasi-Langrangian storm budget volume coordinate system.

TABLE V

GENERALIZED QUASI-LAGRANGIAN BUDGET EQUATIONS IN SIGMA COORDINATES
(after Wash, 1978)

The budget volume integral is defined as

$$F = \int_{\sigma_B}^{\sigma_T} \int_{0}^{\beta_B} \int_{0}^{2\pi} \frac{p_*}{g} fr^2 \sin\beta d\alpha d\beta(-d\sigma).$$

The most general form of the budget equation is

$$\frac{dF}{dt} = LT(F) + VT(F) + S(F)$$

where the lateral transport term is

$$LT(F) = \int_{\sigma_B}^{\sigma_T} \int_{0}^{2\pi} \frac{p_*}{g} f(U-W)_\beta r \sin\beta d\alpha(-d\sigma) \Big|_{\beta_B},$$

the vertical transport term is

$$VT(F) = \int_{\sigma_B}^{\sigma_T} \int_{0}^{\beta_B} \int_{0}^{2\pi} \frac{p_*}{g} \frac{\partial}{\partial\sigma} (f\sigma) \sin\beta d\alpha d\beta (-d\sigma),$$

and the source (sink) term is

$$S(F) = \int_{\sigma_B}^{\sigma_T} \int_{0}^{\beta_B} \int_{0}^{2\pi} \frac{p_*}{g} \frac{df}{dt} r^2 \sin\beta d\alpha d\beta(-d\sigma).$$

The vertical transport term is zero when the limits of integration are $\sigma = 1$ and $\sigma = 0$, since there can be no transport through the top and bottom boundaries of the budget volume.

LIST OF REFERENCES

Arakawa, A., and V. Lamb, 1977: Computational design of the basic dynamical processes of the UCLA general circulation model. Methods in Computational Physics, 17, 173-265, Academic Press, New York.

Arakawa, A., and W. Schubert, 1974: Interaction of a cumulus cloud ensemble with the large-scale environment, part I. J. Atmos. Sci., 31, 674-701.

Chen, T. G., and L. F. Bosart, 1977: Quasi-Lagrangian kinetic energy budgets of composite cyclone-anticyclone couplets. J. Atmos. Sci., 34, 452-464.

Conant, P. R., 1982: A study of east-coast cyclogenesis employing Quasi-Lagrangian diagnostics. M.S. Thesis, Naval Postgraduate School, 102 pp.

Deardorff, J. W., 1972: Parameterization of the planetary boundary layer for use in general circulation models. Mon. Wea. Rev., 100, 93-106.

Downey, W. K. and D. R. Johnson, 1978: The mass, absolute angular momentum and kinetic energy budgets of model generated extratropical cyclones and anti-cyclones, Mon. Wea. Rev., 106, 469-481.

Johnson, D. R. and W. K. Downey, 1975a: Azimuthally averaged transport and budget equations for storms: Quasi-Lagrangian diagnostics 1. Mon. Wea. Rev., 103, 967-979.

Johnson, D. R. and W. K. Downey, 1975b: The absolute angular momentum of storms: Quasi-Lagrangian diagnostics 2. Mon. Wea. Rev., 103, 1063-1076.

Johnson, D. R. and W. K. Downey, 1976: The absolute angular momentum budget of an extratropical cyclone: Quasi-Lagrangian diagnostics 3. Mon. Wea. Rev., 104, 3-14.

Katayama, A., 1972: A simplified scheme for computing radiative transfer in the troposphere. Tech. Report No. 6, Dept. of Meteor., University of California, Los Angeles.

Kung, E. C. and W. E. Baker, 1975: Energy transformations in middle-latitude disturbances. Quart. J. Roy. Meteor. Soc., 101, 793-819.

Lord, S. J., 1978: Development and observational verification of a cumulus cloud parapererization. Ph.D. thesis, Dept. of Atmos. Sci., University of California, Los Angeles.

Nitta, T., and J. Yamamoto, 1974: On the observational characteristics of intermediated scale disturbances generated near Japan and vicinity. J. Meteor. Soc., Japan, 52, No. 1, 11-13.

Oort, A. H., and E. R. Rasmusson, 1974: Atmospheric circulation statistics. NOAA Prof. Paper 5. (U. S. Govt. Printing Office, Stock No. 0317-0045, c55.25:5.)

Petterssen, S., 1956: Weather Analysis and Forecasting, Second Edition, Vol. I. McGraw-Hill, New York, Chap. 16 and 17.

Petterssen, S., D. Bradbury and K. Pedersen, 1962: The Norwegian cyclone models in relation to heat and cold sources. Geofys. Publor., 24, 243-280.

Petterssen, S., and S. J. Smebye, 1971: On the development of extratropical cyclones. Quart. J. Roy. Meteor. Soc., 97, 457-482.

Randall, D. A., 1976: The interaction of the planetary boundary layer with large-scale circulations. Ph.D. thesis, Dept. of Atmos. Sci., University of California, Los Angeles.

Roman, D., 1981: Application of Quasi-Lagrangian diagnostics and FGGE data in a study of east-coast cyclogenesis. M.S. Thesis, Naval Postgraduate School, 93 pp.

Sanders, F. and Gyakum, J. R., 1980: Synoptic-dynamic climatology of the "Bomb", Mon. Wea. Rev., 108, 1589-1606.

Sandgathe, S. A., 1981: A numerical study of the role of air-sea fluxes in extratropical cyclogenesis, Ph.D Thesis, Department of Meteorology, Naval Postgraduate School.

Simmons, A. J., and B. J. Hoskins, 1977: Baroclinic instability on the sphere: solutions with a more realistic tropopause. J. Atmos. Sci., 34, 581-588.

Simmons, A. J., and B. J. Hoskins, 1978: The life cycles of some nonlinear baroclinic waves. J. Atmos. Sci., 35, 414-432.

Smith, P. J., 1973: The kinetic energy budget over North America during a period of major cyclone development, Tellus, 25, 411-423.

Spaete, P., 1974: A diagnostic study of the available potential and kinetic energies of a mid-latitude cyclone. M.S. Thesis, University of Wisconsin.

Wash, C. H., 1975: Circulation budget of extratropical cyclones, M.S. Thesis, Department of Meteorology, University of Wisconsin, 176 pp.

Wash, C. H., 1978: Diagnostics of observed and numerically simulated extratropical cyclones, Ph.D. Thesis, Department of Meteorology, University of Wisconsin, 215 pp.

INITIAL DISTRIBUTION LIST

		No. Copies
1.	Professor Carlyle H. Wash, Code63Cw Department of Meteorology Naval Postgraduate School Monterey, CA 93940	5
2.	Professor Russell L. Elsberry, Code 63Es Department of Meteorology Naval Postgraduate School Monterey, CA 93940	1
3.	Professor Robert J. Renard, Code 63Rd Department of Meteorology Naval Postgraduate School Monterey, CA 93940	1
4.	Capt. William C. Tallman PSC Box General Delivery Langley AFB, VA 23665	3
5.	Capt. Alan R. Shaffer, Code 63 Department of Meteorology Naval Postgraduate School Monterey, CA 93940	1
6.	LCDR. Scott Sandgathe, Code 63Ss Department of Meteorology Naval Postgraduate School Monterey, CA 93940	1
7.	James Peak, Code 63Pj Department of Meteorology Naval Postgraduate School Monterey, CA 93940	1
8.	Professor Christopher N. K. Mooers, Code 68Mr Department of Oceanography Naval Postgraduate School Monterey, CA 93940	1
9.	Library, Code 0142 Naval Postgraduate School Monterey, CA 93940	2
10.	Commander Air Weather Service Scott Air Force Base, IL 62225	1
11.	Air Weather Service Technical Library Scott Air Force Base, IL 62225	1

12. Commander
Air Force Global Weather Central
Offutt Air Force Base, NE 68113 — 1

13. Capt. Brian Van Orman
Program Manager, AFIT/CIRF
Air Force Institute of Technology
Wright-Patterson Air Force Base, OH 45433 — 1

14. Commanding Officer
Fleet Numerical Oceanography Center
Monterey, CA 93940 — 1

15. Commanding Officer
Naval Environmental Prediction Research Facility
Monterey, CA 93940 — 1

16. Commander (Air-370)
Naval Air Systems Command
Headquarters
Department of the Navy
Washington, D. C. 20361 — 1

17. Defense Technical Information Center
Cameron Station
Alexandria, VA 22314 — 2

18. Director
Naval Oceanography Division
Naval Observatory
34th and Massachusetts Avenue NW
Washington, D.C. 20390 — 1

19. Commanding Officer
Naval Oceanographic Office
NSTL Station
Bay St. Louis, MS 39522 — 1

20. Office of Naval Research (Code 480)
Naval Ocean Research and Development Activity
NSTL Station
Bay ST. Louis, MS 39522 — 1

21. Chairman, Oceanography Department
U. S. Naval Academy
Annapolis, MD 21402 — 1

22. Chief of Naval Research
800 N. Quincy Street
Arlington, VA 22217 — 1

Thesis
T13423
c.1

198183

Tallman
Application of quasi-lagrangian diagnostics to the study of numerically-simulated oceanic cyclones.